Advancement of Asymmetric Bipolar Membranes for Tailoring Chemical Environments in Electrochemical Systems

Thesis by

Éowyn Lucas

In Partial Fulfillment of the Requirements for

the Degree of

Doctor of Philosophy

CALIFORNIA INSTITUTE OF TECHNOLOGY

Pasadena, California

2023

(Defended May 9, 2023)

Éowyn Lucas
ORCID: 0000-0002-8743-5722

Acknowledgments

This work would not have been possible without the support of brilliant academic mentors, caring friends, and a loving and supportive family.

First, I would like to thank my advisor Professor Harry Atwater. Harry's excitement and passion for science has been a guiding light through my PhD experience. I encountered many challenges and roadblocks during my time at Caltech and considered leaving multiple time. I want to thank Harry for always believing in me, my work, and my ability to persevere. Furthermore, I would like to thank Harry for supporting my research interests, my crazy ideas, and for teaching me how to employ the tools of science to create a better world for all.

I would also like to thank Professor CX Xiang and Professor Shane Ardo for their support as non-official mentors through much of my PhD work. Specifically, I would like to thank CX for sharing his extensive knowledge on electrochemistry and Shane for his out of the box ideas and enthusiasm for "team save the planet."

Next, thank you to the faculty members who served on my thesis committee, Professor Bill Goddard, Professor CX Xiang, and Professor Karthish Manthiram. Thank you for your time, enthusiasm about my work, and insightful discussion.

I also interacted with many peers (post docs, grads, and undergrads) along the way who guided and supported me and my work. Through the course of my time at Caltech I had the incredible opportunity to work with the following post docs, staff scientist, and graduate students who were always happy and eager to share knowledge and lend a hand: Alex Welch, Giulia Tagliabue, Joe Duchene, Annette Boehme, Aidan Fenwick, Ian Sullivan, Ibadillah Digdaya, Monica Hwang, Aisulu Aitbekova, Kaiwen Wang, Bill Zhang, Zachary Schiffer, Lily Shiau, Emily Dunn, and Ellis Spickermann. Additionally, I would like to thank the following undergraduate researchers with whom I had the opportunity to mentor and learn from: Abby Carbone and Jillian Reed.

The final academic mentor who I would like to thank is my undergraduate research advisor, Professor Veronica Augustine. Veronica was my first mentor in the realm of academia and research. She has always believed in me and even as a young

undergraduate assigned me independent research. I am eternally grateful for the invaluable lessons learned during this experience and for the powerful guidance from a young female mentor pushing boundaries in science and academia.

Furthermore, I would like to thank my entire materials science class at Caltech, without whom I would never have survived the first two years of coursework. I would also like to specifically thank Alex Welch, Megan Phelan, and Sydney Corona for their friendship and support through the challenging years we shared working on our PhDs at Caltech.

Outside of academia, I have had the great joy of developing many close friendships in dance communities, climbing communities, and beyond. I would like to specifically thank Alex, Megan, Kendall, Sydney, David, Katie, Sondra, Nico, Logan, and Aaron, as well as the entire taco Tuesday crew for their continual love, support, and care through the challenging and stressful PhD years of my life, as well as for the many adventures we have all shared along the way!

I would also like to thank Holly and Hazel, my forever friends from back home in North Carolina. These two have stuck with me through thick and thin for over a decade and although we do not see each other as much as I would like, I know their love is ever present. Love you both so much!

Last, but definitely not least, I would like to thank my family for their guidance through life and for supporting and loving me, no matter what, through all my ups and downs, always. Mom, dad, and Nathan, you are my heroes! I love you all so much.

Abstract

Under reverse bias, bipolar membranes (BPMs) enhance water dissociation (WD) at the junction between a cation exchange layer (CEL) and an anion exchange layer (AEL), often with additional improvement from an integrated WD catalyst. Recent research has shown promise for developing and implementing BPMs in renewable energy systems, such as carbon removal, water and CO_2 electrolysis, and energy storage. The economic feasibility of these carbon capture and conversion systems with incorporated BPMs, however, relies on BPMs to maintain stable operation at high current densities (>100 mA cm^{-2}) and low overpotentials. Existing commercial BPMs are limited to current densities of ≤100 mA cm^{-2} as water transport through the CEL and AEL cannot keep up with the increased rate of WD at the junction at higher current densities. In this work, we present a freestanding, high current density BPM (HCD-BPM) with a thin AEL (15 μm, PiperION 15R), a graphene oxide (GrOx) catalyst layer, and a mechanically supportive CEL (50 μm, Nafion 212) specifically designed to overcome water transport limitations. When tested under reverse bias in a custom electrodialysis cell with Luggin capillaries, this HCD-BPM demonstrates the lowest published overpotentials up to 1 A cm^{-2}. Furthermore, the HCD-BPM exhibits stabilities of >1000 hour at 80 mA cm^{-2}, >100 hours at 500 mA cm^{-2}, and >60 hours at 1 A cm^{-2}, Faradaic efficiencies for H^+ and OH^- of >95%, and successful implementation into a multi-cell electrodialysis stack designed for integration into a DOC system. Additional characterization, such as SEM, Confocal microscopy, and titration, was performed to understand the structure and performance of the HCD-BPM. Additionally, the BPM was tested in forward bias to

investigate its use for acid/base flow batteries. Overall, this thesis presents a novel BPM with record performance in multiple electrochemical systems that mitigate anthropogenic CO_2 emissions.

Published Content and Contributions

Measurement of ion transport properties in ion exchange membranes for photoelectrochemical water splitting
Éowyn Lucas, Lihao Han, Ian Sullivan, Harry A. Atwater, and Chengxiang Xiang.
Frontiers in Energy Research. 2022.
DOI: 10.3389/fenrg.2022.1001684
Contributions: experimental design, material fabrication, data collection, data analysis, manuscript writing and revision.

Challenges and opportunities in continuous flow processes for electrochemically mediated carbon capture
Yayuan Liu, Éowyn Lucas, Ian Sullivan, Xing Li, and Chengxiang Xiang.
iScience. Volume 25, Issue 10. 2022.
DOI: 10.1016/j.isci.2022.105153
Contributions: input and writing on bipolar membrane sections, manuscript revision

High current density, catalyzed bipolar membrane for efficient direct ocean capture
Éowyn Lucas, Chengxiang Xiang, and Harry A. Atwater.
Provisional patent filed June 28, 2022.
Contributions: experimental design, material fabrication, data collection, data analysis, manuscript writing and revision.

Asymmetric bipolar membrane for high current density electrodialysis operation with exceptional stability
Éowyn Lucas, Justin C. Bui, Monica Hwang, Kaiwen Wang, Alexis T. Bell, Adam Z. Weber, Shane Ardo, Harry A. Atwater, and Chengxiang Xiang.
Nature Energy. In Review. Submitted February 7, 2023.
ChemRxiv. April 6, 2023.
Contributions: experimental design, material fabrication, data collection, data analysis, manuscript writing and revision.

Modeling bipolar membranes for electrochemical carbon capture
Justin C. Bui, Éowyn Lucas, Eric W. Lees, Andrew K. Liu, Harry A. Atwater, Chengxiang Xiang, Alexis T. Bell, and Adam Z. Weber.
Energy & Environmental Science. In Review. Submitted May 18, 2023
ChemRxiv. May 12, 2023.
Contributions: experimental design, material fabrication, data collection, data analysis, manuscript writing and revision.

Bipolar membrane mediated efficient acid-base combination yielding high power density

Zishuai Bill Zhang[#], Éowyn Lucas[#], Harry A. Atwater, and Chengxiang Xiang.
[#]These authors contributed equally to this work
In preparation.
Contributions: experimental design, material fabrication, data collection, data analysis, manuscript writing and revision.

Table of Contents

List of Figures and Tables

Chapter 1: Introduction to Bipolar Membranes: Motivation, Fundamentals, and New Achievements

Content drawn from: Éowyn Lucas, Lihao Han, Ian Sullivan, Harry A. Atwater, and Chengxiang Xiang. Measurement of ion transport properties in ion exchange membranes for photoelectrochemical water splitting. Frontiers in Energy Research. 2022. DOI: 10.3389/fenrg.2022.1001684.

1.1 Motivation

As atmospheric CO_2 levels from anthropogenic emissions continue to rise, it is critical to rapidly implements carbon neutral and carbon negative technologies across all sectors of industry and the economy (e.g., energy, energy storage, transportation, chemical production). In 2015, the Paris climate accord set a goal of limiting average warming to below 2°C within this century in order to prevent irreversible climate tipping points.[5] However, due to a lack of timely implementation of carbon neutral solutions, to meet this goal it is critical to drastically expand the development and implementation of carbon negative technologies (**Figure 1.1**).[6–8]

Recent studies of bipolar membranes (BPMs), specialized ion exchange membranes with two laminated regions of opposite charge, have been demonstrated as beneficial components in electrochemically mediated carbon removal, carbon conversion, water electrolysis, and energy storage.[1,9] The capital cost per area of a BPM, however, is significant; therefor, high current density operation is ideal to produce larger concentrations of acid and base with the same membrane area.[10] Accordingly, for BPMs to be an economically justifiable component in energy technologies, further work is necessary to demonstrate stable operation at high current densities (> 100 mA cm^{-2}). The work presented in this thesis investigates a novel high current density BPM (HCD-BPM) implemented successfully in multiple

systems (e.g., reverse bias electrolysis, forward bias electrolysis, electrodialysis cell stack) and used to effectively elucidate fundamental BPM properties because of its simple design.

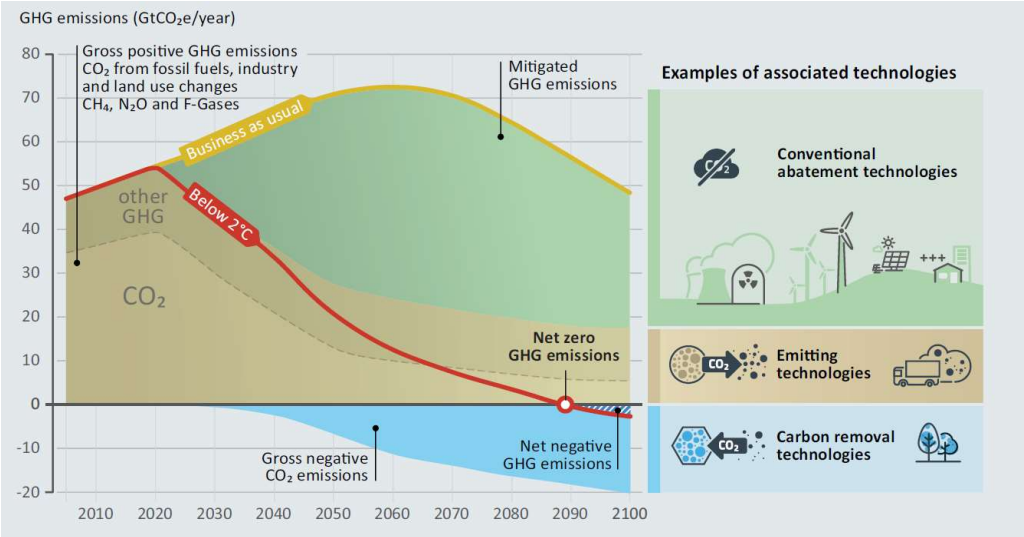

Figure 1.1 Comparison of projected greenhouse gas emissions for multiple scenarios: business as usual (green), implementation of conventional abatement technologies (yellow), and implementation of carbon removal solutions (blue). The red line indicated the maximum emissions allowed to remail below warming of 2°C by the end of this century.[11]

1.2 Background and History of BPMs

First, it is important to clearly define a BPM and its monopolar membrane components. Monopolar ion exchange membranes consist of polymers with ionizable functional groups, which allow for selective transport of cations through cation exchange membranes (CEMs) and anions through anion exchange membranes (AEMs), as depicted in **Figure 1.2**.[12–14] A BPM consists of a cation exchange layer (CEL) laminated to an anion exchange layer (AEL), usually with a water dissociation (WD) catalyst at the junction between the CEL and AEL (**Figure 1.2c**).[1,15] Under reverse bias, a voltage is applied across the BPM and enhanced WD to H^+ and OH^-

occurs at the junction between the CEL and AEL. H^+ ions then travel selectively through the CEL, while OH^- ions travel through the AEL, creating separate acidic and basic streams on either side of the BPM.[1,9] Under forward bias, energy is produced when H^+ and OH^- recombine at the BPM junction.[16–18] Further details on the fundamentals of BPMs and their components are explored in **Section 1.3**.

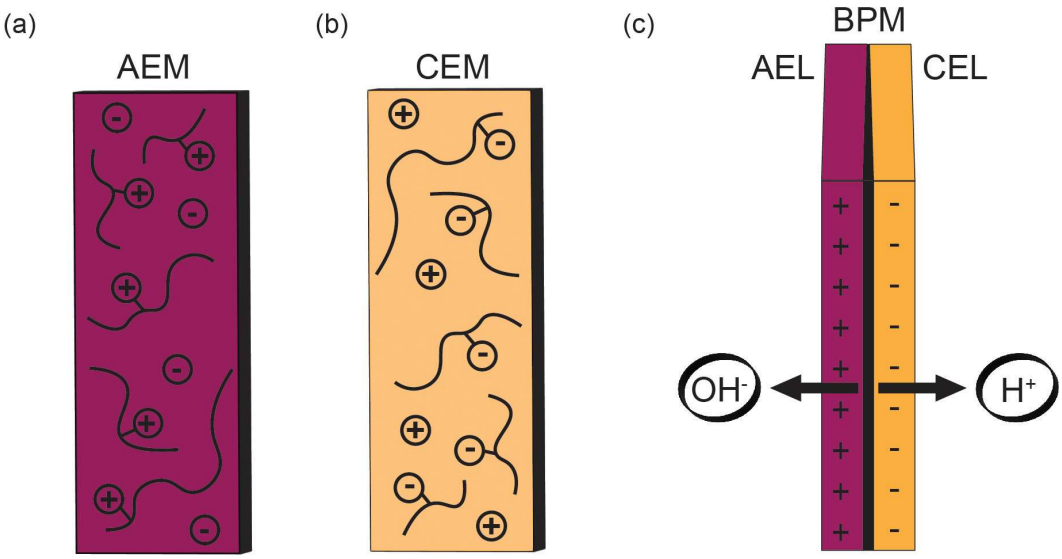

Figure 1.2 Schematic of an anion exchange membrane (a), cation exchange membrane (b), and laminated bipolar membrane (c) structure and charged groups.

To facilitate a better understanding of the work being done in the field today, a brief history of BPM research and development is presented here. Enhanced WD was first seen to occur in natural membranes in 1914 and the observation was later confirmed in 1956 via examination of a partial current in membranes carried by H^+ and OH^-.[1,19] The first work describing a layered membrane with a CEL and an AEL was also published in 1956, defining this laminated structure as a bipolar membrane.[15] This publication described many of the fundamentals of BPMs that are

still the standard in the field today, such as the enhancement of WD due to a strong electric field at the BPM junction. In 1979, Simons published a detailed theory paper, which established the concept that WD enhancement in a BPM occurred through a protonation/deprotonation mechanism, the first step of which is strongly dependent on electric field strength.[20] This laid the groundwork for a second theory paper published in 1997, which proposed a model combining the second Wien effect and protonation/deprotonation reactions at membrane functional groups to explain the mechanism of enhanced WD in a BPM.[21]

In parallel to the development of fundamentals and theory, BPMs began to be implemented for industrial use starting in 1976 when Allied Chemicals developed the first BPM for an acid-base recovery system.[22] Later, in 1988, Aquatech was the first to commercialize a BPM electrodialysis (BPM-ED) system for acid-base recovery in the stainless-steel industry.[23] To this day, the most common commercial use of BPMs is for processing industrial waste streams for acid/base recovery.[1]

Over the last decade, however, BPMs gained traction as a component in biochemical processes, food processing, recovery of heavy metals and other raw materials, energy storage, and carbon capture and conversion.[1] The work presented in this thesis focuses on BPMs energy system applications. One of the first examples of a BPM being used in an energy system was in 1983 when a BPM supported fuel cell was published.[24] For most energy applications to be economically achievable, however, specific operational performance metrics, such as high current density (> 100 mA cm^{-2}) and high current efficiency (> 80%) (discussed further in **Section 1.3**) must be achieved.[25–27] Current technology readiness level vs. necessary operational

current density for the most common electrochemical energy systems is plotted in **Figure 1.3**.[28] **Section 1.4** of this thesis discusses remaining challenges, addressed in this thesis, for achieving technological readiness for BPM electrodialysis (BPM-ED), water electrolysis (hydrogen evolution reaction, HER), CO_2 reduction (CO_2R), and flow batteries.

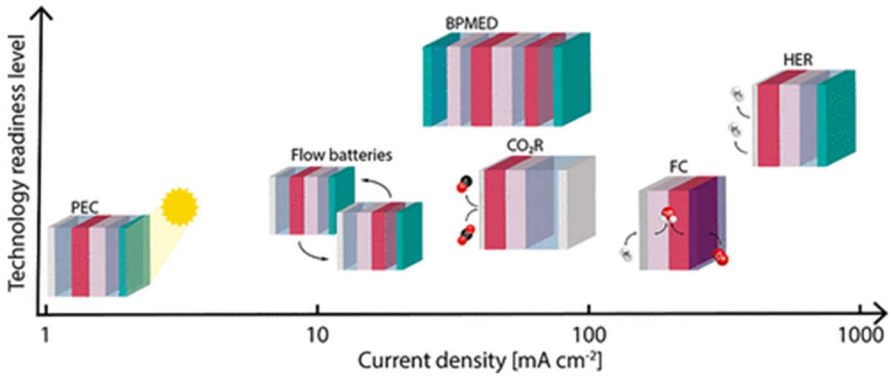

Figure 1.3 Technology readiness level vs. current density for various electrochemical systems incorporating BPMs.[28]

1.3 BPM Fundamentals

To improve understanding of the work presented in this thesis, a deeper dive into the fundamentals of BPMs is presented. When a CEL and AEL are laminated together to form a BPM, free cations in the CEL and free anions in the AEL recombine at the junction (much like electrons and holes in a p-n junction) forming a depletion region on the order of just a few nm, which results in a strong electric field of 10^8 –10^9 V m^{-1}.[1,9] The thickness of the region and associated electric field strength is dependent on the pK_a (tendency for ionic dissociation) of the fixed charge groups and the ion exchange capacity (IEC, concentration of fixed charges in an ion exchange membrane) of the AEL and CEL.[29–31] **Figure 1.4a** depicts the

concentration of ion species and resulting electric field across a BPM with an abrupt junction between the CEL and AEL.[1] **Figure 1.4b** depicts the ionic concentrations and electric field across a BPM with a junction gap, a concept which is discussed later in this section.[21]

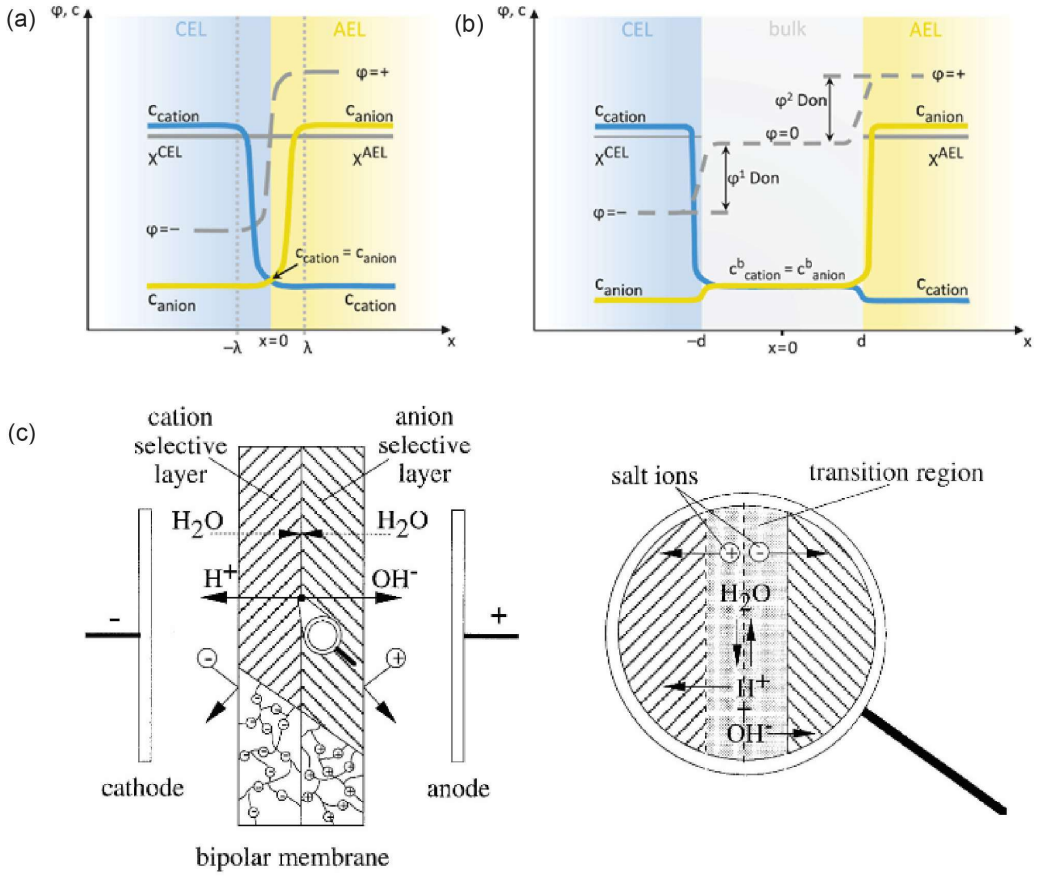

Figure 1.4 Schematic of ion concentration and voltage profiles in a BPM with an abrupt CEL/AEL junction (a) and a neutral solution layer (b), where c is the concentration, X is the ion exchange capacity, and φ is the electric potential. (c) Schematic of BPM structure and ion transport in reverse bias.[1,21]

Another element to consider in the design of a BPM is the individual properties as well as the subsequent compatibility of the CEL and AEL. One property already mentioned is the IEC, which dictates the strength of the electric field at the

junction as well as the ionic conductivity of the individual membranes.[31] Although increasing the IEC can improve the electric field strength and increase the ionic conductivity across the BPM, it can also lead to leakage of undesired co-ions and counter-ions, and consequently a loss in efficiency.[31] Furthermore, it is important to consider the chemical structures of the CEL and AEL to determine their chemical and mechanical compatibility. Ideally, the two membranes will have similar lateral expansion when wetted to mitigate mechanical deformation and junction delamination.[1,9] The CEL and AEL must also be chemically stable in acidic and alkaline environments, respectively, otherwise chemical degradation leading to membrane failure can occur.[1,9] Finally, one or both of the membrane layers must be able to sufficiently transport water and prevent mechanical degradation due to drying in reverse bias or excess water build up in forward bias.[17,18]

As mentioned in **Section 1.2**, theoretical studies have demonstrated that WD is enhanced through a combination of the second Wien effect (which defines the response of a weak electrolyte in the presence of an electric field) and protonation/deprotonation reactions on surface sites in the BPM junction, due to the depletion region and resulting electric field.[20,32] The rate of WD in a BPM can be further enhanced with addition of a catalyst layer between the CEL and AEL. Increased charge density and more extreme pK_a values of catalyst sites are theorized to further strengthen the electric field as well as provide an alternative WD reaction pathway.[33–36] A range of catalyst materials, mostly metal oxides and hydroxides, have been experimentally examined for enhancement of WD at the BPM junction.[36–

[41] These catalyst materials, as they apply to this thesis, are discussed further in **Chapter 2**.

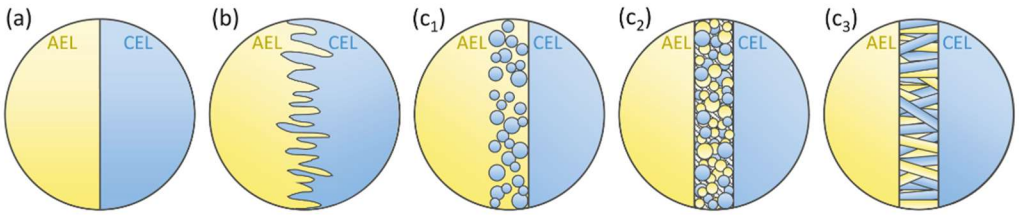

Figure 1.5 Schematic of possible BPM junction geometries: (a) smooth, (b) grooved, (c) 3D.[1]

The geometry of a BPM junction, as depicted in Figure 1.5, can also play an important role in WD enhancement. Numerous studies have investigated 3D geometries of the interface between the CEL, AEL, and catalyst. 3D junctions can increase the quantity of active surface sites for enhanced WD as well as improve mechanical stability, preventing delamination.[42–44] When creating these 3D geometries, however, an increase in resistance and loss of abrupt junction/strong electric field can lead to a decrease in WD activity. Therefore, the increase in active due to a 3D junction geometry and/or added catalysts must be weighed against the competing decrease in electric field and conductivity.[31,35]

1.4 Electrochemical Measurement of BPMs

This section outlines the most important electrochemical experiments typically used to determine BPM performance. First, it is noted that electrochemical cell design itself is critical for accurate measurement of ion transport through, and performance of, BPMs. All electrochemical measurements presented in this thesis

were performed with a custom made electrodialysis flow cell with embedded Luggin capillaries (**Figure 1.6**). The Luggin capillaries allow for minimization of voltage losses due to the electrolyte, while the five-chamber flow design allows for H^+ and OH^- produced via WD to be directly measured since the ions in the center chamber are isolated by the outer AEM and CEMs.[45]

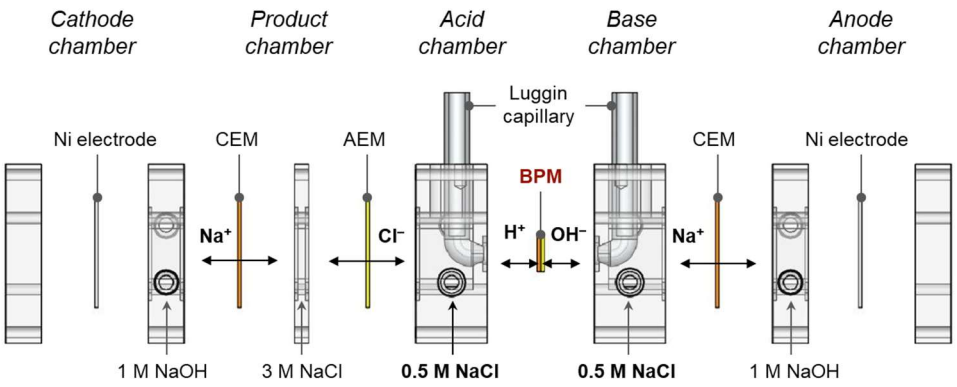

Figure 1.6 Diagram of custom five chamber electrodialysis flow cell with Luggin capillaries.

Chronopotentiometry is one of the most common and elucidating electrochemical measurements performed on BPMs. For these measurements, a specified current is applied across the outer electrodes and the resulting voltage is measured directly across the BPM with reference electrodes (usually in Luggin capillaries).[46] The resulting data can then be used to plot voltage vs. current density (polarization) curves and examine operational voltage stability of the BPM at a specified current density.

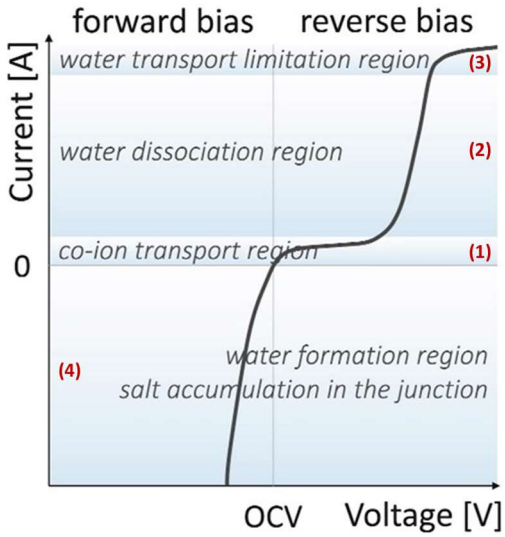

Figure 1.7 Typical current vs. voltage curve for BPMs in forward and reverse bias, depicting four typically observed regions.[1]

Figure 1.7 illustrates a typical polarization curve for a BPM operated in reverse (1-3) and forward (4) bias and indicates four typical regions observed. In region (1), where reverse bias current is low, WD is not yet prominent and co-ion crossover dominates. Eventually, co-ions are flushed out of the CEL and AEL, the limiting current density for WD is surpassed, and WD at the junction occurs more rapidly, allowing migration of H^+ and OH^- to become the prevailing source of current. This leads to the relatively stable voltage seen in region (2), where the current density-voltage relationship becomes ohmic (V=iR) and the small linear increase in voltage is due to the membrane resistance and any residual resistance from the surrounding electrolyte. In region (3), however, the rate of water transport through the CEL and AEL can no longer keep up with the rate of WD at the junction and a sigmoidal increase in voltage is observed.[1,9,45–48] These types of measurements and the resulting polarization curve regions are referenced throughout this thesis.

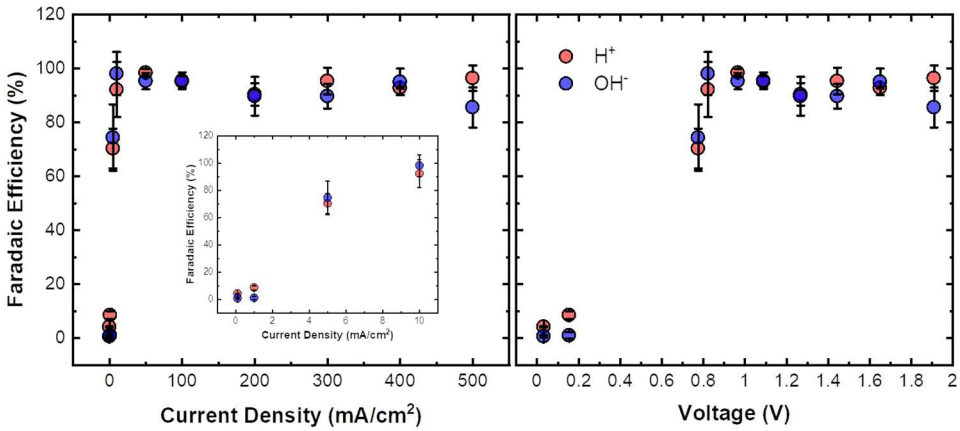

Figure 1.8 Faradaic efficiency of H^+ and OH^- production from enhanced water dissociation vs. current density and voltage for the commercial Fumasep BPM.

Another important performance metric for a BPM is the efficiency at which the current applied across a BPM drives transport of WD products, H^+ and OH^-, over co-ions and counter-ions. Efficiency (or Faradaic efficiency, FE) measurements are typically performed by collecting samples from the acid and base streams of an operating BPM, measuring the pH/$[H^+]$/$[OH^-]$, and comparing this to the expected pH/$[H^+]$/$[OH^-]$ based on the set current density and flow rate. These methods and calculations are discussed in more depth in **Chapter 2**. As an example, experimentally measured FE for a commercial Fumasep BPM is presented in **Figure 1.8**. At low current densities, the FE for both H^+ and OH^- is low, indicating that co-ion and counter-ions account for the majority of the current. In this region, the voltages are relatively low, as an insignificant amount of WD occurred. At current densities ≥10 mA cm^{-2}, however, the FE for both H^+ and OH^- improved substantially and the measured current became dominated by the transport of WD products (H^+ and OH^-). An increase in voltage is also observed as WD begins due to reaction

kinetics and the thermodynamic potential of WD. Additional discussion and analysis of FE measurements is present throughout this thesis.

1.5 BPM Applications of Focus

One of the main BPM applications investigated in this thesis is electrodialysis for carbon removal systems. Most current CO_2 removal projects focus on direct air capture (DAC), using many large fans to pull air across solid or liquid sorbent materials, which draw the CO_2 out of the air stream. The CO_2 is then typically recovered from the sorbent through a highly energy intensive thermal regeneration process.[26,49,50] The process of recovering CO_2 from sorbents, however, can be replaced with BPM mitigated electrochemical pH swings.[10,27,51] A Bjerrum plot of the species abundance in percent of the different forms of dissolved inorganic carbon (DIC) vs. pH (**Figure 1.9**)[2] shows that dissolved CO_2 is the predominant form of DIC at low pH values. Therefore, acidification of DAC liquid CO_2 sorbents via BPM-ED can be used for captured CO_2 recover in place of more energy intensive thermal regeneration methods use today.

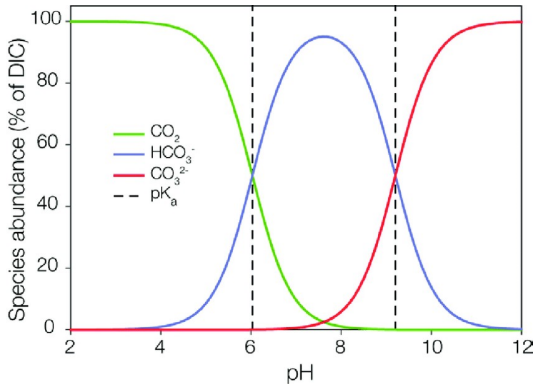

Figure 1.9 Bjerrum plot. Species abundance vs. pH for dissolved CO_2, bicarbonate HCO_3^-, and carbonate CO_3^{2-} at 20°C.[2]

Another opportunity that has gained traction is direct ocean capture (DOC), which offers a promising path for atmospheric CO_2 removal via the ocean (**Figure 1.10**).[52–54] As CO_2 levels increase in the atmosphere, equilibrium is maintained with dissolved carbon in the ocean, leading to a parallel increase, as depicted by the data of dissolved CO_2 over time in **Figure 1.11**.[3] Furthermore, there is ~120% more CO_2 by volume in ocean water than in the air;[54] therefore, the ocean itself acts as the sorbent material, eliminating the need for an absorption step in the CO_2 removal process.

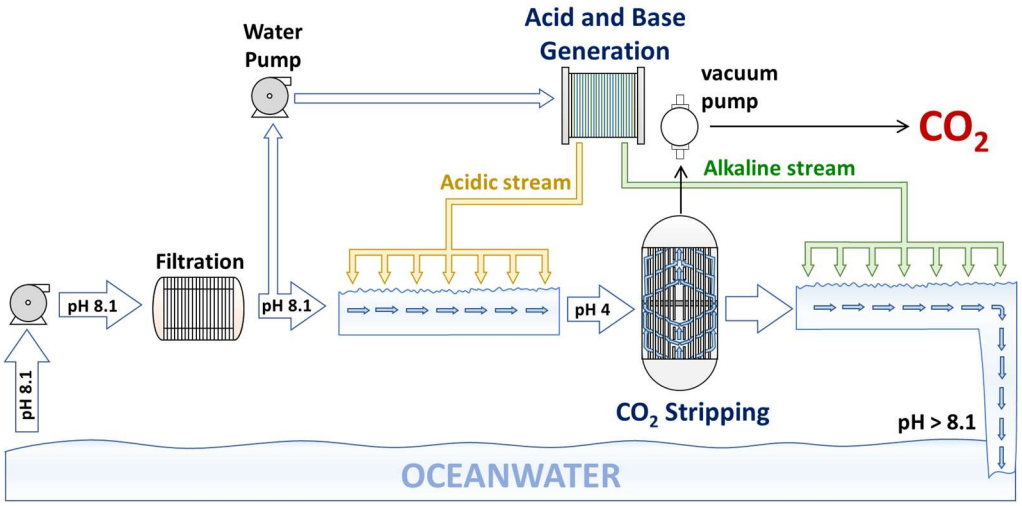

Figure 1.10 Simplified process diagram for a DOC system.

As with DAC, DOC systems take advantage the change in DIC specie concentration with pH. In DOC systems, however, ocean water flows directly through a BPM-ED system to generate acidic and alkaline streams. Dissolved CO_2 is then efficiently stripped from the acidic stream, which is subsequently recombined with the basic stream and returned to the ocean. Lastly, the CO_2 is sequestered or

used to make chemicals, fuels, and plastics.[31,53,55,56] It is also noted here that the HCD-BPM presented in this thesis was initially design for the operational needs of a DOC system.

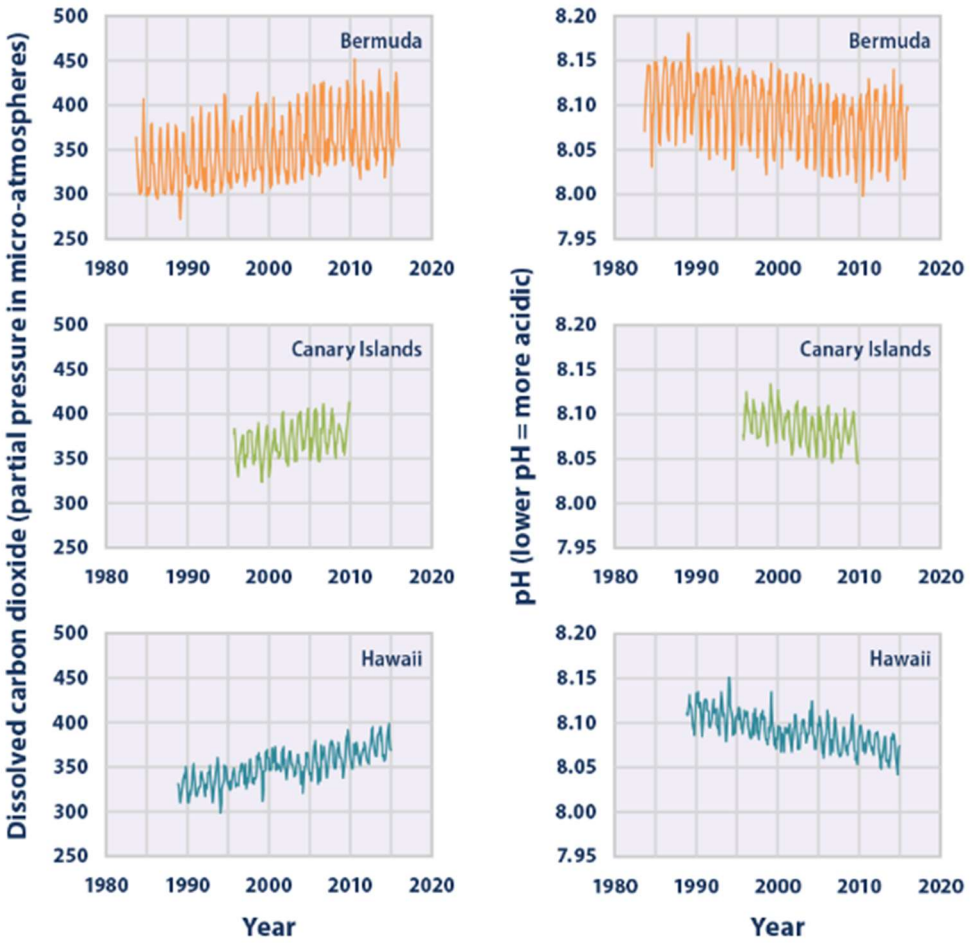

Figure 1.11 Partial pressure of dissolved CO_2 in ocean water and pH of the same ocean water in three different locations over time.[3]

BPMs can also be implemented into water electrolysis and electrochemical CO_2 reduction systems to improve the efficiency of conversion to fuels, chemicals, and plastics (**Figure 1.12**) by sustaining acidic and alkaline environments at the cathode and anode, respectively.[57–64] These cathode and anode pH conditions are

optimal for earth abundant catalyst, which are kinetically more active for HER in acidic conditions, and kinetically more active for OER in alkaline conditions, leading to a lowering of total cell voltage.[57–64] Minimal related work is presented in this thesis about the use of BPMs for CO_2 reduction; however, **Appendix 1** presents preliminary results on the use of nanoporous copper as a CO_2R catalyst. Future work could be done to implement a BPM into this CO_2R system for improvement of reaction environments.

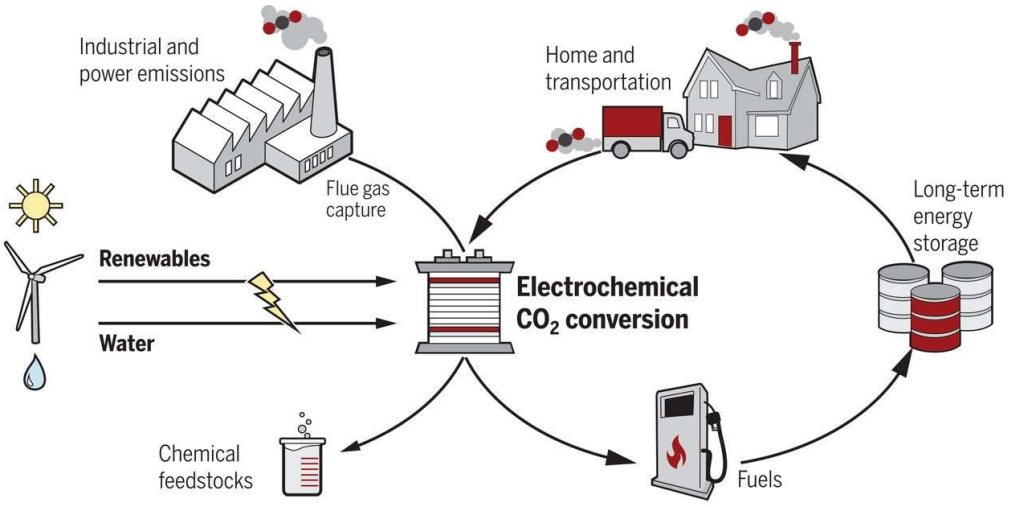

Figure 1.12 Diagram of steps for CO_2 capture and electrochemical conversion to chemicals and fuels.[4]

The final BPM application presented for this thesis is energy storage via a combination of reverse (**Figure 1.13a**) and forward bias (**Figure 1.13b**) operation. In forward bias, H^+ and OH^- travel through the CEL and AEL and combine to form water at the junction of the BPM. When operated in tandem with reverse bias operation, an acid-base flow battery is formed.[18,65–67] Unlike most flow batteries, BPM acid-base systems simply use salt water for operation, eliminating the need for

toxic chemicals and limited mineral resources.[68] With improved BPM efficiencies, these flow batteries have promise to be a scalable, affordable, long term grid level energy storage solution.[65]

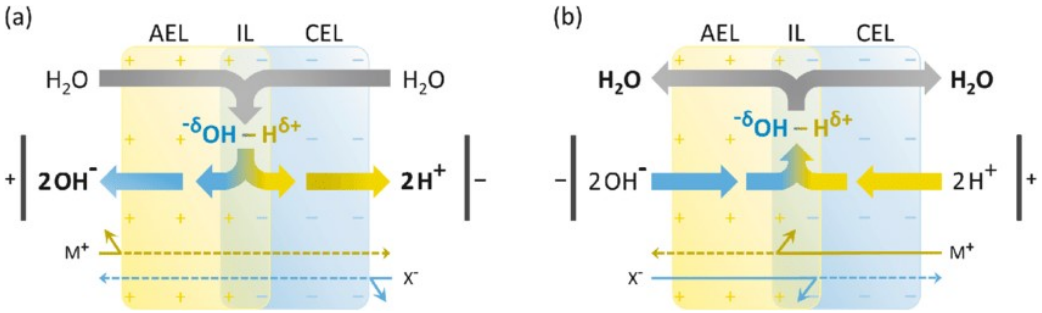

Figure 1.13 Flow diagram of water and ions through a BPM in reverse bias (a) and forward bias (b).[1]

1.6 BPM Challenges Addressed in This Thesis

Although there have been significant advances in BPM performance over the last century, many challenges for commercial implementation into energy systems remain, such as water transport, high current density operation, and junction geometry/lamination.[1,9,28] Furthermore, minimal work has been done to experimentally probe pH and water transport in a BPM and it is not well understood the exact mechanism by which catalysts in BPMs enhance WD. This thesis presents the development, testing, and implementation of a BPM that allows for accelerated water transport to and away from the junction for efficient, high current density operation. The same BPM is then employed for fundamental studies of water transport and pH in and around the membrane.

Chapter 2 presents development, fabrication, and lab scale (1 cm^2 active area) testing/characterization of the HCD-BPM. This chapter, as well as chapter 4, also demonstrate implementation of the HCD-BPM into an electrodialysis cell for DOC.

Chapter 3 delves into in-situ and ex-situ characterization of the BPM and surrounding pH environments using a confocal microscope and pH sensitive dye. Next, ***Chapter 4*** discusses initial scaling (to a 6 cm^2 active area) of the BPM and subsequent implementation into a thin cell electrodialysis stack. Then, in ***Chapter 5***, the BPM is characterized in forward bias, showing that it has potential for implementation in an acid-base flow battery. In addition, this chapter presents a comprehensive investigation of water transport using isotopic labeling in a forward-bias BPM. Finally, ***Chapter 6*** presents experimental work, in collaboration with theory, demonstrating the use of a commercial Fumasep BPM for electrochemical CO_2 recovery as a component of DAC.

Chapter 2: High Current Density Bipolar Membrane Development and Electrochemical Testing

Content drawn from: Éowyn Lucas, Justin C. Bui, Monica Hwang, Kaiwen Wang, Alexis T. Bell, Adam Z. Weber, Shane Ardo, Harry A. Atwater, and Chengxiang Xiang. Asymmetric Bipolar Membrane for High Current Density Electrodialysis Operation with Exceptional Stability. Nature Energy. In Review. Submitted February 7, 2023.

2.1 Introduction

Electrochemical technologies such as water electrolysis,[59,60,63,69] CO_2 conversion,[54,70] and carbon removal [10,54,71,72] are critical for making progress towards a sustainable future.[6–8] Bipolar membranes (BPMs) that demonstrate stable, high current-density operation under reverse bias have immense opportunity for implementation in such devices, due to their ability to sustain constant concentration, separated acidic and alkaline environments in a single device. The ability to sustain large differences in pH allows for cathode and anode local reaction environments that are ideal for attaining high activity, selectivity, and stability of electrocatalysts based on earth-abundant elements.[44,45,73–77] BPMs have also shown promise when integrated into salt-water fed electrodialysis cells used for pH swing-based direct air capture (DAC)[26,49,50] or extraction of dissolved inorganic carbon from ocean water for direct ocean capture (DOC) and ocean deacidification.[10,52,54] Stable BPM operation at high current densities (~ 1 A cm^{-2}) and low voltages (< 1.5 V) is critical to achieve low capital and operating costs in various electrochemical devices.

BPMs are comprised of a cation exchange layer (CEL) laminated to an anion exchange layer (AEL) with a water dissociation (WD) catalyst dispersed at the CEL-AEL junction.[1] At the CEL-AEL junction, mobile protons and hydroxides from the

CEL and AEL react to form water, neutralizing the mobile ions to generate a space–charge depletion region of just a few nanometers, which results in a strong electric field on the order of 10^8 to 10^9 V m^{-1}.[9,78] Under reverse bias, the immense electric field present at the junction accelerates WD via the Second Wien Effect, allowing for enhanced production of H^+ and OH^-, which provide ionic currents through the CEL and AEL and enable buildup of pH gradients across the BPM.[1,29,32,74,79,80] Existing commercial BPMs (e.g., Fumasep FBM, ASTOM BPM) are limited to stable operation at current densities up to ~100 mA cm^{-2}, as the rate of water transport through the CEL and AEL cannot match that of WD in the BPM junction at higher current densities.[1,9,47] Multiple recent efforts have attempted to overcome this water transport limitation by thinning the CEL or AEL to allow for faster water transport to the junction, successfully extending WD operating current densities to the order of 1 A cm^{-2}.[42,44,69,73]

Nonetheless, to achieve industrially relevant rates of WD with minimal applied voltage, BPMs must not only overcome water transport limitations, but also accelerate the rate of WD at the CEL-AEL junction. The addition of a catalyst at the junction further enhances the rate of WD beyond that achievable by the second Wien Effect alone. The catalyst both increases the electric field and provides an alternative path for the WD reaction per the weak acid/base model.[1,41] A range of catalyst materials, such as polymers, metal oxides, and buffer materials have been examined experimentally for WD enhancement.[1,41,81] Previous work predicts that the concentration of ionizable sites in the CEL, AEL, and catalyst layer (CL), along with the specific pK_a values of the catalyst sites, directly affects the rate of WD at the BPM

junction.[1,9,31,41,82] Neither theory nor experiments, however, have been able to determine explicitly which WD enhancement pathway dominates, leaving open a critical area for further investigation.[1,43,83,84]

Despite the substantial enhancements in polymer and catalyst materials for improving water transport and enhancing WD, BPMs suffer from a substantial lack of long-term stability. [1,9] In particular, very few BPMs that have been able to demonstrate high current density operation in electrodialysis, where BPMs are separated by electrolyte channels with limited mechanical support, owing to challenges with adhesion between the two membrane bilayer elements and the CL. Recent work has sought to address this challenge by creating complex junction morphologies to improve catalytic surface area and, furthermore, increase mechanical stability.[42–44] However, no work has demonstrated sustained WD operation in electrodialysis for more than a few hours of uninterrupted stability at current densities >100 mA cm^{-2}.

Herein, we report a BPM comprised of a Nafion 212 CEL (~50 μm), a thin PiperION A15R AEL (~20 μm), and a graphene oxide (GrOx) WD catalyst (200 – 1000 nm) (**Figure 2.1**) that is stable at current densities up to 1 A cm^{-2} when tested under reverse bias in a custom-made, 5-chamber electrodialysis flow cell (**Figure S2.1**). GrOx was chosen as the WD catalyst because it exhibits a low WD overpotential and possesses three ionizable sites with well-defined pK_a values (**Figure 2.1A**). Continuum-level simulation were carried out to investigate the mechanisms of WD occurring on the GrOx layer in the BPM.[85–87] Evaluation of all contributions to the voltage of the GrOx-catalyzed, asymmetric BPM and

comparison with the total experimental voltage, reveals that the BPM operates at just above the thermodynamic potential necessary for WD, with an overpotential of < 250 mV at 1 A cm^{-2}. The reported BPM is also shown to operate for over 1100 hours operation at 80 mA cm^{-2}, over 100 hours at 500 mA cm^{-2}, and over 60 hours at 1 A cm^{-2}, measured independently. This performance indicates effective water transport through the BPM and excellent stability of CEL/AEL junction. Lastly, the GrOx BPM is unique in its ability to achieve similarly low overpotentials when tested freestanding in a 6 cm^{-2} salt water electrodialysis flow cell, conditions necessary for carbon capture via BPM electrodialysis (BPMED) at-scale.

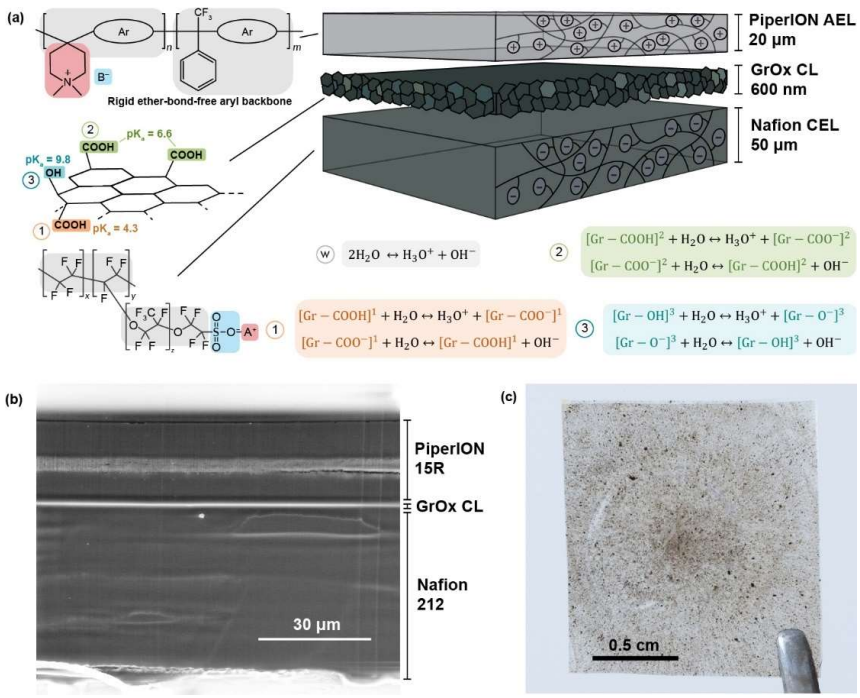

Figure 2.1 GrOx catalyzed, asymmetric BPM design. (a) Schematic of each layer of the BPM, indicating thickness and chemical structure. For the GrOx CL, the sites (1, 2, and 3) that contribute to WD enhancement are labeled with their pKa values and the relevant WD enhancement reactions. (b) SEM cross section of the BPM layers. The lighter region in the AEL is a mechanical support layer. (c) Picture of assembled BPM. [41,88]

2.2 Results and Discussion

Figure 2.1 illustrates the layers and chemical structures of the GrOx catalyzed, asymmetric BPM, along with relevant catalytic WD enhancement reactions (**Figure 2.1A**), a cross sectional SEM of the BPM layers (**Figure 2.1B**), and a picture of the fully assembled BPM (**Figure 2.1C**). Owing to its thin AEL and GrOx catalyst, this BPM was designed to overcome water transport limitations and enable operation at high current densities (≥500 mA cm^{-2}) typically unattainable for commercial BPMs.[28] Polarization curves for the best performing GrOx catalyzed, asymmetric BPM compared to the commercial Fumasep BPM are presented in **Figure 2.2A**. The ability to operate BPMs at high current densities and low voltages is desirable as it enables greater production of acid and base at lower capital and operating costs.[27,51] The GrOx catalyzed, asymmetric BPM outperformed the commercially available BPMs in all current density regions, where the performance of the Fumasep BPMs became significantly limited by either water transport or WD kinetics at current density >300 mA cm^{-2}.

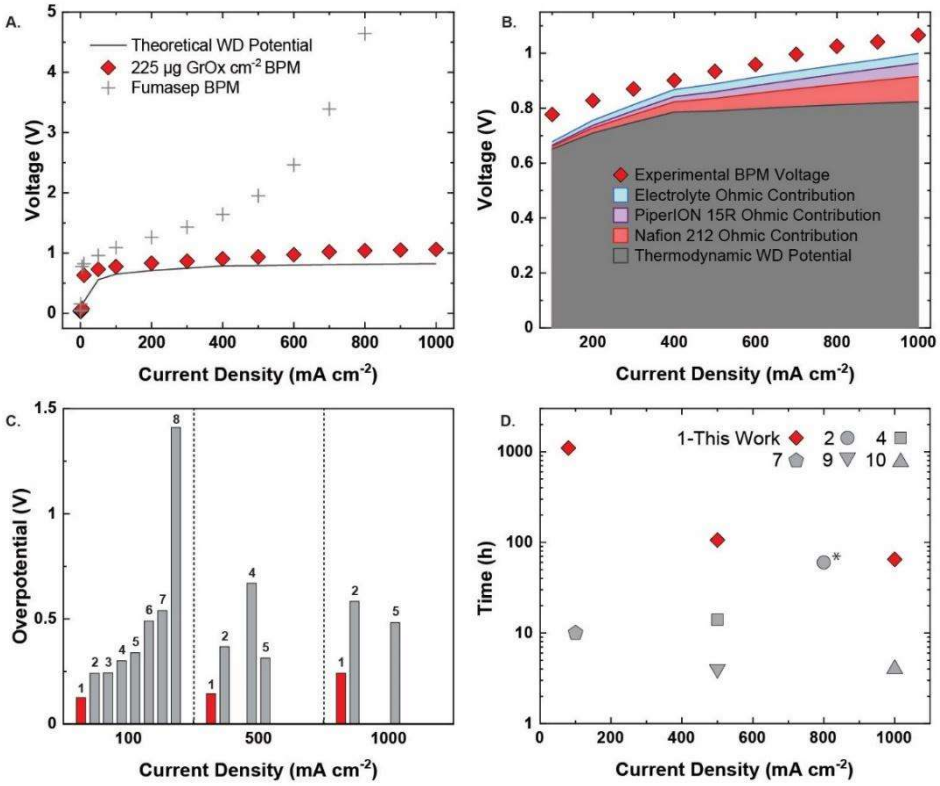

Figure 2.2 GrOx catalyzed, asymmetric BPM performance. (a) Polarization curves for the best performing BPM (225 μg cm^{-2} GrOx loading) and the commercial Fumasep BPM, tested in a custom electrodialysis cell, compared to the thermodynamic potential for WD. (b) Sum of voltage contributions due to WD potential, CEL ohmic losses, AEL ohmic losses, and electrolyte ohmic losses compared to measured performance of the BPM. (c) Overpotentials for the asymmetric BPM compared to other reported BPMs at 100, 500, and 1000 mA cm^{-2}. (d) Stability, in hours, at various current densities, for the reported BPM compared to other BPMs.[39,41–44,69,73,81,84,89] See **Table S2.1** for details about all compared BPMs. *Not continuous.

Figure 2.2B demonstrates that most of the voltage for the BPM is due to the thermodynamic potential required for WD, indicating that the BPM has been optimized for WD close to the maximum possible efficiency. Remarkably, even at a current density of 1 A cm^{-2}, the calculated kinetic overpotential is < 250 mV. The importance of the CL in obtaining these low operating overpotentials is demonstrated in **Figure S2.3**, in which polarization curves of the asymmetric BPM with and

without GrOx are compared. The total overpotential for high current density operation could be further reduced by making the CEL layer thinner or by increasing the ion-exchange capacity of both the CEL and AEL component. However, both changes would lead to an increase in co-ion leakage through the BPM, decreasing the efficiency for making acid and base.[31] We also note that this analysis of the BPM voltage and overpotential neglects any contributions due to pH gradients in the BPM as we are unable to measure the exact pH within the AEL and CEL; however, these contributions are expected to be minimal.[31,32]

Total overpotentials, determined as the sum of contributions due to WD kinetics, membrane resistance, and solution resistance, at 100, 500, and 1000 mA cm^{-2} were calculated for seven, top performing, BPMs.[39,41–44,69,73,81,84,89] Thermodynamic WD potentials at 100, 500, and 1000 mA cm^{-2} were calculated based on the testing environment described in each study (see **Section S2.5.1** for details of these calculations) and are presented in **Table S2.1**. The calculated total overpotentials from the seven publications were then compared to the GrOx catalyzed, asymmetric BPM in **Figure 2.2C**. Our BPM demonstrates the lowest overpotentials across all measured current densities, 126 mV at 100 mA cm^{-2}, 144 mV at 500 mA cm^{-2}, and 242 mV at 1 A cm^{-2}, indicating that it represents a new state-of-the-art for WD energy efficiency in BPMs. Most studies of BPMs in electrodialysis operation have not reported stability data due to problems with membrane delamination experienced by freestanding membranes when tested in saltwater environments.[1,9,89] **Figure 2.2D** compares the stability of the GrOx-catalyzed, asymmetric BPM with those reported

for other BPMs. The points shown are the time to membrane failure, or end of reporting, at a specific current density.

Figure 2.3 shows voltage vs. time plots for the 3 stability points in **Figure 2.2D**. The asymmetric BPM exhibits excellent voltage stability at 80 mA cm^{-2} of 1100 h, at 500 mA cm^{-2} of 100 h, and at 1 A cm^{-2} of 60 h (**Figure 2.3**). The noise seen in the stability data is due to the formation and eventual release of dissolved gas bubbles on the surface of the BPM. Furthermore, the presence of these bubbles at the BPM surface, which only occur after > 1 hour of continuous applied current, leads to additional resistance and higher reported voltage. While many BPMs suffer from poor mechanical adhesion, commonly associated with delamination of the AEL and CEL,[1,9] the Nafion CEL and PiperION AEL used in the BPM presented in this work have excellent adhesion likely due to observed strong electrostatic interactions. Furthermore, this membrane pairing has proven to be mechanically and chemically stable under reverse bias operation as well as in acidic and basic environments.[88,90–92] The addition of a WD catalyst to the BPM junction is typically detrimental to adhesion, necessitating the use of mechanical pressure during operation.[1,9] However, the stability observed for the asymmetric BPM shows that GrOx only minimally interferes with the adhesion between Nafion and PiperION, and as fabricated, the layer-to-layer adhesion is sufficient to facilitate freestanding operation without the need for additional mechanical support.

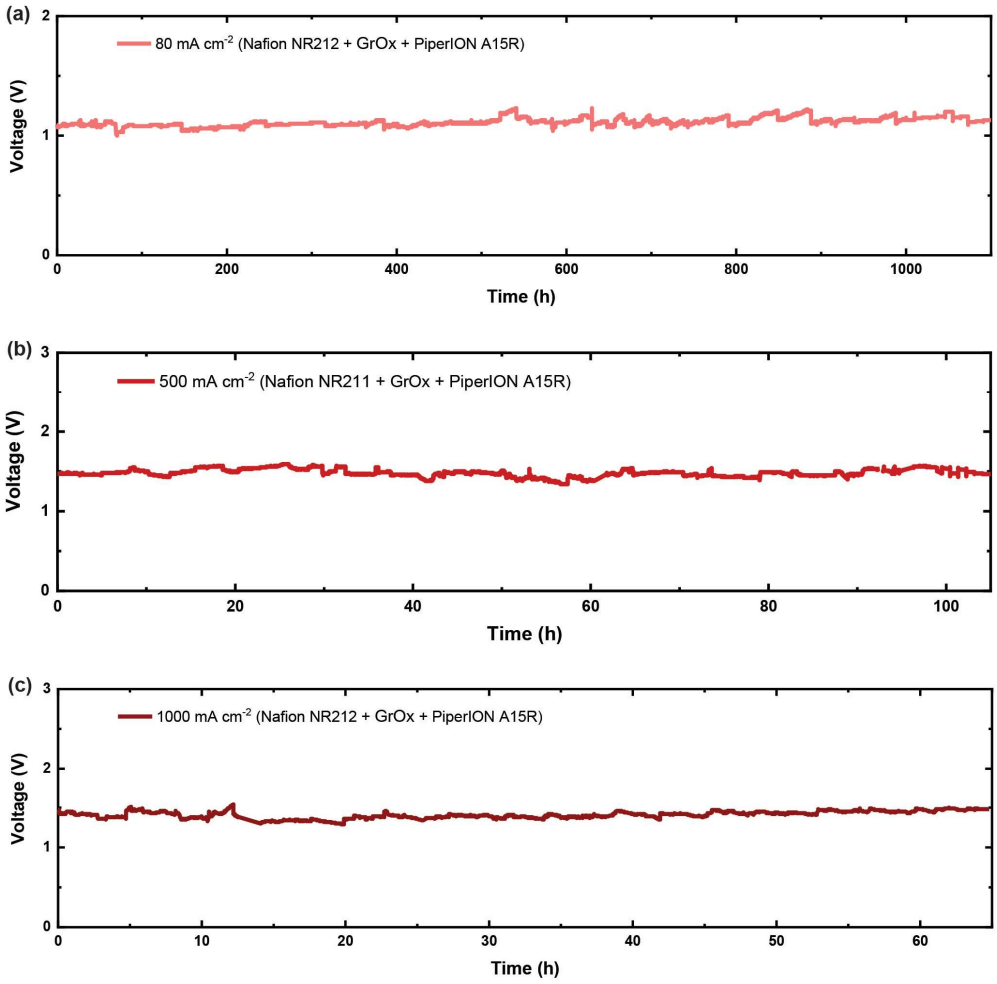

Figure 2.3 Voltage stability of the BPMs over time at (a) 80 mA cm^{-2}, (b) 500 mA cm^{-2}, and (c) 1000 mA cm^{-2}.

One possible hypothesis for the strong adhesion even in the presence of the GrOx CL is that the high conductivity of the GrOx enables the electrostatic forces between the AEL and CEL to maintain adhesion with minimal disruption. However, greater mechanical testing (i.e., pull tests) would be required to fully elucidate the nature of the improved adhesion when employing a GrOx-containing CL. Nonetheless, the strong layer-to-layer adhesion of the BPM, resulting from the optimized combination of Nafion, PiperION, and GrOx, enables the BPM to

overcome the stability limitations due to membrane delamination seen in many other systems.[1,9] The one stability challenge observed for the BPM was delamination due to warping of the Nafion membrane when the BPM was operated at 500 and 1000 mA cm^{-2} for multi-day stability tests. Operation at these high current densities for an extended period of time led to elevated temperatures (> 40°C) in the BPM due to the concentration of current through the custom electrodialysis cell. Thus, we theorize that the elevated temperature over time cause the membranes to warp, delaminate at the junction, and eventually fail.

In addition to low overpotentials and exceptional stability at high current densities, the GrOx-catalyzed, asymmetric BPM exhibits excellent Faradaic efficiencies (FEs, defined as the efficiency of the applied electronic current to generate protons and hydroxides via WD) for acid and base production at > 200 mA cm^{-2} (**Figure 2.4A**). Because of co-ion leakage through the thin AEL, FEs for H^+ and OH^- generation were low (~80% and lower) at operating current densities < 200 mA cm^{-2} (or < 0.8 V, **Figure 2.4B**). However, at current densities of > 200 mA cm^{-2} (> 0.8 V), the FEs for H^+ and OH^- generation were ~95%. This indicates that most of the current flowing through the cell goes to production of acid and base, as desired for the use of a BPM for DAC and DOC. **Figures 2.4c-d** show the FE of H^+ and OH^- vs. current density of the GrOx BPM compared to a commercial Fumasep BPM. At low current densities the thick CEL and AEL of the Fumasep BPM allows for significantly higher FE, however, for high current densities of interest to this work the FE of both membranes levels out around 90-100%.

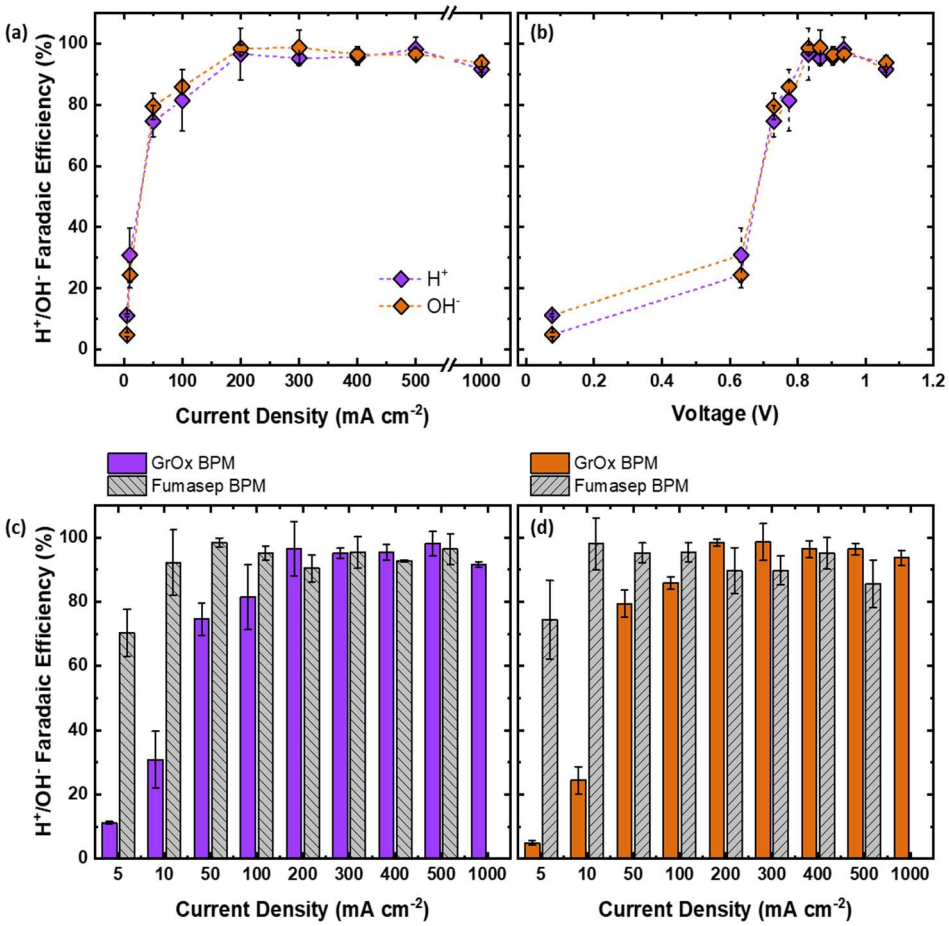

Figure 2.4 FE for H^+ and OH^- vs. current density (a) and voltage (b) for the best performing GrOx BPM (225 μg cm^{-2} GrOx loading) and comparison of FE for the GrOx BPM vs. a commercial Fumasep BPM for H^+ (c) and OH^- (d).

Further experiments were performed on the GrOx catalyzed, asymmetric BPMs with varied loading of GrOx ink, ranging from 75 to 325 μg cm^{-2}. The mass loading of the GrOx catalyst was varied by changing the number of layers of catalyst ink spin-coated onto the Nafion CEL during BPM fabrication. An optimal mass loading of 225 μg cm^{-2} was observed in the polarization characteristics of the GrOx catalyzed, asymmetric BPMs, where further increasing or decreasing the mass loading lowered the BPM performance (**Figure 2.5**). This trend was investigated

further using electrochemical impedance spectroscopy (EIS). The EIS data were fitted with a simple standard Randles circuit containing three elements (**Figure S2.7**): the resistance of the bulk electrolyte and bulk membranes between the two Luggin capillary tips (R_Ω), the resistance due to WD (R_{WD}), and the capacitance of the BPM junction (C_{WD}).[43,93] **Figure 2.5C** shows the relationship between the WD resistance, R_{WD}, and the GrOx catalyst loading. The R_{WD} was the lowest for the BPM at a catalyst mass loading of 225 μg cm^{-2}, exhibiting an identical trend as demonstrated by the polarization characteristics in **Figure 2.5A and 2.5B**.

The same trend was also observed for the BPM junction capacitance as a function of the GrOx catalyst loading (**Figure 2.5D**), where the junction capacitance was maximized at a mass loading of 225 μg cm^{-2}. As capacitance can be correlated with the number of (de)protonatable sites at the BPM junction, these data suggest a maximum number of catalytic sites for 3 layers of GrOx. Increased capacitance and activity from 1-3 layers of GrOx indicates that the catalyst coverage at the BPM junction is increasing, which is also supported by optical images and illustrations presented in **Figures 2.5E – 2.5G.** The optical images and supporting diagrams, also depict that upon introduction of layers 4 and 5, GrOx noticeably aggregates, likely leading to the coverage of a percentage of the active sites available with 3 layers of GrOx.

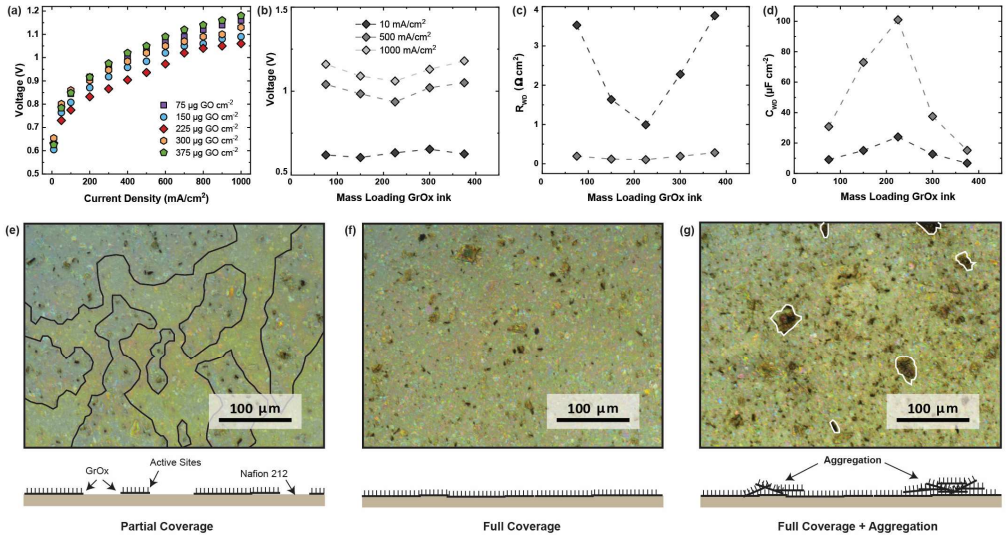

Figure 2.5 Effects of catalyst mass loading on WD enhancement in GrOx catalyzed, asymmetric BPM. (a) Polarization curves of BPMs with mass loading of 75-375 µg cm^{-2} of GrOx ink. Voltage (b), R_{WD} (c), and C_{WD} (d) vs. GrOx mass loading at 10, 500, and 1000 mA cm^{-2}. Optical images and supporting diagrams of (e) 1 layer of GrOx on Nafion 212, showing partial coverage of active sites (outlined in black), (f) 3 layers of GrOx on Nafion 212, showing full coverage, and (g) 5 layers of GrOx on Nafion, showing full coverage and aggregation (outlined in white).

To elucidate the mechanism of WD within the BPM, as well as the sensitivity of the BPM performance to CL properties, a continuum-level model of the BPM was developed. The model employed a continuum representation of mass conservation in which the species fluxes were defined by the Poisson–Nernst–Planck equations and homogeneous-phase bulk reactions in the BPM domain (i.e., WD) were described by mass-action chemical kinetics with electric-field enhancement. Simulation of the electric-field enhanced WD in the CL and ionic transport in the polymer and electrolyte layers reproduced the experimental polarization curves of the GrOx-catalyzed, asymmetric BPM with a high degree of accuracy (**Figure 2.6A**). Additionally, the model was able to accurately simulate measured salt crossover (**Figure 2.6A, red lines and markers**) and FEs (**Figure 2.6B**) for acid and base

generation. The model also was able to define local pH and electrostatic potential profiles within the BPM and CL domains, demonstrating how the pH gradient within the BPM develops as voltage increases. Interestingly, it can be observed that most of the pH and applied potential gradient occurs at the AEL-CL interface, suggesting that WD occurs primarily at this interface.

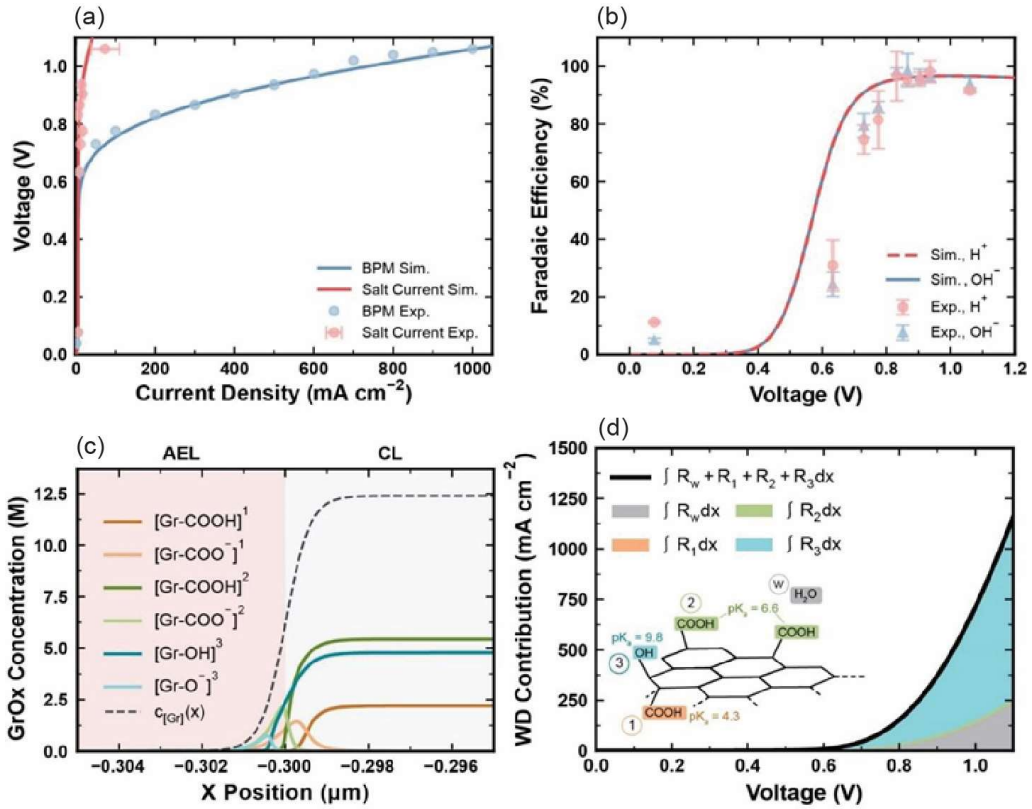

Figure 2.6 Simulation of GrOx BPM. (a) Experimental (markers) and simulated (solid lines) polarization curves for total current density (blue) and salt-ion crossover (red). (b) Experimental (markers) and simulated (lines) FE of H^+ and OH^- generation by the BPM in the catholyte and anolyte, respectively. (c) Concentration profiles of GrOx species at the catalytic AEL|CL interface where the bulk of WD occurs for an operating current density of 100 mA cm^{-2}. (d) Breakdown of WD current density due to various WD pathways **(Figure 2.1A)** integrated within the BPM CL. Orange area represents contribution to WD by R_1. Green area represents contribution to WD by R_2. Blue area represents contribution to WD by R_3. Grey area represents contribution to WD by intrinsic WD pathway.

Analysis of the local electric field within the BPM CL reveals that the maximum in the electric field at the AEL-CL interface coincides with the maximum the rate of WD via the Second Wien Effect (see SI). The local maximum in electric field can be explained by examining the concentration profiles of the GrOx functional groups within the CL (**Figure 2.6C**). Local generation of OH^- anions at the AEL-CL interface causes the most acidic GrOx functional groups (i.e., carboxylic groups) to deprotonated rapidly, resulting in a large buildup of negative charge at that interface, which, in turn, enhances the local electric field and accelerates the WD reaction via the Second Wien Effect. This finding is consistent with prior studies that suggest that the role of the catalyst is to develop surface charges that enhance the electric field and drive WD.[32,82,94] Examination of alternative WD pathways, along with experimentally determined concentrations of ionizable groups in the GrOx catalyst, shows that WD occurs primarily via the reaction of H_2O with the least acidic GrOx functional groups (i.e., phenolic groups) **(Figure 2.6D)**. The occurrence of WD at substantial rates by a catalyzed pathway has not been theoretically or experimentally reported before, as many prior simulations of WD observed that the uncatalyzed, but electric-field-enhanced, WD is dominant, and that the role of the catalyst is solely to assist in forming the electric field.[32,82,94] By contrast, these simulations show that the more acidic GrOx sites serve to enhance the electric field and the least acidic GrOx sites provide additional pathways for WD. The phenolic sites are still present in > 2 M concentrations at 100 mA cm^{-2} (**Figure 2.6C**). Thus, the different pK_as of the acidic groups on GrOx and their high concentration within the CL (see titration in **Section S2.5.6**) are the reason that GrOx exhibits dual functionality.

To determine the extent to which the pK_a of different acidic groups in the CL affects the rate of WD, simulations of the BPM were carried out in which all sites in the CL were set to a single pK_a value equal to that of one of the pK_as associated with phenolic and carboxylic groups in GrOx (i.e., either pK_a = 4.3, 6.6, or 9.8). These single-site simulations were found to be consistent with those reported by Lin *et al.* who found that as the pK_a of the catalyst decreases, its WD performance improves because the acidic groups on the catalyst dissociate more readily, thereby enhancing the electric field and accelerating the rate-limiting step in WD.[82] For low pK_a (4.3 or 6.6) functional groups, WD occurs primarily via the electric-field-enhanced process, and catalyzed WD does not occur to a significant extent because of the lack of neutral sites at the AEL-CL interface.[82,94] Conversely, for higher pK_a (9.8) functional groups, catalyzed WD becomes the dominant reaction pathway, because the pK_a is sufficiently large to prevent full deprotonation. However, because there is substantially less negative charge at the AEL-CL interface in this case, the electric field, and thus the rate of WD, are significantly lower. Intriguingly, for a single pK_a = 4.3 site, the theoretical current density is much higher than for the case of multiple acidic site GrOx due to the increase in the concentration of dissociated sites, implying that the role of the electric field enhancement is more critical to dictating WD performance. Nonetheless, the coexistence of multiple sites on the GrOx enables the passage of WD through a catalyzed mechanism, and the multi-site GrOx CL vastly outperforms the simulated single site catalysts with $pK_a > 5$.

Continuum-level modeling also helps elucidate experimental trends observed when the mass loading of the GrOx catalyst is increased. The simulations reveal that

changes in CL thickness alone cannot explain the observed trends in WD rate because WD is assumed to occur at the AEL-CL interface and not within the bulk of the CL. Further modeling demonstrates that if the volumetric concentration of catalyst sites increases concomitantly with thickness from one to three layers, the performance enhancements observed experimentally can be explained. Such an increase in the volumetric concentration of GrOx sites could result from an increase in the exposed GrOx surface with increasing CL thickness, consistent with the schematic of the GrOx structure deduced from the EIS analysis shown in **Figure 2.5.** While this hypothesis provides a possible explanation for the observed trends with increasing CL thickness, more detailed experimental measurements, will be required to resolve fully the effects of CL thickness on WD performance in BPMs.[95,96]

2.3 Conclusion

This study reports the successful development of a GrOx catalyzed, asymmetric BPM that overcomes water transport limitations and operates in reverse bias at high current density and low overpotentials, with high efficiencies for acid and base production. Evaluation of this BPM under conditions relevant for electrodialysis demonstrated stable operation for 1100 hours at 80 mA cm^{-2}, over 100 hours at 500 mA cm^{-2}, and over 60 hours at 1 A cm^{-2}. Additionally, at an applied current density of 1 A cm^{-2}, the BPM exhibits an overpotential of only 242 mV and a Faradaic efficiency (FE) for acid and base generation near unity. Additionally, the combination of anion exchange layer (AEL), cation exchange layer (CEL), and catalyst (PiperION, Nafion, and GrOx) chosen for the BPM enables excellent adhesion at the BPM junction, which contributes to its long-term stability. Initial testing of the BPM in an electrodialysis cell stack with a scaled active area of 6 cm^2 also demonstrated high current density operation at low voltage.

The performance of the BPM was also optimized by varying the loading of the GrOx catalyst. This effort revealed that an optimum in loading exists, whereas too low loading results in patchy coverage of the membrane interface by GrOx, which reduces the catalyst site concentration, and too high a catalyst loading results in catalyst agglomeration and a similar loss of sites. Furthermore, continuum-level modeling of the BPM closely matches the experimentally measured polarization curves and FEs. These simulations revealed that high concentrations of both low and high pK_a deprotonation sites in the GrOx CL enhance the electric field at the AEL-CL interface and provide alternative pathways for WD, enabling its exceptional performance. In summary, this work demonstrates an efficient, freestanding BPM

that can be readily employed in a wide array of electrochemical technologies in which operation with high current densities and low voltages is desirable.

2.4 Materials and Methods

Materials: Nafion 212 (50 μm, Fuel Cell Store), Nafion 211 (25 μm, Fuel Cell Store), Nafion 115 (127 μm, Fuel Cell Store), PiperION A15R (15 μm, Versogen), PiperION 20 (20 μm, Versogen), PiperION 60 (60 μm, Versogen), Fumasep FAB-PK-130 (110-140 μm, Fuel Cell Store), Fumasep FKB-PK-130 (110-140 μm, Fuel Cell Store), Nafion D520 (5 wt% Ionomer, Fuel Cell Store, IonPower), graphene oxide paste (30 g/L, Graphene Supermarket), sodium chloride (NaCl, Sigma Aldrich), sodium hydroxide (NaOH, Pellets, Macron Chemicals), hydrochloric acid (HCl, 1.0 M and 0.1 M, J. T. Baker), potassium hydroxide (KOH, pellets, Sigma-Aldrich). All membranes were received in dry form, pretreated according to manufacturer's instructions before use, and stored in DI water (CEMs) or 1 M NaOH (AEMs). All chemicals were used as received.

Catalyst ink: Catalyst inks were made by first diluting graphene oxide paste (Graphene Supermarket) from 30 g/L to 10 g/L. The dilute graphene oxide dispersion was then mixed with Nafion D520 in a 1:1 volume ratio. The final ink solution was sonicated for at least 10 minutes prior to use.

BPM fabrication: First, a piece of purchased Nafion membrane (NR212, NR211, NR115), precut into a 1.5x1.5 cm square and soaked in DI water for at least 1 h, was placed on a glass slide and patted dry with a Kim wipe. The membrane with then taped to the glass slide on all 4 sides with Kapton tape. GrOx catalyst ink was then spin coated onto the Nafion membrane at 3000 rpm for 30 s. Next, the Nafion

membrane with GrOx was placed in an oven at 100°C for 2 min. This process of spin coating and heating was repeated if more layers, i.e., greater mass loading, was desired. Finally, the Nafion membrane with GrOx was rewetted with a few drops of DI water, sandwiched with the desired thickness of PiperION membrane, and pressed firmly between gloved fingers, taking care to press out any air pockets. All membranes were tested directly after assembly. The same methods were used for fabrication of both the 1 cm^2 and 6 cm^2 active area BPMs.

Membrane conductivity measurements: The conductivity of the all AEMs and CEMs used in this work were measured using a four-point probe on a Lake Shore FastHall Station. All measurements were taken from -10 to 10 V on fully hydrated membranes. These measurements gave an in-plane conductivity, however, as the membranes are isotropic, this is equivalent to the through plane conductivity.

Measuring mass loading of GrOx: To determine the mass loading of GrOx ink spin coated onto Nafion, the Nafion membranes taped to glass slides were weighed before and after spin coating using a Sartorius CP Series electronic microbalance. Before weighing, the Nafion taped to a glass slide, was dried at 100°C for 10 min so that the measurements would not be affected by a change in hydration after the GrOx ink was added and heat treated. After the GrOx was spin coated onto the Nafion and heated, a Kim wipe was used to remove excess GrOx ink from the tape and glass. The final loading amount was calculated based on the exposed Nafion area within the tape border.

Electrodialysis cell design/assembly: Figure S2.1 shows a schematic of the electrodialysis cell used for testing the BPMs in this work. The cell consisted of, from

left to right in schematic, an anode, an anolyte chamber, a CEM, a dilute chamber, an AEM, an acid chamber, a BPM (1 cm^2 active area), a base chamber, a CEM, a catholyte, and a cathode. Both the anode and cathode consisted of Ni foil with copper tape as leads. Aqueous 1 M NaOH with used as both the anolyte and the catholyte and was recirculated through both chambers at ~10 mL/min. Aqueous 3 M NaCl was recirculated at ~5 mL/min through the dilute chamber and aqueous 0.5 M NaCl was flowed through the acid and base chambers at 0.2 mL/min. Both CEMs used in the cell stack were Nafion N324 (280 μm, Fuel Cell Store) and the AEM was Fumasep FAB-PK-130 (130 μm, Fuel Cell Store). Luggin capillaries holding Ag/AgCl reference electrodes (CHI111, CH Instruments) were placed in the acid and base chambers to allow for the most direct measurement of the voltage across the BPM.

Chronopotentiometry: After the electrodialysis cell described above was assembled, potentiostat (Biologic SP 300, Biologic SP 200, Kiethley 2400) leads were attached in a four-point measurement configuration so that a current could be applied across the full cell and the resulting voltage could be measured directly across the BPM. Chronopotentiometry measurements were used to obtain all reported data for all polarization curves. For each point, a chosen current was applied across the anode and cathode and held steady for 5-20 min or until the voltage measured across the BPM reached steady state. The current was then increased to the next value and the process was continued until all desired current measurements were performed. The reported voltage values are averages of the voltage collected over the steady state region for each chronopotentiometry step.

Electrochemical Impedance Spectroscopy (EIS): EIS measurements were performed in the same electrodialysis cell as the chronopotentiometry measurements. For each BPM tested, measurements were started at 500 mA cm^{-2} and stepped down through each desired current density. For each step, the current was held for 1 min, then scanned from 600 kHz to 20 Hz with an amplitude of 5-10% of the current, recording every 0.5 sec. Nyquist plots were then fitted using EIS Spectrum Analyzer software.

Faradaic efficiency: The same five chamber electrodialysis cell was used for collecting acid and base samples to measure the Faradaic efficiency at various current densities. Aqueous 0.5 M NaCl was flowed at 5 mL/min through the acid and base chambers and the desired current was applied across the cell until the voltage stabilized (usually 10-20 min). Samples were then collected in 20 mL vials from the acid and base chamber. The current was then increased to the next desired value and the process repeated. Once the samples were collected, the H^+ and OH^- activity was evaluated via pH probe measurements or pH titration. Titration was used for more pH values > 12 and < 2. All pH titration measurements and the subsequent calculation of theoretical H^+/OH^- concentration and Faradaic efficiency were performed as reported in Lucas *et al*.[45]

Low vacuum SEM: All SEM images were obtained using the low vacuum mode on an FEI Nova NanoSEM 450. A spot size of 5.0 and a voltage of 10.00 kV was used for most images. For the BPM cross-sectional images, the membrane was embedded in resin and cut using a microtome. For cross sections of just the Nafion with a GrOx

CL, the membranes were sliced using a razor blade. ImageJ was used to evaluate membrane and CL thickness from these SEM cross sections.

Optical Microscopy: All optical microscope images were obtained using a Nikon Eclipse LV100D-U. Images of GrOx dispersions were taken during the BPM fabrication process, while Nafion and GrOx-coated Nafion remained taped to glass slides before they we rewetted and sandwiched with the AEM.

AFM: An Asylum AFM in AC Air Topography mode was used for topological and roughness measurements of the membrane and GrOx layer surface. As with the optical microscope images, AFM was performed on Nafion and GrOx-coated Nafion prior to the samples being rewetted and sandwiched with the AEM.

Continuum simulation: The simulation was performed using the COMSOL Multiphysics v.6.0 software package. The concentration of H_3O^+, OH^-, Na^+, Cl^-, and of all GrOx surface species along with the electrostatic potential profile were solved using conservation equations where Poisson-Nernst-Planck described mass and charge transport. Crucially, the rates of net-charge-generating homogeneous reactions were modified by the Second Wien effect such that the rate of ion dissociation, i.e., the forward direction, was substantially enhanced by an electric field. [94,97,98]

2.5 Supporting Information

2.5.1 Bipolar Membrane Experimental Design and Analysis

To accurately understand the performance of bipolar membranes (BPMs) for electrodialysis, it is important to be able to directly measure the voltage across the BPM without interference from electrolyte resistance or redox reactions.[45] Luggin capillaries with reference electrodes can be implemented into H-Cells to measure the BPM voltage as close to the surface of the membrane as possible. However, in a simple H-Cell configuration, equilibrium at each applied current density cannot be reached as the acid and base concentration will continue to increase (especially directly at the surface of the BPM) for the entire duration the bias is applied. To overcome these challenges for electrochemical testing of BPMs, we designed a custom electrodialysis cell with embedded Luggin capillaries that also allows electrolyte to be flowed through each chamber (**Figure S2.1**). Furthermore, to guarantee equilibrium during experiments, fresh solution was continuously flowed through each chamber of the electrodialysis cell, and the acid/base chambers were agitated using small magnetic stir bars with a plate placed under the cell. Using accurate pumps to set specific flow rates, **Equations S2.1-S2.8** were used to calculate the theoretical concentration of H^+ and OH^- in the acid and base chambers of the electrodialysis cell.

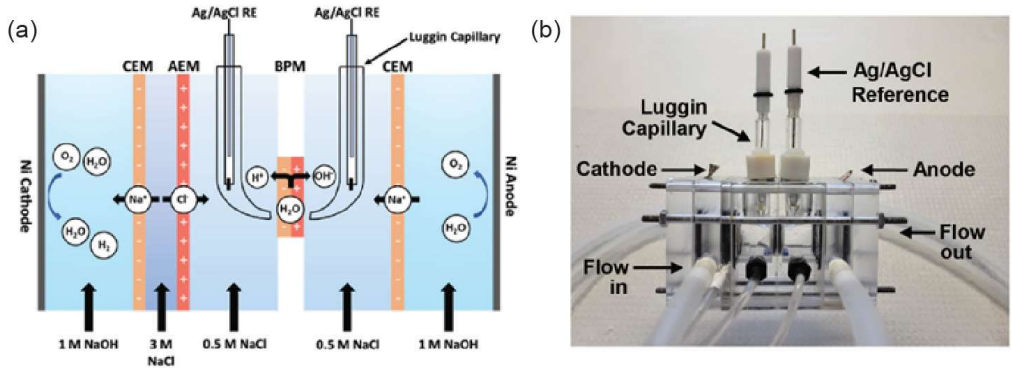

Figure S2.1 Electrodialysis flow cell. (a) Cross section schematic of electrodialysis cell designed for direct testing of bipolar membranes. (b) Image of actual flow cell, showing Luggin capillaries, reference electrodes, anode, cathode, and flow channels. Luggin capillaries with Ag/AgCl reference electrodes are implemented to allow for direct measurement of the BPM voltage without interference from electrolyte resistance. The tips of the capillary tubes are placed approximately 0.1 mm from the surface of the BPM. The BPM active area in the custom cell is 1 cm^2. The AEM, CEMs, anode, and cathode all have an active area of 4 cm^2.

It is also important to note that since the concentration of acid and base increases as current density is stepped up, the solution conductivity increases as well and therefor the solution iR drop cannot be accurately calculated directly from the initial salt conductivity (**Figure S2.4**). As equilibrium can be achieved in the custom electrodialysis cell by flowing and stilling the acid and base chamber solutions, **Equation S9** can be implemented to calculate the ohmic contribution from the acid and base solutions. In **Equation S9** J is the current density, $\kappa_{solution}$ is the conductivity of NaCl, HCl, or NaOH based on the current density and flow rate, and d is the distance of the Luggin capillary tips from the BPM surface (~0.01 cm). Conductivity value for 0.5 M NaCl and varying concentrations of HCl and NaOH were obtained from literature.[99–101] Furthermore, the calculated equilibrium acid and base concentrations were used with **Equation S10** to calculate the Nernstian

thermodynamic potential necessary for WD at a specific current density and flow rate.[9] The final iR contributions, from the AEL and CEL, were then calculated using **Equation S11** along with membrane conductivity values measured using a four-point probe system (see Methods).

$$G_{H^+} = \frac{I_{applied}}{nF} \tag{S2.1}$$

$$[H^+]_{added} = \frac{G_{H^+}}{Q_{0.5\ M\ NaCl}} \tag{S2.2}$$

$$[H^+]_{present} = 10^{-6.85} \tag{S2.3}$$

$$[H^+]_{theoretical} = [H^+]_{added} + [H^+]_{present} \tag{S2.4}$$

$$G_{OH^-} = \frac{I_{applied}}{nF} \tag{S2.5}$$

$$[OH^-]_{added} = \frac{G_{OH^-}}{Q_{0.5\ M\ NaCl}} \tag{S2.6}$$

$$[OH^-]_{present} = \frac{10^{-13.71}}{10^{-6.85}} \tag{S2.7}$$

$$[OH^-]_{theoretical} = [OH^-]_{added} + [OH^-]_{present} \tag{S2.8}$$

$$iR_{solution} = \frac{J * d}{\kappa_{solution}} \tag{S2.9}$$

$$E_{WD,Thermo} = 0.059(pH_{base} - pH_{acid}) = 0.059\Delta pH \tag{S2.10}$$

$$iR_{AEM/CEM} = \frac{J * \Delta x}{\kappa_{AEM/CEM}} \tag{S2.11}$$

$$Efficiency_{WD} = \frac{E_{WD,Thermo}}{V_{BPM}} \times 100 \tag{S2.12}$$

To determine overpotentials for all BPMs compared in **Figure 2.2C**, the thermodynamic WD potential was subtracted from reported operating voltages at 100, 500, and 1000 mA cm^{-2}. Values for reported voltages from each reference were

obtained using ImageJ measurement tool on reported polarization curves. Thermodynamic WD potentials for each BPM study were calculated based on the individual testing environment described in reported materials and methods, with the three general testing environments and how they were evaluated listed below. We note that these calculations do not account for co-ion leakage through the BPMs as it was not reported for all systems. However, if the Faradaic efficiency of H^+ and OH^- production is near unity, these differences would be minimal.

- For systems that used flow cells with salt water, the thermodynamic WD potential was calculated using the same method reported above.
- For systems that used acid and base fed flow cells, the acid and base concentration reported for the feed solutions was used with **Equation S10**.
- For stagnant systems, using H-cells, the flow rate value in the calculations of acid and base concentration was replace with the approximate amount of solution present and amount of time that a specific current density was applied.

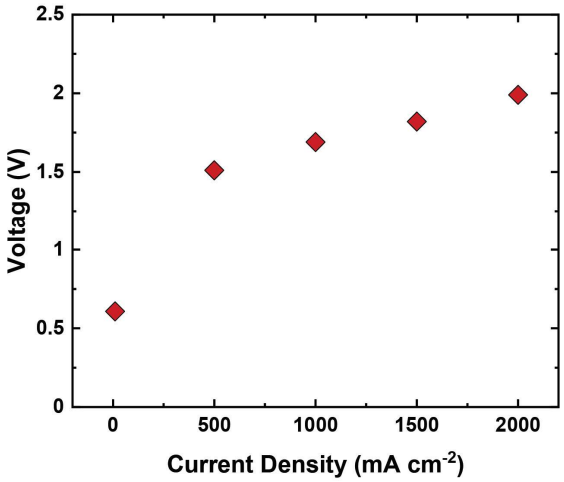

Figure S2.2 Current density vs. voltage curve of thin AEL BPM with 75 µg cm^{-2} of GrOx ink at the BPM junction operated up to 2 A cm^{-2}.

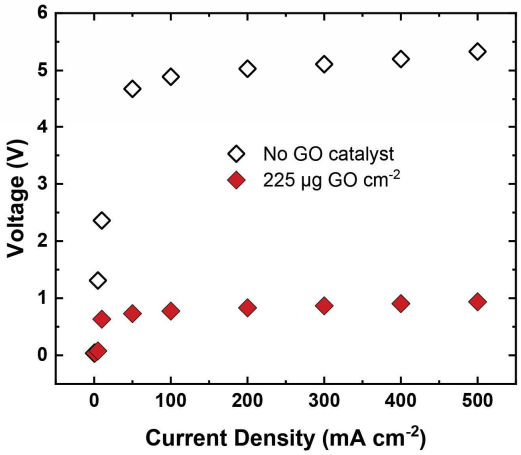

Figure S2.3 Current density vs. voltage of top performing GrOx catalyzed, asymmetric BPM compared to same BPM construction without GrOx catalyst at the junction. The significantly lower voltage of the catalyzed BPM demonstrates that although WD is enhance due to the electric field at the AEL/CEL junction, implementation of a catalyst at the BPM inner layer can significantly further enhance the rate of WD.

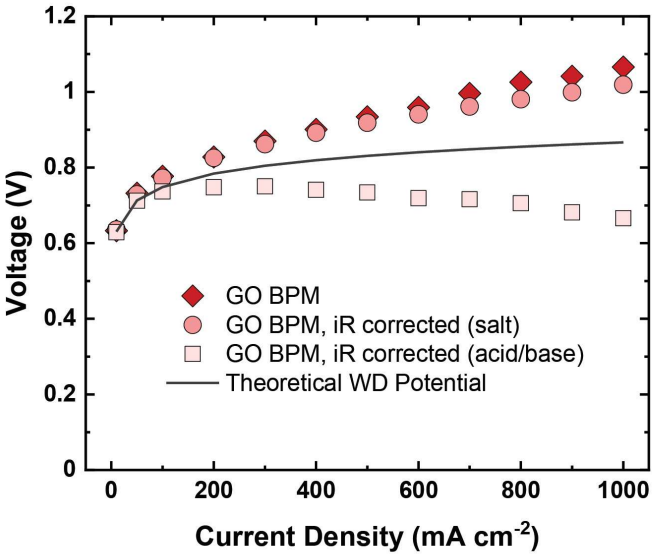

Figure S2.4 Top performing GrOx catalyzed, asymmetric BPM voltage as measured (diamonds), voltage minus iR calculated based on salt conductivity (squares), and voltage minus iR calculated based on acid/base conductivity (circles). This shows the importance of calculating solution resistance voltage contributions based on the changing conductivity as the solutions are acidified and basified.

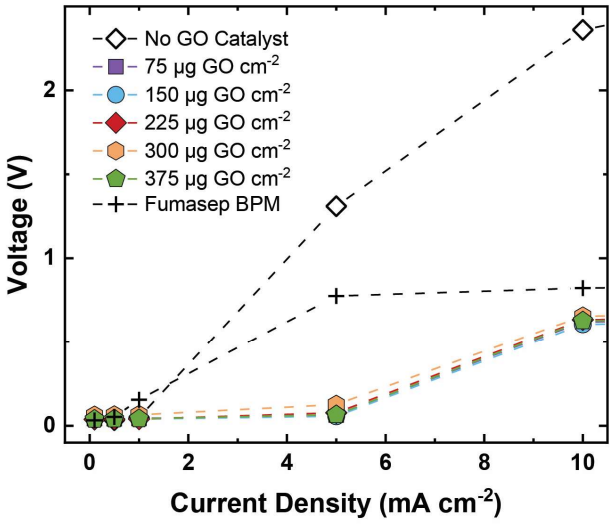

Figure S2.5 Current density vs. voltage plot comparing GrOx BPMs to BPM with no catalyst and commercial Fumasep BPM at low currents. BPMs with GrOx show greater co-ion leakage than those without GrOx.

Table S2.1 Details about each of the top performing BPMs compared in this paper.

#	Ref	μ (mV) @ 100 mA cm^{-2}	μ (mV) @ 500 mA cm^{-2}	μ (mV) @ 1000 mA cm^{-2}	Stability	Cell Geometry	Temp (°C)	CEM	AEM	Catalyst	Electrolyte
1	This Work	126	145	242	1100 h @ 80 mA cm^{-2} 106 h @ 500 mA cm^{-2} 65 h @ 1000 mA cm^{-2}	5 Chamber Cell w/ Luggins	25	Nafion 212	PiperION 15R	Graphene oxide	0.5 M NaCl
2	Powers, D. et al. Freestanding Bipolar Membranes with an Electrospun Junction for High Current Density Water Splitting. Cite This: ACS Appl. Mater. Interfaces 14, 36092−36104 (2022).	242	368	584	60 h @ 800 mA cm^{-2} (Not continuous)	H-Cell w/ Luggins	25	Electrospun SPEEK	Electrospun QPPO	Graphene oxide, $Al(OH)_3$	0.5 M Na_2SO_4
3	Hohenadel, A. et al. Electrochemical Characterization of Hydrocarbon Bipolar Membranes with Varying Junction Morphology. ACS Appl Energy Mater 2, 6817−6824 (2019).	244	-	-	-	H-Cell w/ Luggins	25	SPPB	HMT-PMBI	$Al(OH)_3$	0.5 M Na_2SO_4
4	Chen, Y. et al. High-Performance Bipolar Membrane Development for Improved Water Dissociation. ACS Appl Polym Mater (2020) doi:10.1021/acsapm.0c00653.	301	670	-	14 h @ 500 mA cm-2 (steady voltage increase)	4 Chamber Cell w/ Luggins	25	Electrospun Nafion	Electrospun PFEAM	Graphene oxide	1 M NaOH, 1 M H_2SO_4
5	Shen, C., Wycisk, R. & Pintauro, P. N. High performance electrospun bipolar membrane with a 3D junction. Energy Environ Sci 10, 1435−1442 (2017).	339	314	483	-	H-Cell w/ Luggins	25	Electrospun SPEEK	Electrospun QPPO	10 wt% $Al(OH)_3$	0.5 M Na_2SO_4
6	McDonald, M. B. & Freund, M. S. Graphene oxide as a water dissociation catalyst in the bipolar membrane interfacial layer. ACS Appl Mater Interfaces 6, 13790−13797 (2014).	491	-	-	-	H-Cell w/ Luggins	25	Nafion 211	Neosepta AHA	Graphene Oxide	1 M $NaClO_4$
7	Yan, Z. et al. The balance of electric field and interfacial catalysis in promoting water dissociation in bipolar membranes ↑. Energy Environ. Sci 11, 2235 (2018).	539	-	-	10 h @ 100 mA cm-2	4 Chamber Cell w/ Luggins	25	Nafion	-	Graphene Oxide	0.5 M KNO_3
8	Al-Dhubhani, E. et al. Entanglement-Enhanced Water Dissociation in Bipolar Membranes with 3D Electrospun Junction and Polymeric Catalyst. ACS Appl Energy Mater 4, 3724−3736 (2021).	1411	-	-	-	5 Chamber Cell w/ Luggins	25	Electrospun SPEEK	Electrospun FAA-3	P4VP (Polymer)	NaCl
9	Oener, S. Z., Foster, M. J. & Boettcher, S. W. Accelerating water dissociation in bipolar membranes and for electrocatalysis. Science (1979) 369, 1099−1103 (2020).	894	-	-	4 h @ 500 mA cm-2 (steady voltage increase)	Compressed MEA	50	2 μm Nafion	50 μm Sustainion	TiO_2 and NiO	water, 1 M HCl/ 1 M NaOH
10	Oener, S. Z., Twight, L. P., Lindquist, G. A. & Boettcher, S. W. Thin Cation-Exchange Layers Enable High-Current-Density Bipolar Membrane Electrolyzers via Improved Water Transport. ACS Energy Lett 6, 1−8 (2021).	844	1394	1724	4 h @ 1000 mA cm-2 (1 h stable, 3 h steady voltage increase)	Compressed MEA	50	2 μm Nafion	50 μm Sustainion	TiO_2 and NiO	water, 1 M HCl/ 1 M NaOH
11	Fumasep BPM	341	1119	-	-	5 Chamber Cell w/ Luggins	25	-	-	-	0.5 M NaCl

2.5.2 Bipolar Membrane Stability

Beyond the 100 hours reported in the main text, stability measurements of over 400 hours at 500 mA cm^{-2} were also obtained, however, they showed a small but steady climb in voltage through the entire measurement period. By examining BPMs before and after stability tests, it was observed that the Nafion 212 membranes were irreversibly warping and pitting at the BPM junction (**Figure S2.6**). The same pitting in the Nafion 212 was observed when membranes were heated in a furnace at 150°C for ~10 minutes. During chronopotentiometry experiments, the temperature measured in the bulk 0.5 M NaCl electrolyte on either side of the BPM was ~35°C at 500 mA cm^{-2} and ~50°C at 1 A cm^{-2}, indicating that it was likely even higher in the BPM itself. To further understand possible temperature effects on the membranes, 3D modeling of the custom electrodialysis cell was performed using COMSOL. These models indicate that the temperature in the BPM is reaching an estimated 42°C at 500 mA cm^{-2} and 80°C at 1 A cm^{-2} (**Figure S2.13**). From these temperature measurements and modeling results, it was determined that heating in the membrane

due to high current densities was the cause of the Nafion deformation leading to slow delamination and voltage ramping in stability tests. To overcome this delamination challenge, multiple other Nafion membranes (Nafion 211, Nafion 115, and Nafion 117) were heated in a furnace to 150°C for 10 minutes. Out of the three membranes heated, Nafion 211 was the only one that did not exhibit deformation, therefore, new BPMs were fabricated with Nafion 211 in place of the Nafion 212. When the BPMs with Nafion 211 were stability tested, they maintained a consistent voltage over more than 100 hours, indicating that the membranes were no longer deforming and delaminating (**Figure S2.6**).

It should be noted that the potentials reported in the GrOx catalyzed, asymmetric BPM stability measurements are slightly higher than those reported in the current density vs. voltage plots. During stability testing, bubbles begin to evolve from dissolved air in the electrolyte due to elevated temperature when operating for long periods of time at high current densities. The higher reported potentials therefor, are due to the evolution of gas bubbles on the BPM surface, which effectively reduces the active area.

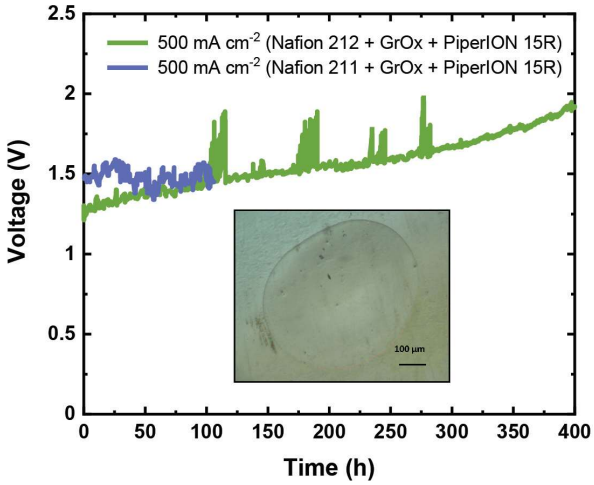

Figure S2.6 Stability plots comparing BPMs made with Nafion 212 and Nafion 211. Nafion 211 has superior stability and does not climb in voltage over time as Nafion 212 membranes do. The picture insets depict the irreversible pitting and warping that occurs in the Nafion 212 membranes due to high temperatures reached in the cell when testing at large current densities.

2.5.3 Characterization and Analysis of GrOx Loading

Table S2.2 List of the main BPMs, and their properties, fabricated and tested in this work.

Name	CEL	AEL	Catalyst	Layers of Catalyst	Mass Loading of Catalyst (µg cm^{-2})	Catalyst Layer Thickness (nm)
BPM 0	Nafion 212	PiperION 15R	GrOx ink	0	0	0
BPM 1	Nafion 212	PiperION 15R	GrOx ink	1	75	200
BPM 2	Nafion 212	PiperION 15R	GrOx ink	2	150	400
BPM 3	Nafion 212	PiperION 15R	GrOx ink	3	225	600
BPM 4	Nafion 212	PiperION 15R	GrOx ink	4	300	800
BPM 5	Nafion 212	PiperION 15R	GrOx ink	5	375	1000
BPM 6	Nafion 211	PiperION 15R	GrOx ink	3	225	600

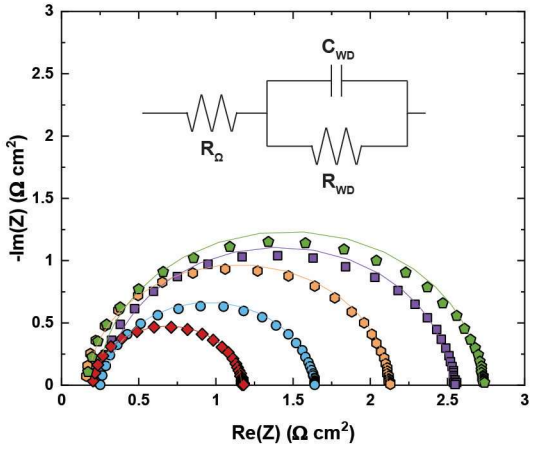

Figure S2.7 Nyquist plots for thin AEL BPMs with varying GrOx loading amounts at 50 mA cm^2. The inset shows the circuit that was used to fit the EIS data. R_Ω is the resistance between the tips of the Luggin capillaries, which includes the solution and the membranes, R_{WD} is the resistance due to the water dissociation reaction, and C_{WD} is the capacitance due to a double layer build up at BPM inner layer.

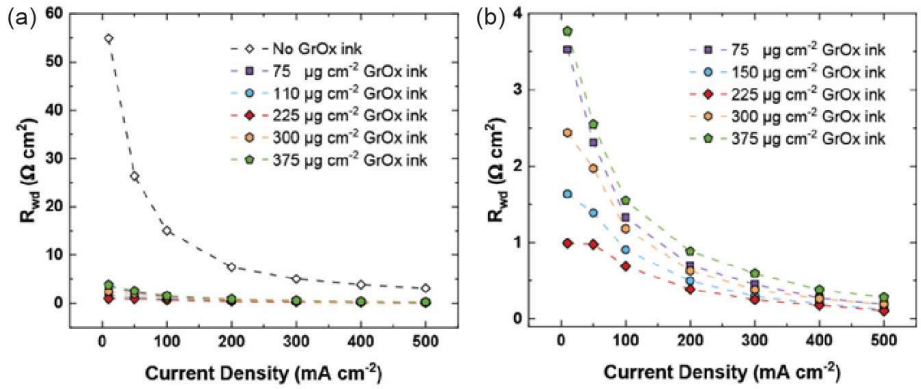

Figure 2.8 Current density vs. R_{WD} plots comparing BPMs with and without catalyst ink (a) and comparing loading amounts of GrOx catalyst ink (b).

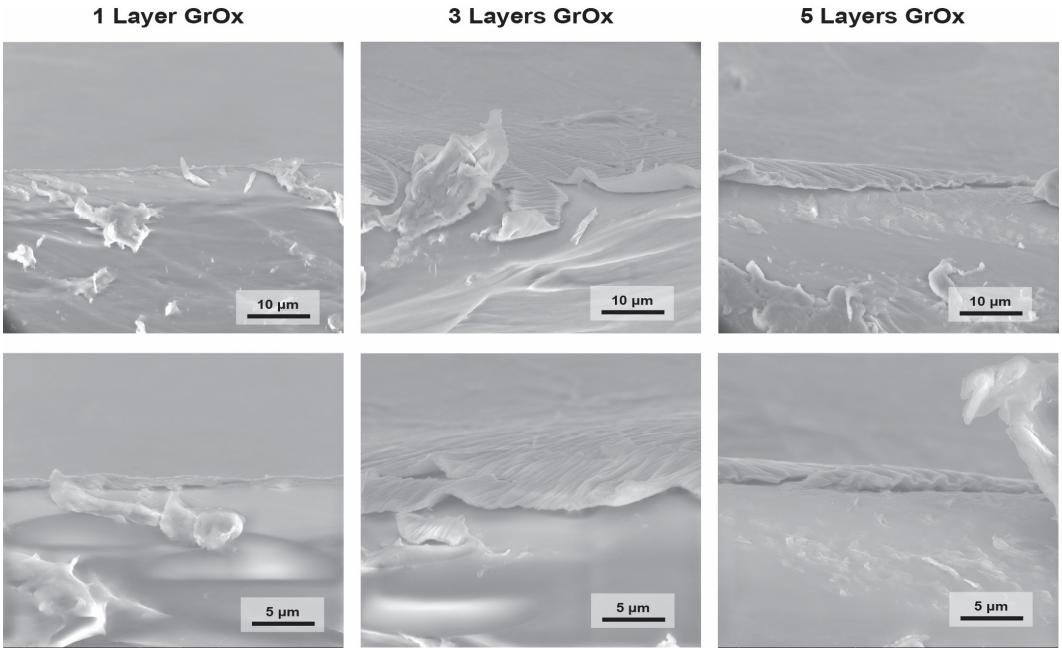

Figure S2.9 SEM cross sectional images of 1, 3, and 5 layers of GrOx ink spin coated onto Nafion 212. Cross sections were obtained by slicing dry membranes with a razor blade and mounting at 90°.

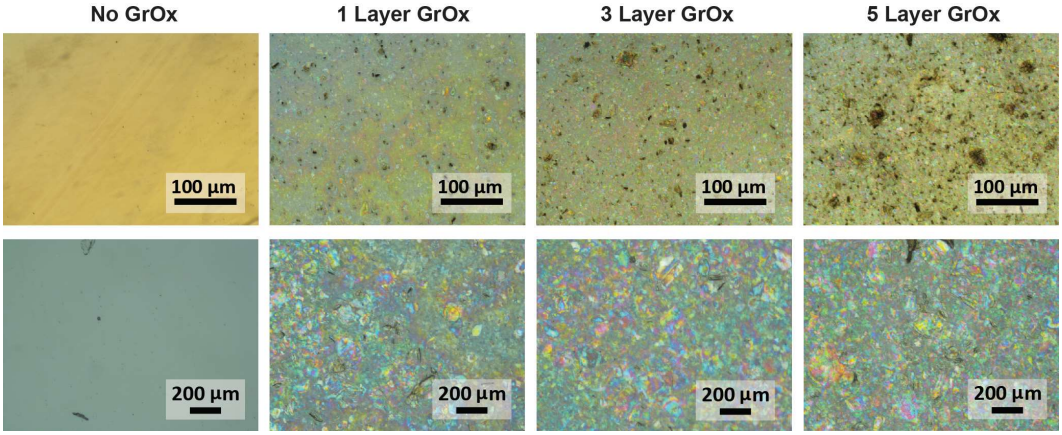

Figure S2.10 Optical images of 1, 3, and 5 layers of GrOx ink spin coated onto Nafion 212 at 5x magnification (top row) and 20x magnification (bottom row).

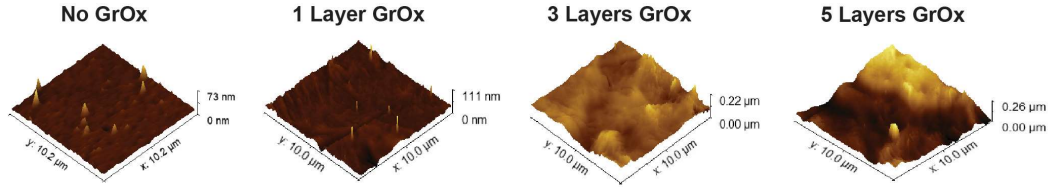

Figure S2.11 AFM scans of 0, 1, 3, and 5 layers of GrOx ink spin coated onto Nafion 212.

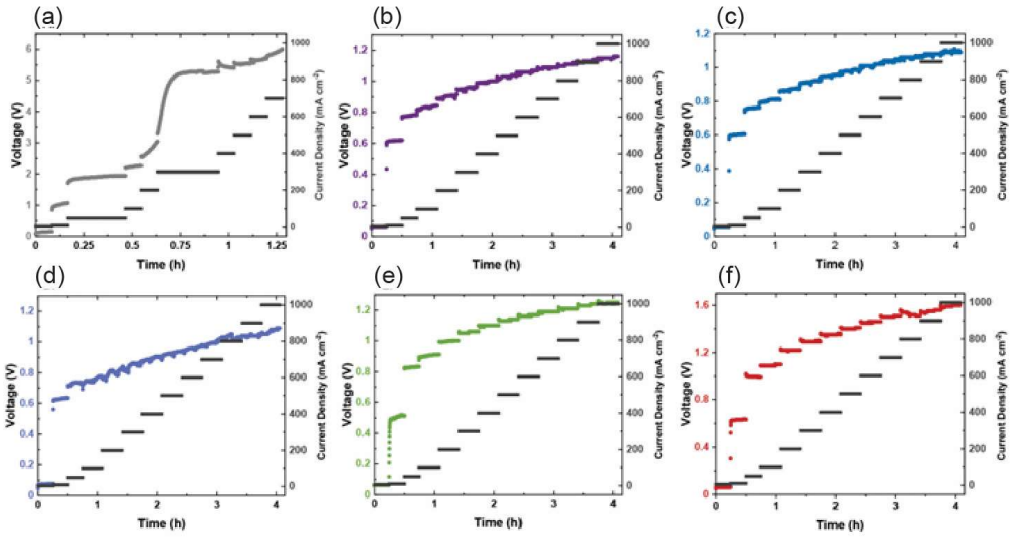

Figure S2.12 Voltage and current density vs. time plots for BPMs with no catalyst (a), 1 layer GrOx (b), 2 layers GrOx (c), 3 layers GrOx (d), 4 layers GrOx (e), and 5 layers GrOx (f).

2.5.4 Cell and Membrane Temperature Model

A 3-D temperature simulation for the custom electrodialysis cell used in this work was carried out using a multi-physics finite element model featured with current distribution, resistive heating, and fluid dynamics. The current distribution is simulated assuming a primary current model in which the current density distribution is simulated with an assigned conductivity for the electrolyte and ion-exchange membrane domains instead of explicitly resolving the ion concentration and flux. Three average current density values (80, 500, 1000 mA cm^{-2}) were applied as the boundary condition. The current distribution inside the cell is plotted in the top row of **Figure S2.13** with sliced heat maps indicating the magnitude of the local current density and arrows depicting both the direction and the magnitude of the current density vector.

Other than in the BPM domain, the local heating power per unit volume is calculated based on the local current density and conductivity by the differential form of Joule heating equation.

$$\frac{dP}{dV} = \frac{1}{\sigma} J^2 \tag{S13}$$

where σ is conductivity and J is the current density. In the BPM domain, a portion of the potential is consumed as the energy to facilitate the water dissociation reaction:

$$H_2O \rightleftharpoons H^+ + OH^- \qquad \Delta\varphi = 0.83V \tag{S14}$$

Thus, the differential form of Joule heating power inside the BPM is calculated by

$$\frac{dP}{dV} = \frac{1}{\sigma} J^2 - J_z \frac{\Delta\varphi}{z_{BPM}} \tag{S15}$$

The temperature after 1 hour of operation predicted by the simulation is plotted in the bottom row of **Figure S2.13**. The temperature results from this model manifest that operating at 80 mA/cm^2 a low temperature, not exceeding 21.6°C can be maintained throughout the cell, however, when the cell is operating at 500 mA/cm^2 and 1000 mA/cm^2, the temperature reaches a maximum of 42.3°C and 80.7°C, respectively, near the cylindrical region where the BPM is located.

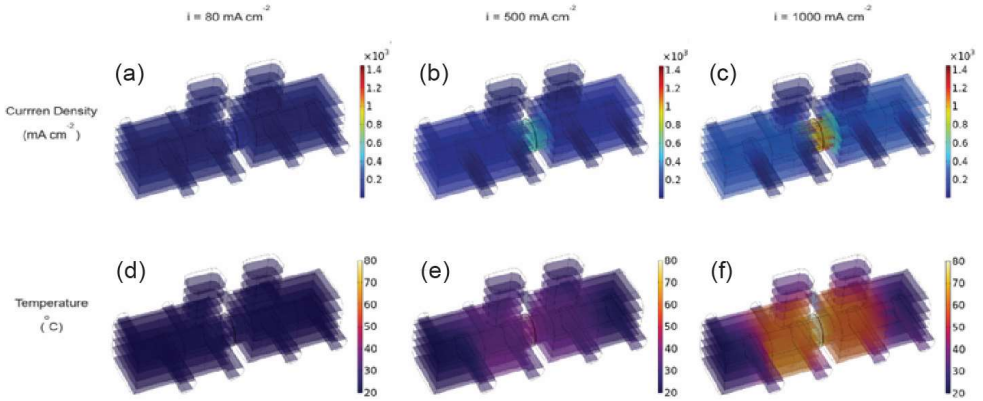

Figure S2.13 Temperature model of electrodialysis flow cell. (a-c) Primary current density distribution of 80, 500 and 1000 mA cm^{-2} average applied current density. (d-f) Temperature distribution inside the cell.

2.5.5 Analytic Hyperbolic Tangent Distributions in Model

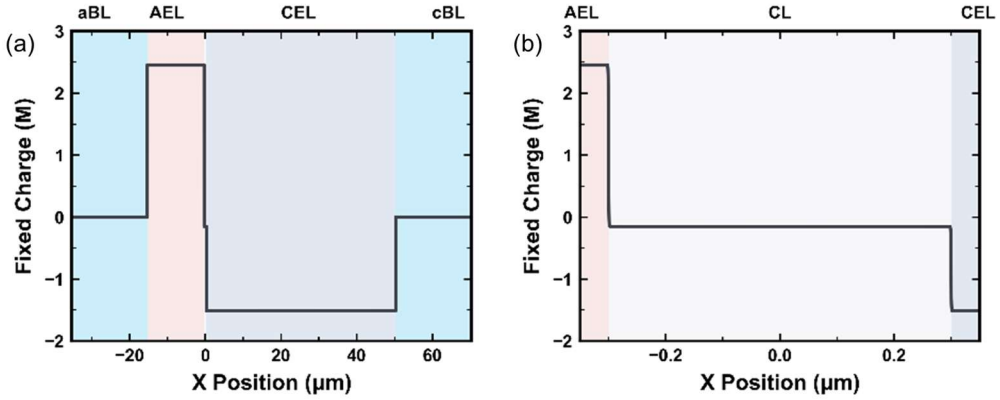

Figure S2.14 Fixed charge in BPM as a function of position for (a) entire simulation domain and (b) zoomed into catalyst layer.

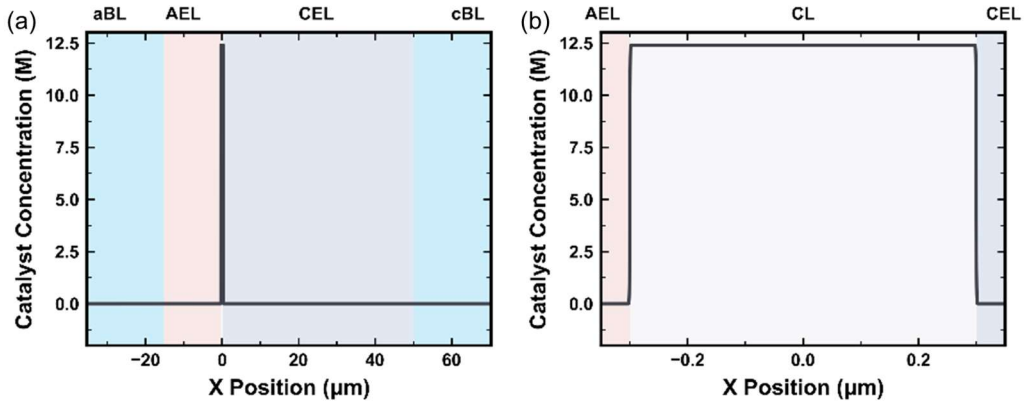

Figure S2.15 Total catalyst site distribution ($c^0_{[Gr]}(x)$) in BPM as a function of position for (a) entire simulation domain and (b) zoomed into catalyst layer.

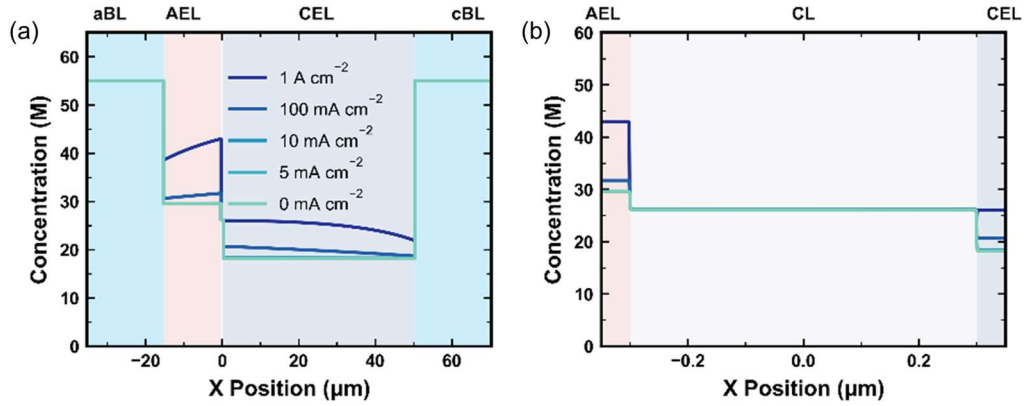

Figure S2.16 Water concentration of BPM as a function of position for (a) entire simulation domain and (b) zoomed into catalyst layer. Water concentration changes as a function of current density as BPM changes from Na^+-Cl^- form to H^+-OH^- form and water content increases.

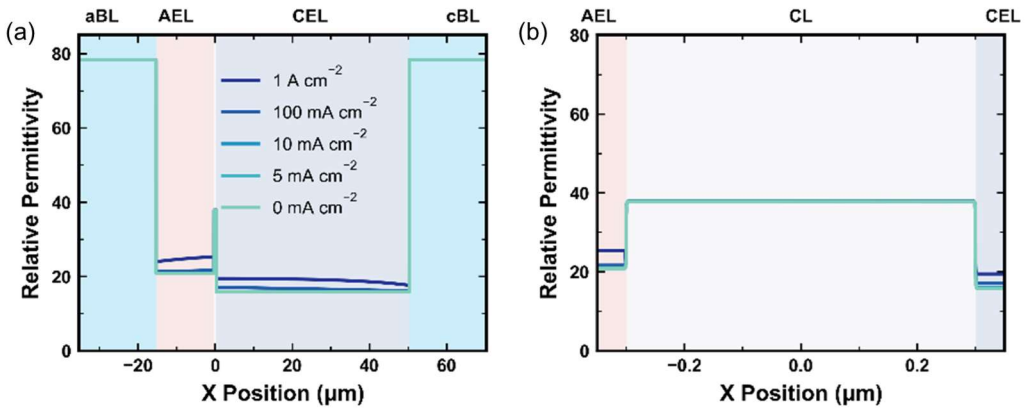

Figure S2.17 Relative permittivity of BPM as a function of position for (a) entire simulation domain and (b) zoomed into catalyst layer. Permittivity changes as a function of current density as BPM changes from Na^+-Cl^- form to H^+-OH^- form and water content increases.

2.5.6 Titration of GrOx

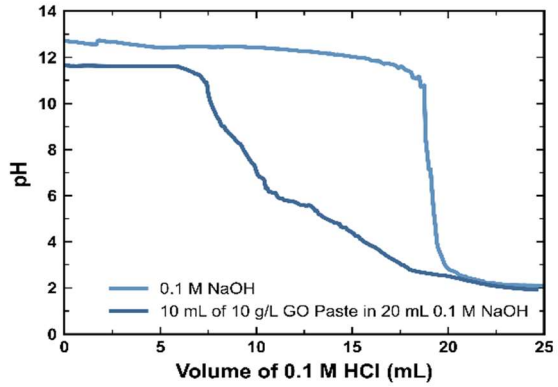

Figure S2.18 Titration of 0.1 M NaOH (light blue trace) and 10 mL of 10 g/L GROX paste added to 20 mL NaOH (dark blue trace) with 0.1 M HCl

To calculate the total number of GrOx sites available for proton transfer from the titration data collected (**Figure S2.18**), we first assume that the GrOx is in equilibrium [102]:

$$\frac{c_{[Gr-COO^-]^1}c_{H_3O^+}}{c_{[Gr-COOH]^1}} = 10^{-4.3}\ [M] \tag{S67}$$

$$\frac{c_{[Gr-COO^-]^2}c_{H_3O^+}}{c_{[Gr-COOH]^2}} = 10^{-6.6}\ [M] \tag{S68}$$

$$\frac{c_{[Gr-O^-]^3}c_{H_3O^+}}{c_{[Gr-OH]^3}} = 10^{-9.8}\ [M] \tag{S69}$$

At the equivalence point pH = 7, so $c_{H_3O^+} = 10^{-7}\ [M]$ and $c_{OH^-} = 10^{-7}\ [M]$. Additionally, we know we have added 10.05 mL of 0.1 M HCl, 20 mL of 0.1 M NaOH, and 10 mL of a 10 g/L GrOx Paste. Substituting in the known proton concentration at the equivalence point:

$$\frac{c_{[Gr-COO^-]^1}(10^{-7}\ [M])}{c_{[Gr-COOH]^1}} = 10^{-4.3}\ [M] \tag{S70}$$

$$\frac{c_{[Gr-COO^-]^2}(10^{-7}\ [M])}{c_{[Gr-COOH]^2}} = 10^{-6.6}\ [M] \tag{S71}$$

$$\frac{c_{[Gr-O^-]^3}(10^{-7}\ [M])}{c_{[Gr-OH]^3}} = 10^{-9.8}\ [M] \tag{S72}$$

To determine the equilibrium concentrations of Na^+ and Cl^-, we simply alter the starting concentrations to account for dilution.

$$c_{Cl^-} = \frac{10.05\ [mL] \times 0.1\ [M]}{10.05\ [mL] + 20\ [mL] + 10\ [mL]} = 0.0251\ [M] \tag{S73}$$

$$c_{Na^+} = \frac{20\ [mL] \times 0.1\ [M]}{10.05\ [mL] + 20\ [mL] + 10\ [mL]} = 0.0500\ [M] \tag{S74}$$

We know there must be a site balance where all of the GrOx surface species add up to a total:

$$c^0_{[Gr-COOH]^1} + c^0_{[Gr-COOH]^2} + c^0_{[Gr-OH]^3} = c^0_{Gr} \tag{S75}$$

Additionally, we know the fraction of the total sites occupied by each type of site by integration performed by prior research,[26] and that a site balance must hold for each type of site on the GO.

$$c^0_{[Gr-COOH]^1} = \frac{3}{16.9} c^0_{Gr} = c_{[Gr-COO^-]^1} + c_{[Gr-COOH]^1} \tag{S76}$$

$$c^0_{[Gr-COOH]^2} = \frac{7.4}{16.9} c^0_{Gr} = c_{[Gr-COO^-]^2} + c_{[Gr-COOH]^2} \tag{S77}$$

$$c^0_{[Gr-OH]^3} = \frac{6.5}{16.9} c^0_{Gr} = c_{[Gr-O^-]^3} + c_{[Gr-OH]^3} \tag{S78}$$

Electroneutrality is conserved in the system:

$$c_{[Gr-CO^-]^1} + c_{[Gr-COO^-]^2} + c_{[Gr-^-]^3} + c_{Cl^-} - c_{Na^+} + c_{OH^-} - c_{H_3O^+} = 0$$

Solving the system of equation enables determination of the total GrOx site concentration:

$$c^0_{Gr} = 0.0506030446[M] \tag{S79}$$

Now, we must convert back to a mole basis from the concentration basis by multiplying by the total volume of solution:

$$n^0_{Gr} = 0.0506030446\ [M] \times 40.05\ [mL] \tag{S80}$$

$$= 0.00202665194\ [moles]$$

We note that there was 0.1 g of GrOx added to the solution (10 mL of 10 [g/L] GrOx paste). Therefore, the ion exchange capacity of pure GrOx can be determined as follows:

$$IEC_{GrOx} = \frac{0.00202665194\ moles}{0.1\ [g]} = 20.2665194\ [mmol\ g^{-1}] \tag{S81}$$

Lastly, the fixed-site concentration in pure GrOx can then be determined by multiplying the IEC by the density of GrOx[103] as follows:

$$c^0_{GrOx,Pure} = IEC_{GrOx} \times \rho_{GrOx} \quad \text{(S82)}$$

$$= 20.2665194\ [mmol\ g^{-1}] \times 1.36\ [g\ cm^{-3}]$$

$$= 27.56\ [M]$$

It is important to note, however, that while the model does fit the data without significant error, the pK_as of the GrOx sites used the simulation were taken from measurements in aqueous electrolyte, which may vary from their values within the BPM junction.

2.5.7 Ion Transport

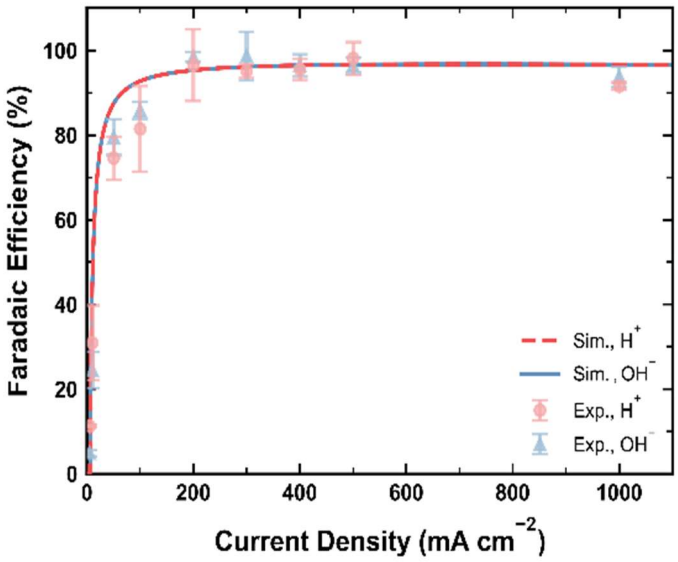

Figure S2.19 Simulated (lines) and experimentally measured (markers) Faradaic efficiency for water dissociation as a function of applied current density.

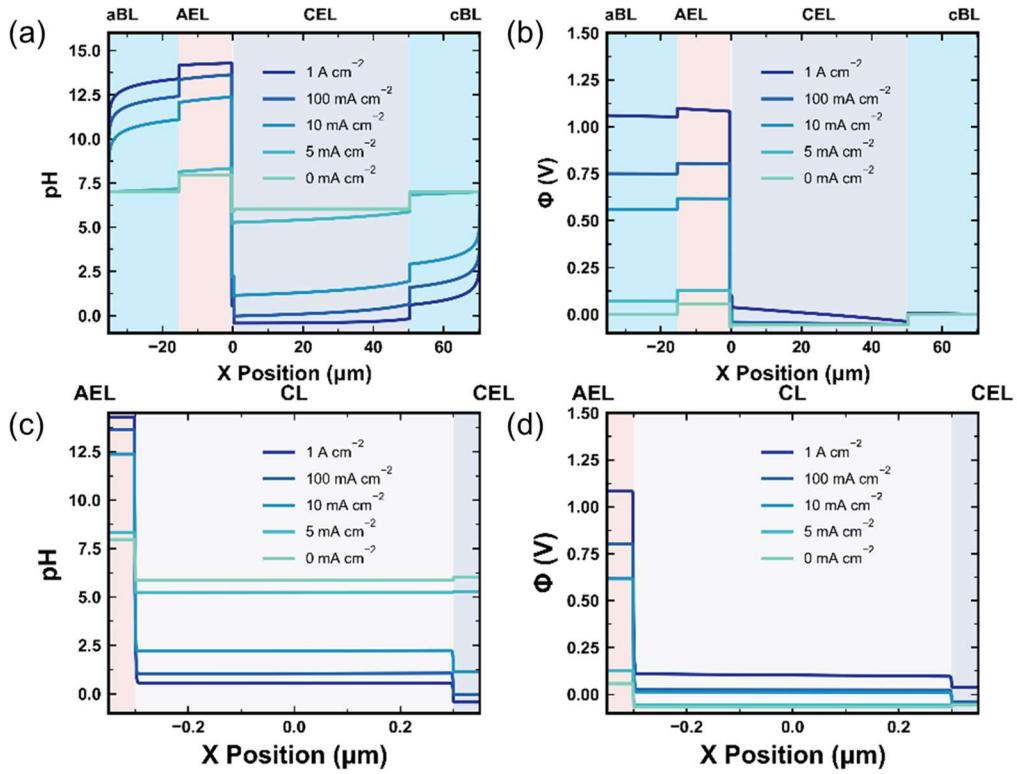

Figure S2.20 Full (a-b) and zoomed in (c-d) profiles of (a, c) local pH and (b, d) local electrostatic potential gradient zoomed into the catalyst layer domain.

To determine the salt crossover current, the contribution to the total current density from WD as measured by pH change was subtracted from the total current density. Because the H^+ and OH^- current density should be equivalent stoichiometrically, their average was used to perform the subtraction to determine the salt crossover current density.

$$j_{salt} = j_{total} - \frac{j_{H_3O^+,catholyte} + j_{OH^-,anolyte}}{2} \quad \text{(S1)}$$

2.5.8 Water Dissociation Catalysis Simulations

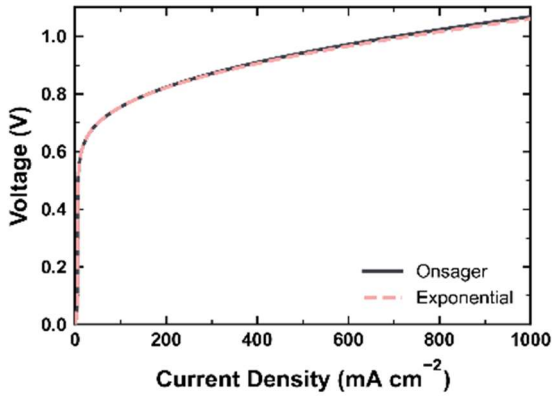

Figure S2.21 Simulated BPM polarization curve using Onsager kinetics (solid grey line) and exponential kinetics (dashed red line).

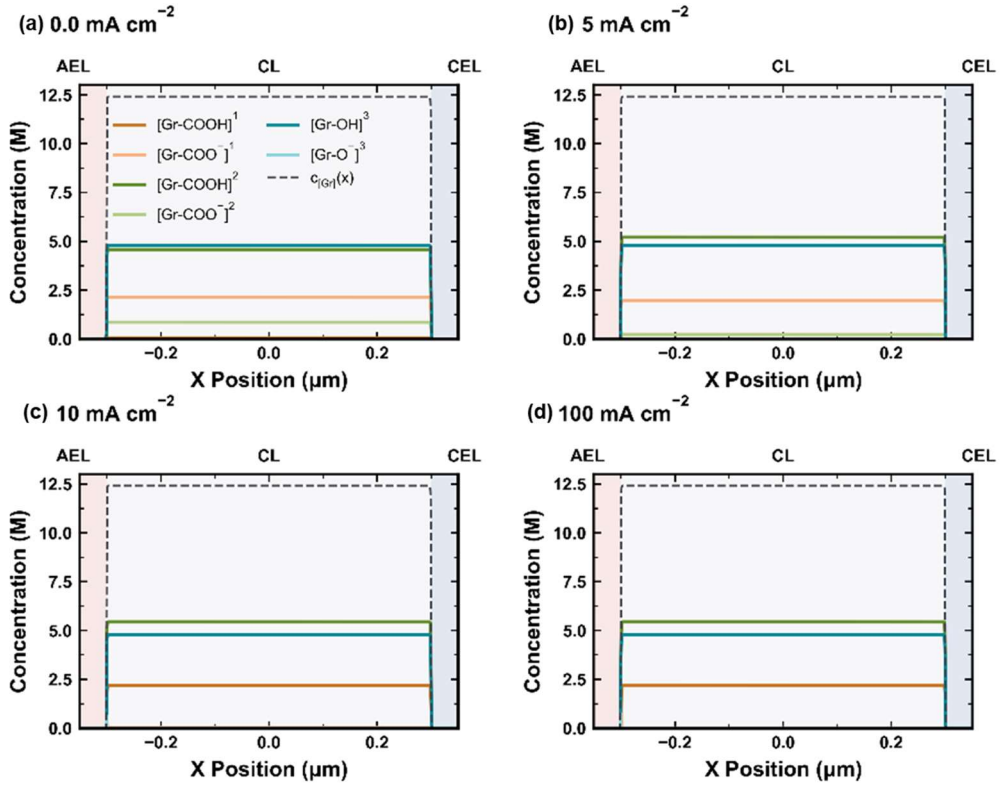

Figure S2.22 Simulated concentration profiles for various graphene oxide species within the BPM CL at (a) 0 mA cm^{-2}, (b) 5 mA cm^{-2}, (c) 10 mA cm^{-2}, and (d) 100 mA cm^{-2}. Solid lines represent concentrations of various GrOx sites. Dashed grey lines represent concentration of total sites present within the BPM CL.

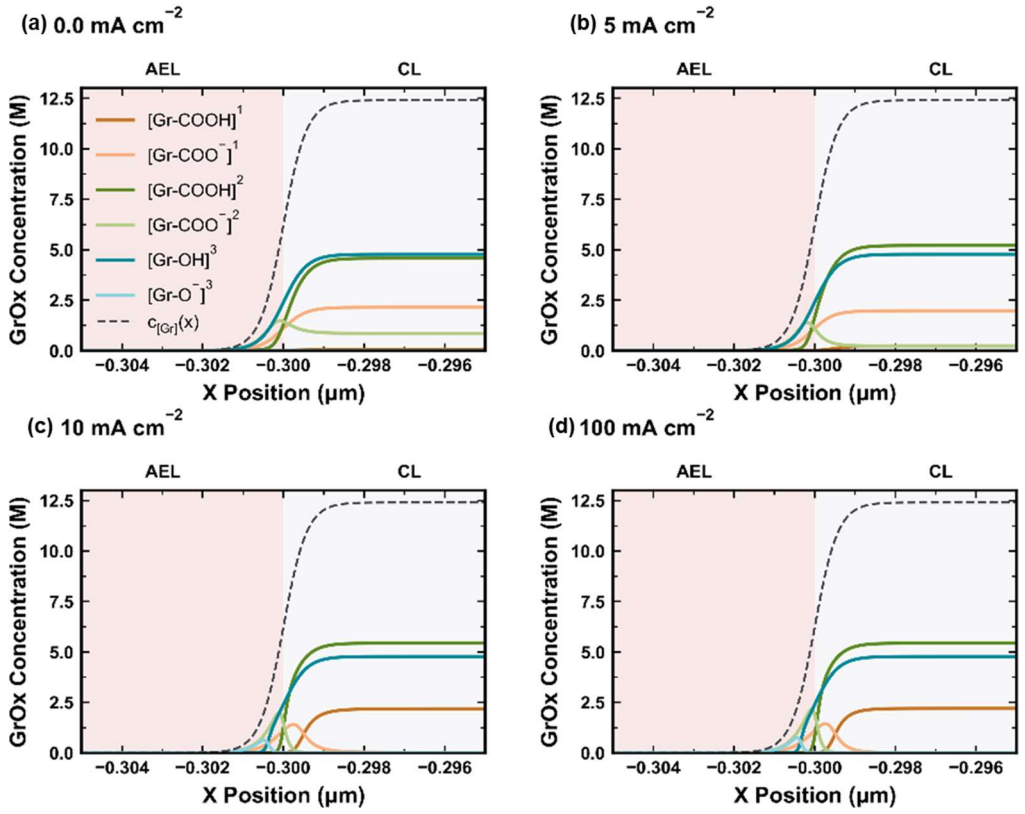

Figure S2.23 Simulated concentration profiles for various graphene oxide species at the AEL|CL interface at (a) 0 mA cm^{-2}, (b) 5 mA cm^{-2}, (c) 10 mA cm^{-2}, and (d) 100 mA cm^{-2}. Solid lines represent concentrations of various GrOx sites. Dashed grey lines represent concentration of total sites present within the BPM CL.

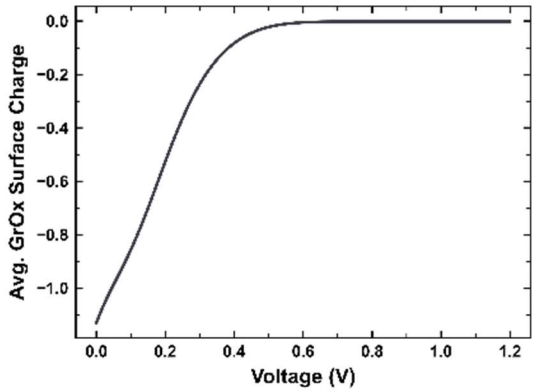

Figure S2.24 Average GrOx surface charge within the BPM CL as a function of applied voltage.

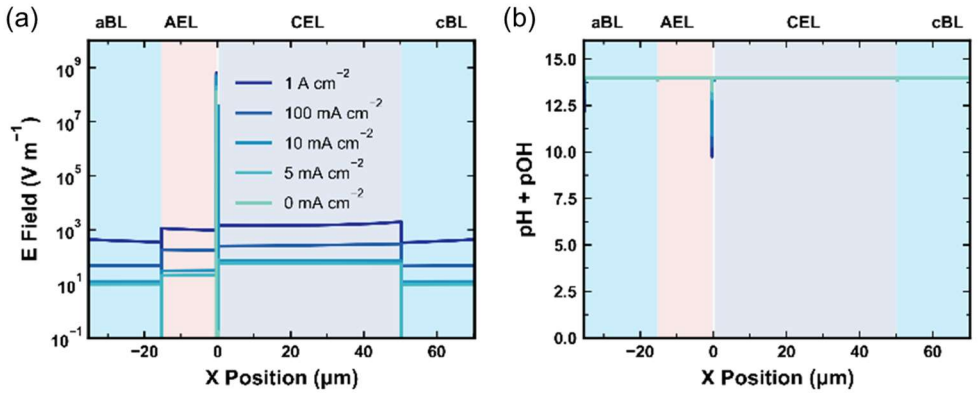

Figure S2.25 Simulated profiles of (a) local electric field and (b) pH + pOH throughout the BPM domain.

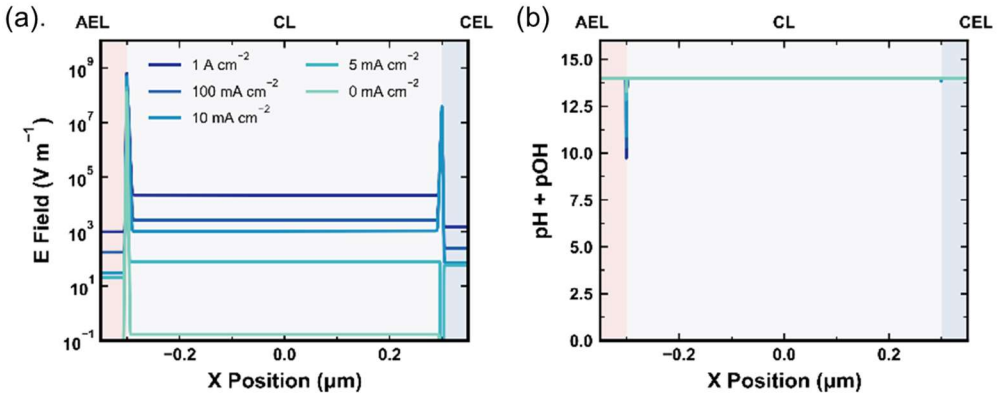

Figure S2.26 Simulated profiles of (a) local electric field and (b) pH + pOH zoomed into the catalyst layer domain.

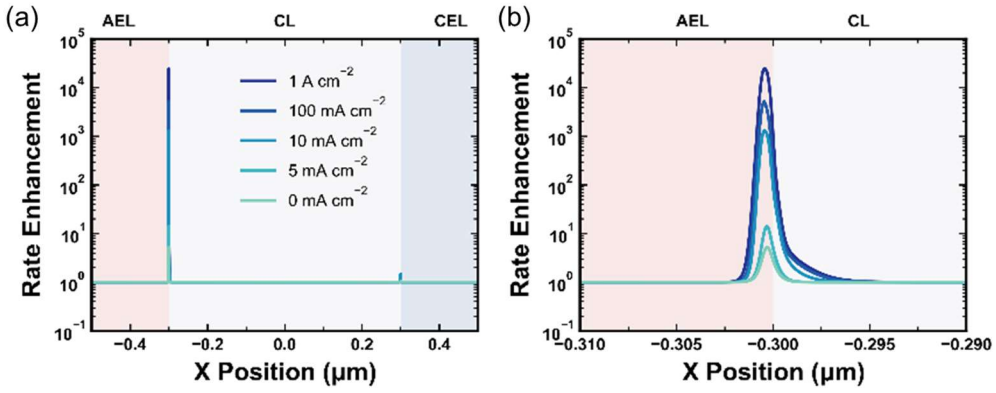

Figure S2.27 Simulated rate enhancement $\left(\frac{k_f(E)}{k_r(E)}\right)$ as a function of position within the BPM CL. (a) Simulated rate enhancement as a function of current density within the BPM CL domain. (b) Rate enhancement as a function of current density at the AEL|CL interface.

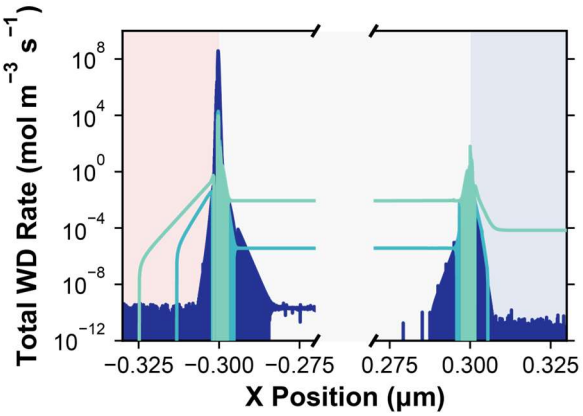

Figure S2.28 Simulated total WD contribution terms for proton and hydroxide generation within the BPM CL as a function of applied current density.

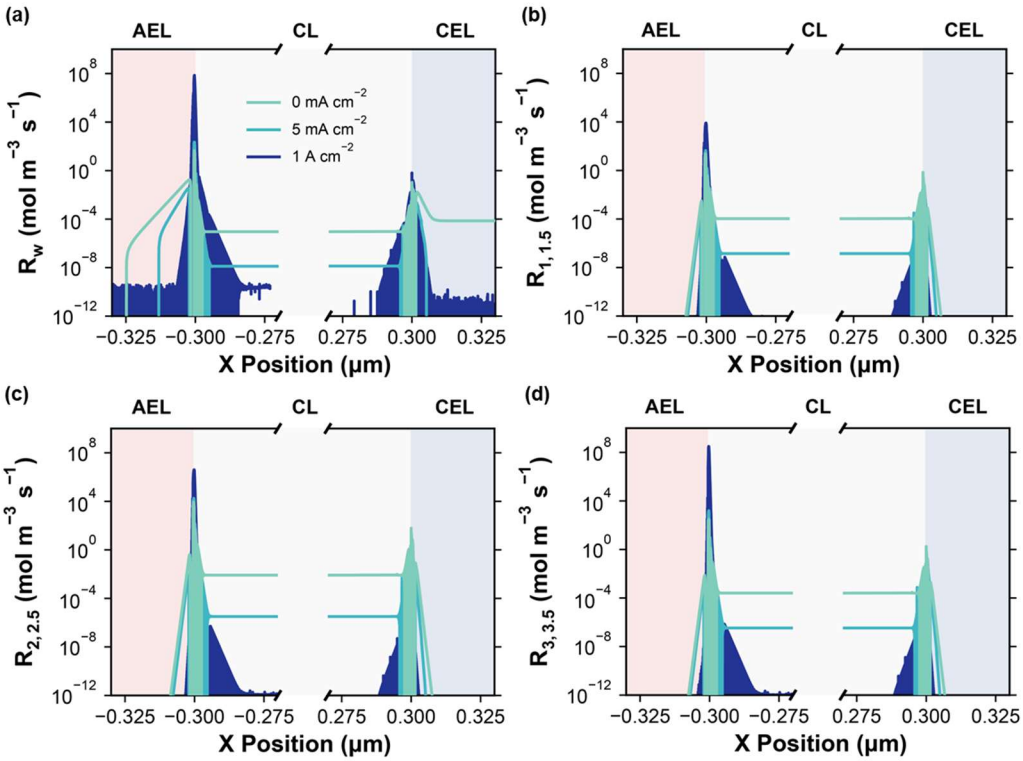

Figure S2.29 Simulated WD contribution terms for proton and hydroxide generation within the BPM CL as a function of applied current density. (a) Local rate of intrinsic WD. (b-d) Local rates of catalyzed WD by (b) site 1, (c) site 2, and (d) site 3.

2.5.9 Sensitivity to Catalyst Layer Properties

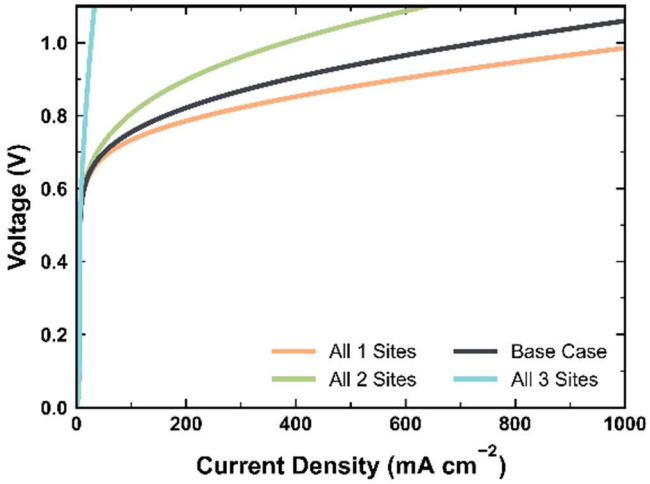

Figure S2.30 Simulated BPM polarization curves for a BPM containing only 1 site (orange line), 2 sites (green line), or 3 sites (blue line), compared to that of the base case (grey line) that contains $\frac{3}{16.9}$ site 1, $\frac{7.4}{16.9}$ site 2, and $\frac{6.5}{16.9}$ site 3.

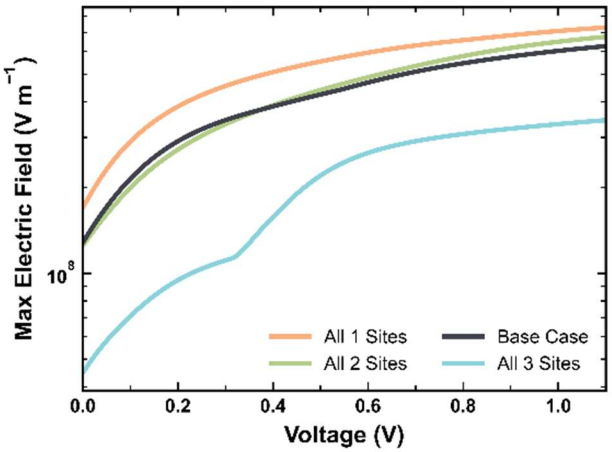

Figure S2.31 Simulated electric field maximum for a BPM containing only 1 sites (orange line), 2 sites (green line), or 3 sites (blue line), compared to that of the base case (grey line) that contains $\frac{3}{16.9}$ site 1, $\frac{7.4}{16.9}$ site 2, and $\frac{6.5}{16.9}$ site 3.

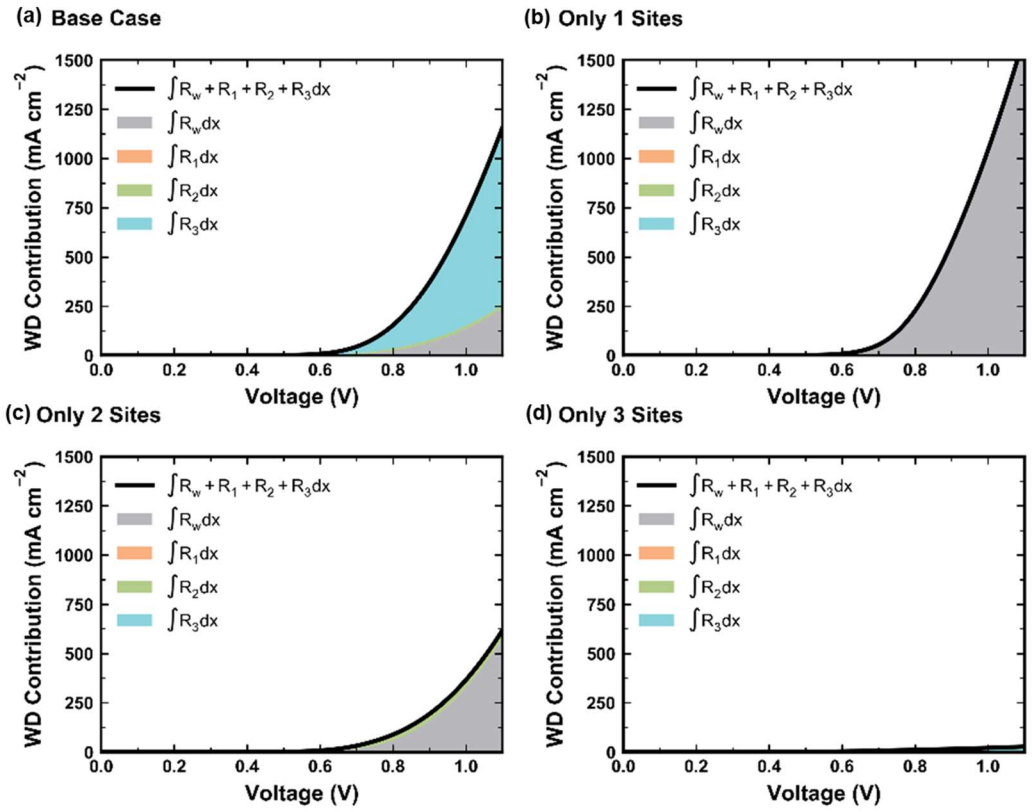

Figure S2.32 Breakdown of WD current density integrated within the CL for a BPM containing only (b) 1 sites, (c) 2 sites (green line), or (d) 3 sites (blue line), compared to that of the (a) base case (grey line) that contains $\frac{3}{16.9}$ site 1, $\frac{7.4}{16.9}$ site 2, and $\frac{6.5}{16.9}$ site 3. Orange area represents contribution to WD by R_1. Green area represents contribution to WD by R_2. Blue area represents contribution to WD by R_3. Grey area represents contribution to WD by intrinsic WD pathway.

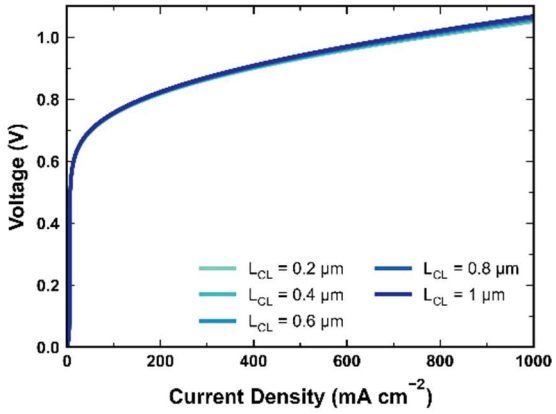

Figure S2.33 Sensitivity of BPM polarization curve to WD CL thickness.

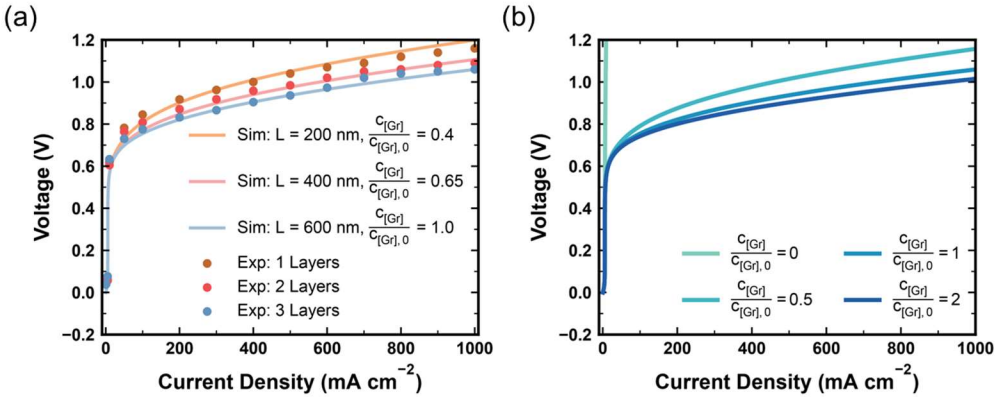

Figure S2.34 Sensitivity of BPM polarization curve to GrOx site concentration at (a) varied CL thickness consistent with experiment, and (b) constant thickness of 600 nm.

Chapter 3: BPM Characterization with In-Situ Confocal Microscopy and pH Sensitive Fluorescent Dye

3.1 Introduction

There remains much to elucidate and validate with experimental evidence about the internal structure of BPMs as well as reactions that occur within and around an operational BPM.[1,9] This chapter presents preliminary work aimed at visualizing and measuring pH in and around an operational BPM. To accomplish this goal, a confocal microscope was employed to emission from pH sensitive fluorescent dyes soaked into the BPM.

A confocal microscope allows for 3D visualization of fluorescent samples by detecting emitted wavelengths passed through a pinhole (**Figure 3.1a**).[104–106] The pinhole prevents scattered light from reaching the detector, enabling the microscope to produce clear and focused images in three dimensions in transparent samples.[104–106] Since the HCD-BPM is transparent (other than the catalyst layer) this technique was employed to visualize membrane structure and pH, utilizing a custom cell designed to accommodate a water immersion microscope objective (**Figure 3.1b**). In this chapter, initial visualization (using reflectance mode) of the inner structure of the HCD-BPM is presented. Furthermore, images are presented of fluorescence from pH sensitive dyes added to the electrolyte and membranes, allowing for direct visualization of the pH in an HCD-BPM with and without applied current.

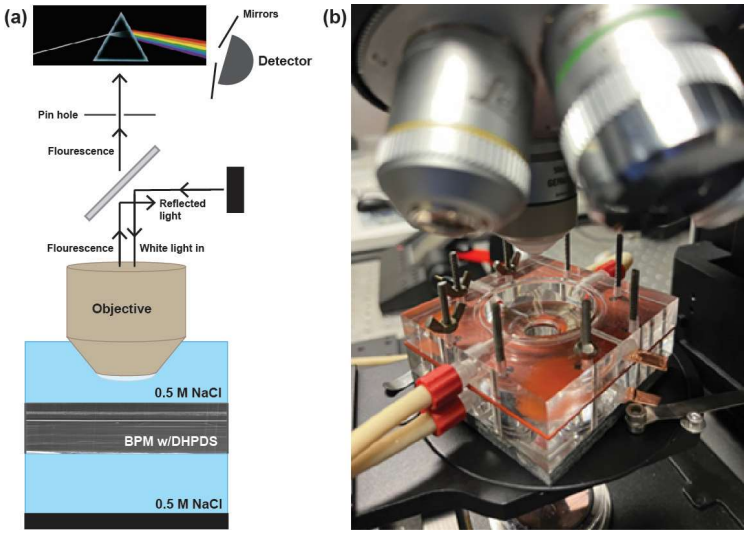

Figure 3.1 In-situ confocal microscopy. Diagram depicting the basics of confocal microscopy for imaging a BPM in solution with a water immersion lens (a). Images of assembled BPM-ED flow cell for in-situ confocal microscopy and monitoring of local pH (b).

3.2 Results, Discussion, and Outlook

For these experiments, APTS (8-Aminopyrene-1,3,6-Trisulfonic Acid, Trisodium Salt) dye was selected because it is sensitive between pH 11.5 and 13.5, a range that is relevant to the pH in an AEL as well as its alkaline solution counterpart.[106] Before implementing these dyes for measurements with the HCD-BPM, emission vs. pH calibration was performed. First, a set of solutions with pH values across the expected sensitivity range for APTS were made and an equal concentration of the dye was added to each solution (**Figure 3.2a**). A single set of microscope parameters, with two channels using the same excitation wavelength and detecting different emission wavelength ranges, was then applied to all samples, and resulting emission was measured (**Figure 3.2b**). Finally, the ratio of emission between the two channels was calculated for each sample and plotted against the

sample pH (**Figure 3.2c**). This use of a ratio of emission allows for accurate measurement of pH without dependence on pH concentration in future experiments.

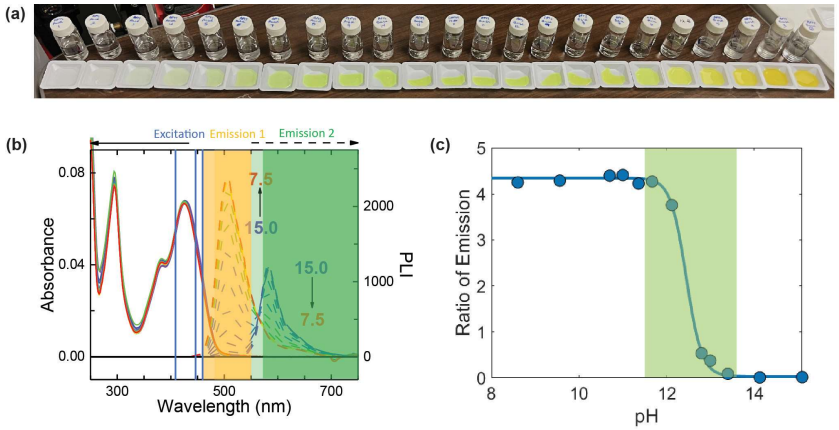

Figure 3.2 Calibration of APTS dye for monitoring pH in BPM-ED in-situ cell. Image of varying pH samples made for calibration (a). Absorbance spectrum for APTS dye with chosen excitation lase wavelengths and fluorescence detection ranges (b). Calibration curve for ratio of emission vs. pH for APTS dye (c).

The calibrated APTS dye was diluted and added to the electrolyte flowing through the custom BPM-ED confocal compatible cell. Initial cross section images of dye fluorescence, obtained from z-stacks, allowed for clear visualization of the AEL and CEL were compared to the surrounding electrolyte (**Figure 3.3**). Dye saturation, however, was too great in the AEL to clearly visualize details in the BPM cross section structure. One interesting element that was observed though, was the presence of defect channels through the AEL as seen in the cross section in **Figure 3.3**. This is the first time that defects like these have been directly observed in an ion exchange membrane. Inhomogeneous regions of concentrated polymer without fixed charge functional groups are the most likely explanation behind these regions that appear to have minimal dye saturation. Further experiments should be done to

determine if these defects are observed in other types of ion exchange membranes and to quantify the volume percent of the defects.

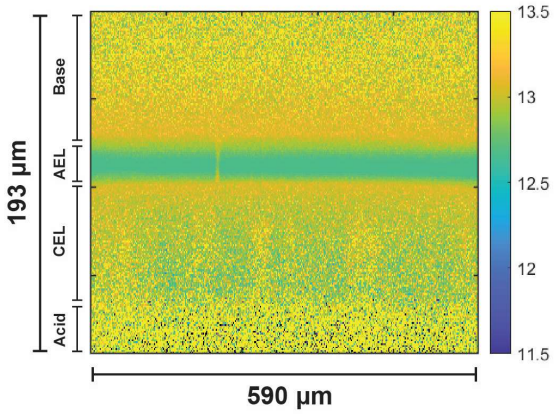

Figure 3.3 Cross section of pH through an HCD-BPM (Nafion 115 + PiperION A40) as visualized using APTS fluorescent dye Confocal microscopy z-stack data. Blue/green seen in the AEL is likely not reporting a true pH value as oversaturation of fluorescence signal occurred in this region.

BPM structure and defects were further visualized using reflectance mode in the confocal microscope. For these measurements, a wavelength of 600 nm (which gave the highest response signal) was set for both emission and detection. Z-stack images created with this method also showed the voids through the AEL seen when using the APTS dye. Furthermore, the use of reflectance mode allowed for visualization of the catalyst layer in the BPM junction (**Figure 3.4**), illuminating the structure and coverage for different loading amounts of GrOx (**Figure 3.5**).

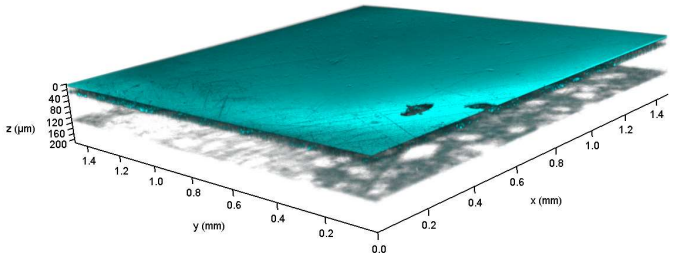

Figure 3.4 Z-stack composed 3D visualization using reflectance mode in a confocal microscope for a BPM made with Nafion 115, GrOx catalyst layer, and PiperION A40.

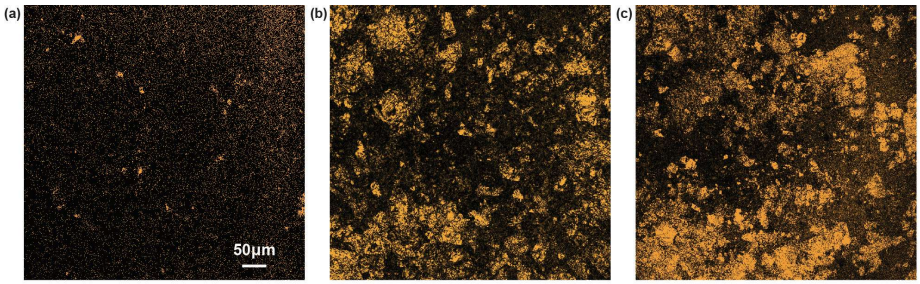

Figure 3.5 Confocal images taken in reflectance mode of the catalyst layer of HCD-BPMs with 1 (a), 3 (b), and 5 (c) spin coated layers of GrOx catalyst.

Reflectance mode was also used to visualize regions of delamination between the CEL and AEL in HCD-BPMs (**Figure 3.6**). It was observed that small pockets of delamination, as visualized in Figure 3.6, formed around areas of aggregated GrOx. This delamination due to GrOx aggregates likely contributes to the poorer performance seen in Chapter 2 for BPMs with larger amounts of catalyst loading. Further experiments should also be conducted to quantify the percent of area that is delaminated in HCD-BPMs with varying GrOx loading.

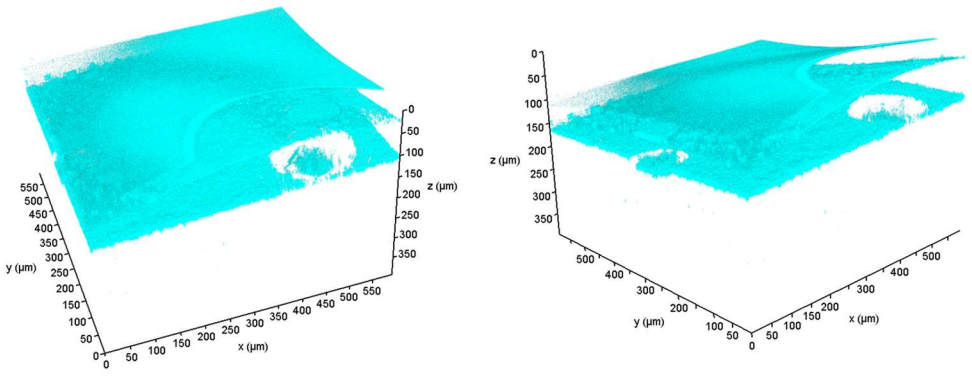

Figure 3.6 3D visualization (from two angles) of delamination between the CEL and AEL of a BPM made with Nafion 115, GrOx catalyst layer, and PiperION A40. The images were obtained by collecting a z-stack in reflectance mode in a confocal microscope.

Initial in-situ experiments were also performed to examine the change in pH with applied current in the BPM structure (**Figure 3.7 and 3.8**). Measurements performed in the electrolyte above the AEL allowed for the first ever visualization of pH regions, on the order of hundreds of microns, forming and mixing as current is applied (**Figure 3.7**). pH shifts can also be seen in BPM cross section images (**Figure 3.8**) obtained using the same technique. However, direct monitoring of pH in the BPM layers proved challenging because, not only was the AEL over saturated with dye, but the BPM also shifted when current was applied. Future cell design modifications should be considered, such as the use of supportive meshes above and below the BPM, to allow for further insightful imaging of pH in BPMS.

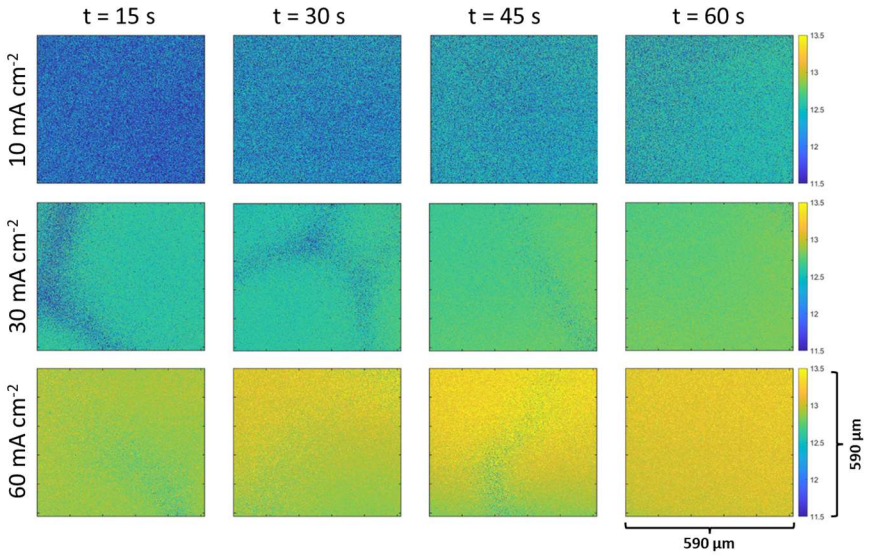

Figure 3.7 In-situ confocal microscopy images of electrolyte ~100 um above the surface of the AEL of an HCD-BPM (Nafion 115 + PiperION A40). Each image is ~20 sec apart starting in the top left corner and progressing left to right and top to bottom. The first, second, and third rows corresponds to applied currents of 12, 30, and 60 mA cm^{-2}, respectively. Each image corresponds to an area with a length of 590 µm and a width of 590 µm.

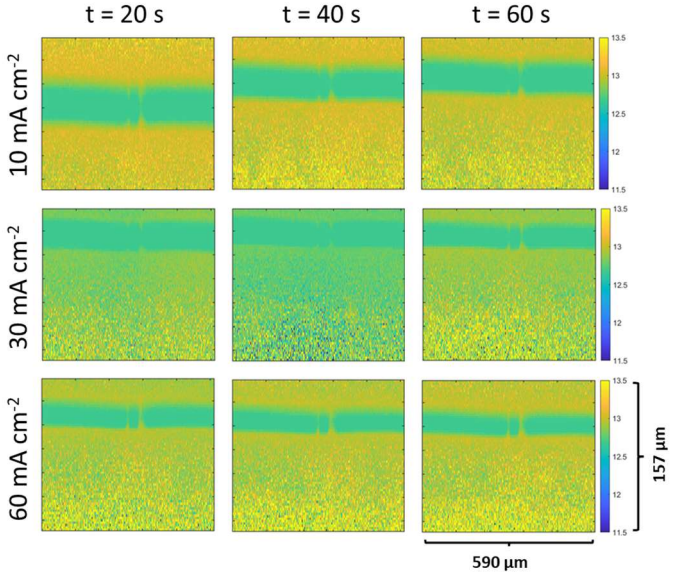

Figure 3.8 In-situ confocal microscopy images of HCD-BPM (Nafion 115 + PiperION A40) cross section, constructed from z-stack data. Each image is ~10 sec apart starting in the top left corner and progressing left to right and top to bottom. The first, second, and third rows corresponds to applied currents of 12, 30, and 60 mA cm^{-2}, respectively. Each image corresponds to an area with a heigh of 157 µm and a width of 590 µm.

3.4 Materials and Methods

Materials: Nafion 115 (127 μm, Fuel Cell Store), PiperION A40 (40 μm, Versogen), graphene oxide paste (Graphene Supermarket), Sodium Sulfate (Na_2SO_4), 8-Aminopyrene-1,3,6-Trisulfonic Acid, Trisodium Salt (APTS, Thermo Fisher). All membranes were received in dry form, pretreated according to manufacturer's instructions before use, and stored in DI water (CEMs) or 1 M NaOH (AEMs). All chemicals were used as received.

Catalyst ink: Catalyst inks were made by first diluting graphene oxide paste (Graphene Supermarket) from 30 g/L to 10 g/L. The dilute graphene oxide dispersion was then mixed with Nafion D520 in a 1:1 volume ratio. The final ink solution was sonicated for at least 10 minutes prior to use.

BPM fabrication: First, a piece of purchased Nafion membrane (NR212, NR211, NR115), precut into a 3x3 cm square and soaked in DI water for at least 1 h, was placed on a glass slide and patted dry with a Kim wipe. The membrane with then taped to the glass slide on all 4 sides with Kapton tape. GrOx catalyst ink was then spin coated onto the Nafion membrane at 3000 rpm for 30 s. Next, the Nafion membrane with GrOx was placed in an oven at 100°C for 2 min. This process of spin coating and heating was repeated if more layers, i.e., greater mass loading, was desired. Finally, the Nafion membrane with GrOx was rewetted with a few drops of DI water, sandwiched with the desired thickness of PiperION membrane, and pressed firmly between gloved fingers, taking care to press out any air pockets. All membranes were tested directly after assembly.

Dye calibration: First, a set of solutions with pH values across the expected sensitivity range for APTS were made by diluting 1 M KOH and 1 M HCl and an

equal concentration of the dye was added to each solution (**Figure 3.2a**). A single set of microscope parameters, with two channels using the same excitation wavelength and detecting different emission wavelength ranges, was then applied to all samples, and resulting emission was measured (**Figure 3.2b**). Finally, the ratio of emission between the two channels was calculated for each sample and plotted against the sample pH (**Figure 3.2c**).

Electrodialysis cell design/assembly: Figure 3.1 shows an image of the electrodialysis cell used for testing and visualizing the BPMs in this work. The cell was designed using SolidWorks and parts were ordered from Xometry. There are two main pieces in the cell stack. The bottom layer has in flow and out flow ports for electrolyte, a port for a working electrode, and a port for a reference electrode (Leakless Ag/AgCl). The top layer contains the same four ports as the bottom, and has a large opening in the top, which allows use of the confocal water immersion objective. When assembling the cell for measurements, a BPM is sandwiched between the two layers, sealed with an O-ring and a gasket. The inlet and outlet tubing is then connected to a peristaltic pump and 1 M Na_2SO_4 is flowed through both chambers until they are full. The pump is then stopped to avoid noise from vibrations when collecting images. The water immersion objective is then lowered into the solution in the top chamber to start measurements.

Reflectance Measurements: Leica confocal software is used to set an excitation and detection wavelength of 600nm. The laser is turned on and the microscope stage is shifted in z until reflectance from the sample is observed. A z-stack measurement is then set up for which the starting point is just above the BPM and its ending point is

just below the BPM. The desired zoom, pixel size, and z-step length are then set, and the measurement is then started. Individual x-y images are reported as seen in the microscope. The 3D viewing function in the software is used to obtain all 3D images.

Measurements with dye: For measurements with fluorescent dye, the two-channel emission and detection settings chosen during the dye calibration are used for all measurements. MATLAB is then used along with the fit curve from the calibration to create pH maps from the images collected in the confocal. MATLAB is also used to stitch together images from z-stack measurements and form x-z images for visualizing the cross section of the BPMs.

Chronopotentiometry: Chronopotentiometry using a Biologic SP 200 was used to apply current steps for in-situ measurements.

Chapter 4: Bipolar Membrane Scaling and Implementation into Electrodialysis Stack

Content drawn from: Éowyn Lucas, Justin C. Bui, Monica Hwang, Kaiwen Wang, Alexis T. Bell, Adam Z. Weber, Shane Ardo, Harry A. Atwater, and Chengxiang Xiang. Asymmetric Bipolar Membrane for High Current Density Electrodialysis Operation with Exceptional Stability. Nature Energy. In Review. Submitted February 7, 2023.

4.1 Introduction

As previously discussed, BPM-ED is a promising method for DAC and DOC.[53,107] This chapter explores scaling of the HCD-BPM and implementation into a custom electrodialysis thin cell stack to evaluate its potential for implementation into industrial systems. Due to the high capital cost of ion exchange membranes and cell parts, large area BPMs (~ 0.5 – 1 m^2) are employed in commercial systems to avoid excess material waste.[10,25–27,50] Furthermore, to drive a current and maintain electroneutrality, BPM-ED systems must contend with the energy penalty of a redox reaction (typically water electrolysis) across the anode and cathode of the device.[54] To limit the contribution of the redox reaction to the total power needed to run the system, BPM-ED stacks are designed with multiple acid/base flow channel cells (typically > 100 for commercial systems) sandwiched between the outer anode and cathode. This design means that, when divided across all cells in a stack, the energy penalty from the redox reaction is negligible. These multi cell stacks are also engineered to minimize the thickness of each flow chamber and reduce solution resistance losses, which can add up quickly across the full cell. All multi-cell stack experiments presented in this chapter were performed in a custom BPM-ED system (**Figure 4.1**) designed in house by Monica Hwang (Staff Scientist, Caltech).

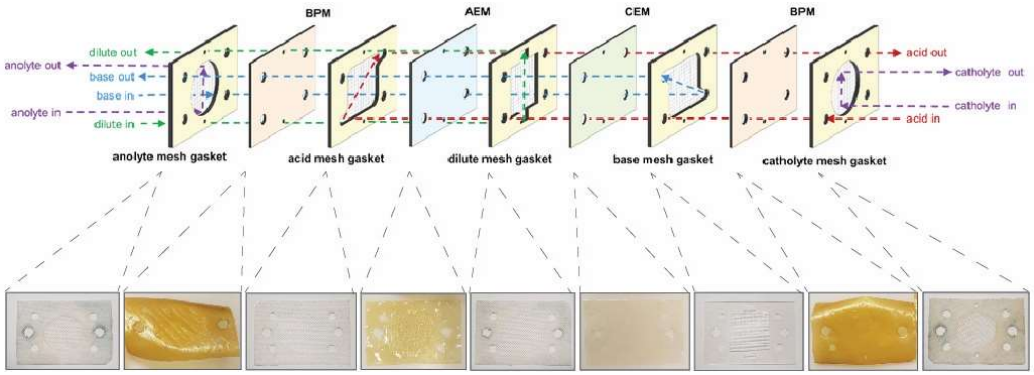

Figure 4.1 Diagram of layers and flow channels in BPM-ED 1-cell stack (top) with images of each membrane and gasket layer (bottom).

To show that the HCD-BPM is functional beyond an active area of 1 cm^2 previously presented, the BPM was scaled to have an active area of 6 cm^2 (with the full size of the BPM = 35 cm^2, indicating that further scaling is possible) and tested in the thin electrodialysis cell stack. The same fabrication methods used to make the small area BPMs were successfully employed for the scaled membranes. When the HCD-BPM was tested in the custom cell stack system, cell voltages were achieved that were significantly lower than with a commercial Fumasep BPM and similar to those obtained with a commercial Iontech BPM. Furthermore, the HCD-BPM demonstrated stable operation in the cell stack for > 15 hours at 500 mA cm^{-2}.

4.2 Results and Discussion

First, the cell configuration and components will be described as they vary some across experiments, which plays an important role in the observed results. Details on the CEMs, AEMs, BPMs, and gaskets used for experiments presented in this chapter are given in **Table 4.1**. The specific membranes used as well as the

conductivity and voltage contributions for the dilute, acid, and base flow channels is stated later in the text as relevant for each experiment.

Table 4.1 BPM-ED cell stack components.

Component	Thickness (nm)	Conductivity (mS cm^{-1})	Voltage contribution (V) @ 500 mA cm^{-2}
Fumasep FAB-PK-130 (AEM)	126.2	1.19	5.30
Aemion AF2 (AEM)	95	5.50	0.88
PiperION A40 (AEM)	64	10.5	0.305
Fumasep FKB-PK-130 (CEM)	130.4	1.22	5.34
Nafion NR212 (CEM)	57	23.7	0.12
Fumasep (BPM)	-	-	2.18
Iontech (BPM)	-	-	1.40
HCD-BPM	-	-	-
Gasket (Dilute)	450	-	-
Gasket (Acid)	450	-	-
Gasket (Base)	450	-	-

For the thin cell stack used in this work, the voltage is measured across the entire stack as opposed to what is reported in **Chapter 2** where the voltage is measured across reference electrodes in Luggin capillaries placed on either side of the BPM. Therefore, to report the voltage of a single cell, without the redox reaction voltage loss, a 0-cell measurement is taken for each BPM. A zero-cell stack consists of a single BPM with two electrolyte outer chambers. A 1-cell, 2-cell, 3-cell, etc. stack then comprises a grouping of membranes (AEM/CEM/BPM or AEM/CEM) repeated the appropriate number of times following zero-cell stack BPM (**Figure 4.2**). To report the voltage of a single cell (excluding the redox reactions and edge BPM) with a specific BPM implemented, polarization data is collected for both a 0-cell and a 1-cell stack configuration with the same type of BPM and the 0-cell voltage is subtracted from the full 1-cell stack voltage. The result is reported at the experimental 1-cell voltage.

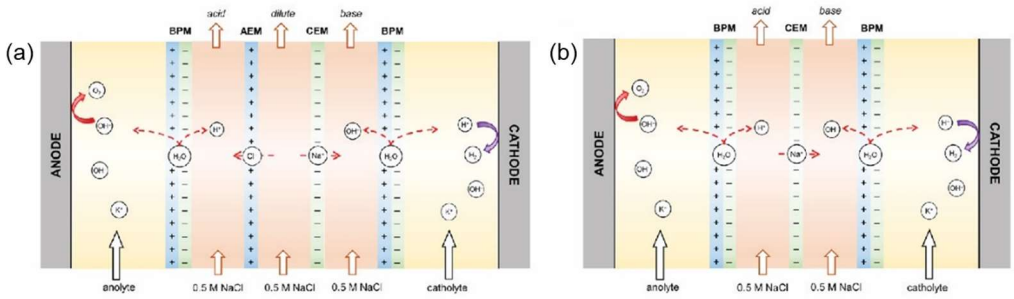

Figure 4.2 Cross section diagrams of BPM-ED cell configuration, flow, reactions, and ion transport for BPM-AEM-CEM assembly (a) and BPM-CEM assembly (b).

Once the cell stacks described above are assembled, they are compressed between two electrodes using the device pictured in **Figure 4.3**. Proper alignment of the layers and compression of the stack is critical to prevent leakage, which can lead to unaccounted for voltage losses.

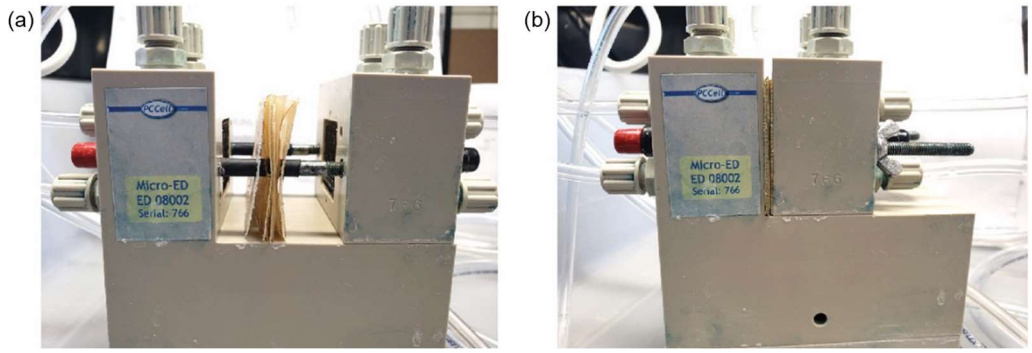

Figure 4.3 Images of cell stack assembly uncompressed (a) and compressed (b).

Multiple different 6 cm^2 active area HCD-BPMs with varying CEL and AEL thickness and fabrication methodology were made and tested to determine the most stable for scaled stack operation (**Figure 4.4, 4.5** and **Table 4.2**).

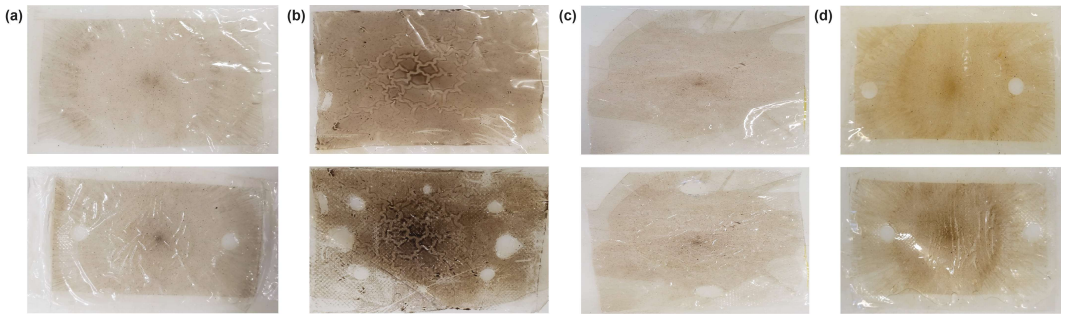

Figure 4.4 Images of multiple generations of scaled GrOx BPMs before and after testing in BPM-ED cell stack. (a) BPM1, (b) BPM2, (c) BPM3, (d) BPM4.

Table 4.2 CEL, AEL, and catalyst layer for BPMs 1-4.

Sample	CEL	AEL	Catalyst Layer
BPM1	Nafion NR212	PiperION 15R	3 layers spin coated GrOx, 3000 rpm, 30 sec, heated at 100°C for 2 min
BPM2	Nafion NR212	PiperION 15R	1 layer spin coated GrOx, 500 rpm, 30 sec, heated at 100°C for 50 min
BPM3	Nafion NR212	PiperION 15R	3 layers spin coated GrOx, 3000 rpm, 30 sec, heated at 100°C for 30 min
BPM4	Nafion N115	PiperION A40	3 layers spin coated GrOx, 3000 rpm, 30 sec, heated at 100°C for 30 min

The initial set of BPMs (BPM1) were fabricated identically to the best performing 1 cm^2 active area BPMs. Although these BPMs operated successfully in the ED cell stack, voltage was not stable at high currents and wrinkling of the AEL was observed after removal from the cell. Furthermore, it appeared that some of the GrOx catalyst layer was washed away during operation. To prevent the loss of catalyst material, new membranes (BPM2) were made with a slower spin rate for catalyst deposition and a longer heat treatment to adhere the catalyst to the Nafion.

The slow spin coating rate, however, led to wetting and wrinkling of the Nafion causing and inhomogeneous coating of GrOx. Nevertheless, when tested in the cell stack, BPM2 demonstrated some of the lowest voltages out of all configurations tested. BPM3 was an attempt to recreate the successful GrOx adhesion through heat treatment observed for BPM2, without wrinkling of the Nafion on the prosses by keeping the same heating time and returning to the initial faster spin coating rate. This third set performed similarly to BPM2; however, wrinkling was still seen in the AEL after removal from the cell. To overcome the wrinkling of the AEL and generally improve mechanical stability, BPM4 was made with a thicker AEL and CEL layer. The performance of BPM4 remained close to that of BPM2 and BPM3, indicating that any increase in resistance due to the implementation of thicker membrane layers was negligible in the stack.

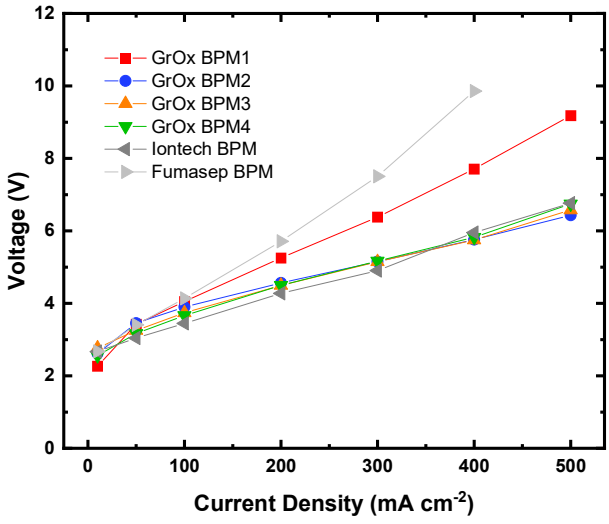

Figure 4.5 0-cell polarization curves for commercial Iontech and Fumasep BPMs compared to novel GrOx BPM tested in electrodialysis cell stack.

When 0-cell and 1-cell measurements were completed and the experimental single cell voltage was calculated, a significant gap was observed when compared to

calculated voltage contributions (**Figure 4.6)**. It was hypothesized that the thin nature of the HCD-BPM made it challenging to fully compress the cell stack leading to leakage between the chambers and unaccounted for voltage losses. One method that was employed to eliminate these voltage losses was to use a thicker CEM and AEM for chamber separation.

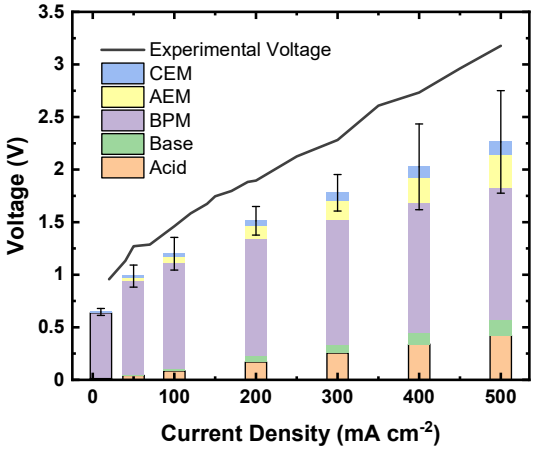

Figure 4.6 Experimental voltage and calculated voltage contributions for one of the top performing HCD-BPMs.

When implemented, thicker CEM and AEM layers did in fact allow for matching of the experimental and measured voltages (**Figure 4.7**). The taller stacked bars in **Figure 4.7b** show the calculated voltage values for each layer's contributions. The grey error bars show the standard deviation for the AEM and CEM voltage contribution and the black error bars show the total standard deviation for the AEM and CEM voltage. All other voltage contributions did not have significant error. It can be seen in **Figure 4.7b** that the total calculated voltage contributions closely match the experimental one-cell voltage for the 6 cm^2 active area GrOx catalyzed, asymmetric BPM.

With optimization of the electrodialysis stack design to allow for increased compression, thin AEM and CEM layers can be implemented again. The shorter bars in **Figure 4.7b** show the voltage contribution of each layer of a one-cell stack based on the conductivities of thinner AEMs, CEMs, and gaskets. With this improved system, the total cell voltage at 500 mA cm^{-2} would be dropped from ~ 14 to < 4 V.

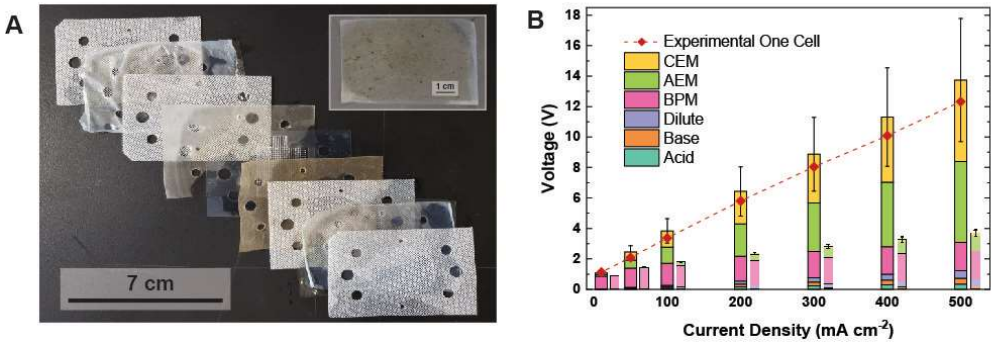

Figure 4.7 6 cm^2 active area thin AEL BPM tested in single cell electrodialysis stack. (a) Photo of actual layers of electrodialysis cell stack. (b) Experimental one-cell polarization curve for multi-cell stack with GrOx catalyzed, asymmetric BPM (dashed line), calculated voltages for each section of the one-cell stack at current densities of 10 – 500 mA cm^{-2} (taller stacked bars), and calculated voltages for each section of a projected optimized one-cell.

Finally, stability data is presented for an HCD-BPM made identically to BPM3 presented above (**Figure 4.8**). These initial results show that the BPM was stable for >16 hours at 500 mA cm^2. Further stability measurements are still necessary however, to optimize the BPM for further scaling and commercial use.

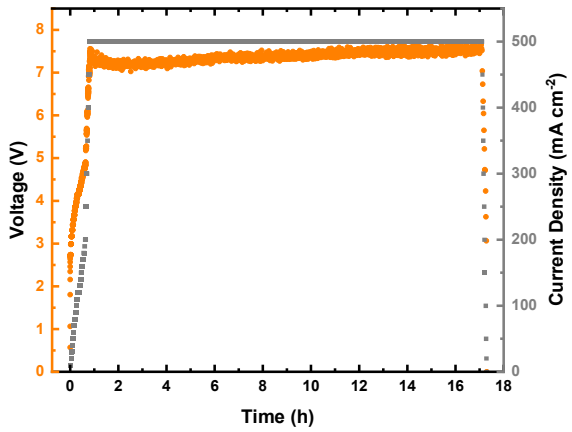

Figure 4.8 Stability of GrOx BPM in electrodialysis cell stack at 500 mA cm^{-2}.

4.3 Conclusion and Outlook

In this work scaling and testing of our novel BPM in a scaled cell stack was performed. The experiments showed an operational performance better than/comparable to commercial BPMs. More work still needs to be done, however, to understand the voltage gaps between measured and calculated seen for most experiments. Furthermore, improves adhesion of GrOx and overall adhesion at junction of BPM as well as development of a new catalyst deposition method will be necessary to scale beyond 6 cm^2.

4.4 Materials and Methods

Materials: As described in **Chapter 2**.

Membrane preparation: As described in **Chapter 2**.

BPM fabrication: As described in **Chapter 2**.

Scaled cell stack: A commercial cell with iridium oxide-mixed metal oxide electrodes and a 6 cm^2 active area (ED 08002-010-1031-EDR, PCCell GmbH) was

modified with two holes on the catholyte chamber to create inlet and outlet ports for the dilute chamber. For a single-cell stack, from anode to cathode, the membrane stack comprises of a BPM, AEM, CEM, and a BPM. All membranes were cut to a size of ~5 cm x 7 cm with a blade. 2 mm and 4 mm holes were punched in the appropriate locations to allow solution flow past the membranes for the acid and base chambers and dilute chamber, respectively. In between the membranes, a modified commercial polypropylene mesh silicone gasket (ED 08-115-085, 450 μm thickness, PCCell GmbH for the inner chambers and ED 08-115-086, 450 μm thickness, PCCell GmbH for the outer chambers) is used to allow continuous, segregated solution flow through the inner chambers (acid, base, and dilute) and outer chambers (anolyte and catholyte) of the cell. 1 M KOH solution was recirculated in two separate 5 L polypropylene reservoirs (3795T27, McMaster-Carr) for the anolyte and catholyte chambers at rate of ~1.5 L/min (BT601S-YT25, Golander Pump). 0.5 M NaCl solution flowed through the cell from separate source reservoirs for the acid, base, and dilute chambers and exited to a communal waste container at rates of ~35 mL/min (Masterflex L/S 7519-20, 2.79 mm ID tubing, Cole-Parmer) for the acid and base channels and ~45 mL/min (PWM-controlled motor pump, 4 mm ID tubing).

Small cell chronopotentiometry: As described in **Chapter 2**.

Faradaic efficiency: As described in **Chapter 2**

Scaled cell stack chronopotentiometry: After the electrodialysis cell described above was assembled, power supply (2260-B-80-13, 360 W, Keithley) leads were attached to the cell in a two-point configuration to apply current and measure voltage. A custom LabVIEW VI controlled the applied current and chronopotentiometry

measurements were used to obtain all reported current density and voltage data. For each point, a chosen current was applied across the anode and cathode and held steady for at least one minute or until the measured voltage reached steady state. Voltage data was collected at a time step of 5 s. The current was then increased to the next point and the process was continued until all desired current density measurements were obtained. The final reported voltage values are the averages of the voltage collected over a section of the steady state region for each chronopotentiometry step.

Stacked cell voltage contribution calculations: At each chosen current, under steady state, solution samples were collected in 50 mL polypropylene conical tubes from the acid, base, and dilute chambers. Once the samples were collected, the conductivity was measured using a four-ring conductivity probe (HI76312, Hanna Instruments) and meter (HI5521, Hanna Instruments). The voltage contributions for the inner chambers and ion-exchange membranes (AEM and CEM) were calculated using the following equation: $V = \frac{jL}{\sigma}$ where j is the current density (mA cm^{-2}), L is the width of the chamber (i.e., the thickness of the mesh gasket) or thickness of the membrane (cm), respectively, and K is the solution or membrane conductivity (mS cm^{-1}), respectively. The thickness of the membranes was determined using a micrometer (293-348-30, Mitutoyo). Errors in the membrane voltage contributions were determined using the standard errors in the conductivity and thickness measurements to calculate the minimum and maximum possible voltage contributions. The BPM voltage contribution was determined using this work's custom BPM testing cell as previously described.

Chapter 5: Bipolar Membrane Mediated Efficient Acid-Base Combination Yielding High Power Density

Content drawn from: Zishuai Bill Zhang, Éowyn Lucas, Harry A. Atwater, and Chengxiang Xiang. Bipolar Membrane Mediated Efficient Acid-Base Combination Yielding High Power Density.

5.1 Introduction

As electrical grids around the world increasingly rely on variable output renewable energy sources (wind, solar, etc.), it is imperative to develop and implement long-term, affordable grid energy storage that can account for fluctuations.[108] Batteries account for the largest growth in energy storage capacity over the last decade, however, most conventional batteries (e.g., Li-ion, lead-acid) have a limited cycling lifetime and depend on finite resource minerals and/or toxic chemicals.[109] Flow batteries on the other hand, a newly emerging technology, show great promise for grid level storage as they have long term cycling stability, are scalable, and require little capital overhead.[109] Within the realm of flow batteries, the acid-base flow battery, which employs bipolar membranes (BPMs) has shown initial promise as a scalable, low-cost and environmental friendly form of energy storage.

Bipolar membranes (BPMs), composed of a cation exchange layer (CEL) laminated with an anion exchange layer (AEL), have been extensively investigated in reverse bias for enhanced water dissociation (WD) to acid and base and implemented in numerous applications (e.g., acid and base recovery, wastewater treatment, water electrolysis, electrochemical CO_2 reduction, and carbon

removal).[1,110–114] BPMs, however, can also be operated in forward bias, where H^+ and OH^- recombine to form water at the junction between the CEL and AEL. When reverse and forward bias BPMs are combined sequentially, this system becomes an acid-base flow battery (**Figure 5.1a**). Energy is input to drive the reverse-bias reaction (**Equation 5.1**) and stored chemically as acid and base. The chemical energy can then be harnessed by allowing the BPM to run in forward bias, generating water at the junction (**Equation 5.2**).[18]

$$\textit{Water dissociation:} \quad H_2O \rightleftharpoons H^+ + OH^- \tag{5.1}$$

$$\textit{Acid-base recombination:} \quad H^+ + OH^- \rightleftharpoons H_2O \tag{5.2}$$

Minimal work has been published investigating BPMs in forward bias, leaving open vast opportunities for improving performance and understanding fundamentals of BPM architecture, electrocatalysts, water transport, and recombination. There are two key factors to consider when designing a forward bias BPM. The first is that the mass transport of ions becomes a limiting factor for high current density operation; an efficient forward-bias BPM must therefore enable sufficient ion transport without significant ion leakage. The second factor is that water formed at the BPM junction can quickly lead to delamination and failure, especially at high current densities when water influx exceeds efflux from the junction.[1] It is therefore critical to develop BPMs with CEL and/or AEL layers that allow for rapid water removal from the junction. To date, the most advanced research has demonstrated that free-standing commercial (i.e., Fumasep FBM-BPM) and novel BPMs can only operate in forward bias at current densities less than 100 mA cm^{-2}, resulting in a maximum power density of 50 mW cm^{-2} (**Figure**

5.1b). Efficient forward bias BPMs that can operate at a commercially relevant current density (e.g., j > 200 mA cm^{-2}) remains uncharted territory.

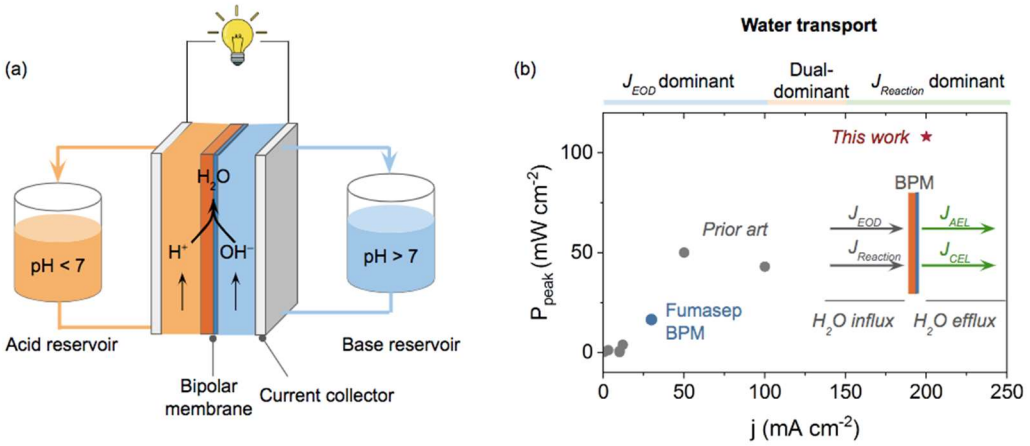

Figure 5.1 Demonstration of high-power density yield BPM. (a) Schematic of a BPM implemented in forward bias for high power density energy storage and (b) peak power vs. current density for the BPM presented in this work compared to prior work and commercial BPMs.[67,115–120] The insert is an illustration of H_2O influx driven by EOD and acid-base reaction, and efflux driven by osmosis.

In our previous work, we exhibited that BPMs made from laminated Nafion membranes as CELs and PiperION membranes as AELs with a graphene oxide (GrOx) catalyst layer led to record performance in reverse bias,[121] proving them to be effective for transporting ions and water at high current densities. These readily available membranes were leverages in this work to create forward bias BPMs with carefully designed layer thickness and lamination to modulate the ion and water transport and achieved sustainable operation at 200 mA cm^{-2} with a yield power density of 109 mW cm^{-2} (**Figure 5.1b**). While acid-base recombination is kinetically fast, this study shows the management of reaction sites and reactant concentrations using high-surface nanocarbons in the BPM junctions significantly

enhanced the reaction and improved the durability. Our BPMs display excellent stability over a 24-hour period at 50 mA cm^{-2}, with a voltage drop of only ~1.6%, whereas the commercial BPM failed after 10 minutes.

Water management is also critical for forward-bias BPMs, however, there is currently little information available to quantify water influx and efflux from a BPM junction. In this study, we set out to fill the gap in the literature with a rigorous investigation of water transport using isotopic labeling. For the first time, this research reveals that the water influx is primarily driven by electro-osmotic drag (EOD) at low current densities (j < 30 mA cm^{-2}), then becomes dual-dominant with acid-base recombination (100 – 150 mA cm^{-2}), and eventually acid-base recombination dominates water influx at high current densities (j > 150 mA cm^{-2}) (**Figure 5.1b**). Overall, this work addresses the gap in understanding of water transport mechanisms in a forward-bias BPM and presents a high current density, stable BPM with a viable path for long-term, affordable, grid-scale energy storage.

5.2 Results and discussion

A five-compartment electrodialysis cell was used to conduct all electrolysis experiments, which assessed the performance of BPMs in forward-bias.[45] This test cell consisted of, from left to right in the **Figure 5.2** schematic, anode/anolyte, product, acid, base and cathode/catholyte chambers . The anode and cathode electrodes were made from nickel (Ni) foil mediating the oxygen evolution reaction (OER) and hydrogen evolution reaction (HER), respectively, and 0.5 M K_2SO_4 solution served both as the anolyte and catholyte. Aqueous acid (HCl) and base (KOH) were circulated at a flow rate of 20 ml min^{-1} through acid and base

chambers, where stir bars were set at 400 rpm to enhance the mass transport within both chambers. A BPM was sandwiched between the acid and base chamber and operated in a forward-bias mode with the CEL facing toward the acid chamber. Two Luggin capillaries holding Ag/AgCl reference electrodes were positioned in the acid and base chambers to directly measure the voltage drop across BPMs (V_{BPM}). KCl was produced through the neutralization reaction in a separate product chamber located between the acid and anode chambers (**Figure 5.2**). This custom cell design enables the precise measurement of V_{BPM} by minimizing the impacts of electrode stability, anode/cathode reactions, and solution resistance.[45]

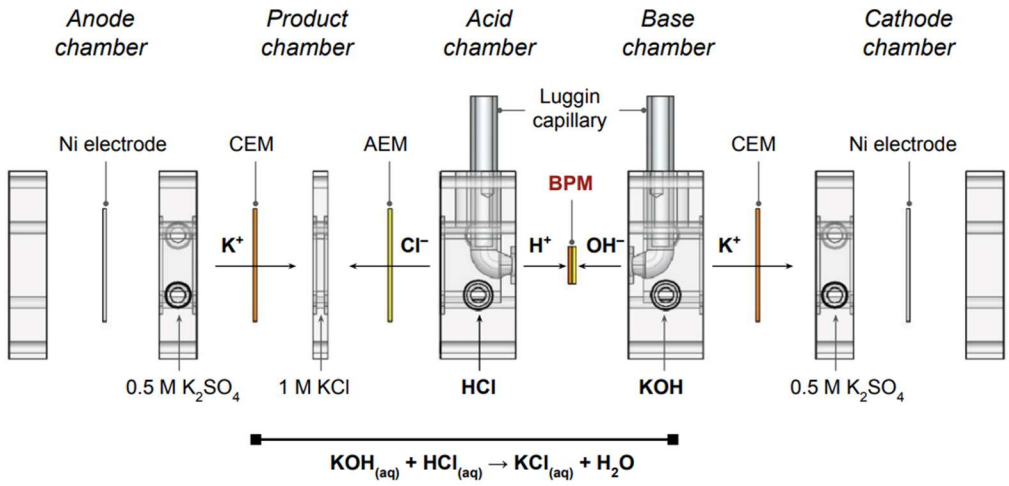

Figure 5.2 A custom electrodialysis cell for direct measurement of BPM voltage drops in forward-bias mode. Expanded view of the flow electrodialysis cell used in this work consisting of anode, product, acid, base, and cathode chambers. A bipolar membrane separates the acid and base chambers, and a product chamber was placed between the anode and acid chamber to collect KCl. Nickel foils were used as both the anode and cathode, and 0.5 M K_2SO_4 solution served as both the anolyte and catholyte. Ag/AgCl reference electrodes were held in two Luggin capillaries, which were positioned in the acid and base chambers.

Our previous study showed that a BPM consisting of a Nafion membrane as the CEL and a PiperION membrane as the AEL enables sufficient water transport

to the BPM junction at 1A cm^{-2} in reverse-bias, whereas a commercial BPM encounters "water starvation" at junctions.[121] Therefore, it is hypothesized that the combination of Nafion and PiperION membranes could also enable rapid water removal from the BPM junctions to prevent flooding of the junction in forward-bias mode. Previously, the aim was to reduce ion and water transport limitations for reverse-bias BPM by minimizing the thickness of ion exchange layers.[121] However, this principle does not necessarily apply to forward-bias BPM designs, as reducing the thickness of the ion exchange layer can lead to an increase in H^+/OH^- leakage, which significantly reduces voltage efficiency. Achieving optimal forward-bias BPM performance requires a careful balance between these competing factors, which can be modulated by the CEL and AEL thickness.

To investigate the effects of AEL and CEL thickness on V_{BPM}, thickness was independently varied and measured V_{BPM} over a wide range of current densities from 0 to 200 mA cm^{-2}. By keeping the CEL thickness constant at 125 μm, it was found that a thinner AEL resulted in a higher V_{BPM}, up to comparable performance observed for 15 and 20 μm thick AELs (**Figure 5.3a**). After selecting the thinnest AEL (15 μm), the effect of CEL thickness on V_{BPM} were further investigated. It was observed that the asymmetric BPM architecture with the thickest CEL (225 μm) resulted in the highest V_{BPM} of 230 mV at 200 mA cm^{-2} (denoted as "**aBPM**") (**Figure 5.3b**). This asymmetric BPM was also tested in different concentrations of HCl and KOH (**Figure 5.3c**). Surprisingly, a decrease in V_{BPM} when increasing the acid/base concentrations from 1 to 2 M was observed. Furthermore, the V_{BPM} decreased for j >

50 mA cm^{-2} when the acid/base was diluted to 0.5 and 0.25 M, as the diluted reactants (H^+ and OH^-) imposed mass transport limitations at high current densities.

The **aBPM** was benchmarked against a commercially available BPM (Fumasep BPM) and found that the Fumasep BPM showed higher V_{BPM} values at j < 30 mA cm^{-2}, indicating lower H^+/OH^- leakages. However, the Fumasep BPM failed, with the V_{BPM} approaching 0 mV, at j > 50 mA cm^{-2} due to "flooding" of the BPM junctions. The poor water transport phenomena of the Fumasep BPM were attributed to the presence of a reinforcement layer,[16] as well as a tightly laminated junction (**Figure S5.1**). In contrast, the custom **aBPM** allows for operation at 200 mA cm^{-2} with a yield of 230 mV voltage (**Figure 5.3d**).

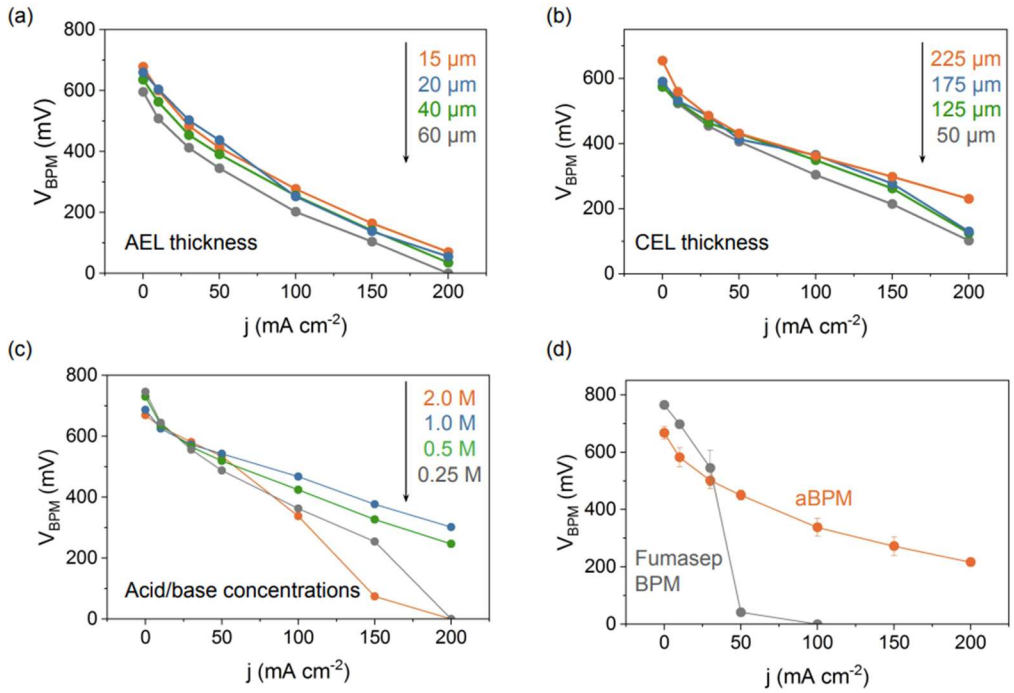

Figure 5.3 Electrochemical characterization of the BPMs made from Nafion (CEL) and PiperION (AEL) membranes. (a) Polarization curves for AEL thicknesses ranging from 15 to 60 µm when coupled with a 175 µm thick CEL. (b) Polarization curves for CEL thicknesses ranging from 225 to 50 µm when coupled with a 15 µm thick AEL. (c) Polarization curves for the BPM with 0.25 to 2.0 M acid/base feedstocks. The acid concentration equals the base concentration in all experiments. (d) Comparison of the **aBPM**, consisting of a 225 µm CEL and a 15 µm AEL, with the commercial Fumasep BPM.

Although the acid-base neutralization is kinetically fast (~1.3 $\times 10^{11}$ M^{-1} s^{-1} at 25°C), previous studies have demonstrated that adding catalysts to BPM junctions can significantly facilitate this reaction by providing a larger volume of reaction sites.[16] Due to the extreme pH microenvironment at BPM junctions, the catalysts must be chemically stable under extreme acidic and basic conditions, therefore, high surface, acid/base resistant nanocarbons could be ideal candidates. Catalysts furnished BPMs were assessed by spin-coating the same quantity (i.e., 10 mg catalysts in the ink) of graphene oxide (GrOx), graphene nanoplatelets (GN),

carbon black (CB) and TiO_2 inks at the BPM junctions. The GO-furnished BPM (denoted as "**aBPM-GO**") outperformed the GN, CB and TiO_2-furnished BPMs after re-optimizing the AEL/CEL thickness and deposition method (**Figures 5.4a, S5.2, 3**). One possible reason for the observed performance trend could be that the 2D GROX formed a thin and flat catalyst layer, reducing ion transport limitations and increasing H^+/OH^- concentrations at BPM junctions. Furthermore, optimizing GrOx coverage in the junction is crucial for the best BPM performance. It was demonstrated that 3 layers of spin coat GrOx provides satisfactory coverage, as confirmed by SEM images (**Figure 5.4b, c**). However, excessive GrOx deposition (e.g., five time GrOx deposition) can lead to a denser and thicker catalyst layer (**Figure 5.4c**). Although it can provide more reaction sites, it can also lead to poorer adhesion and increases in the thickness of the catalyst layer, which dilutes the reactant concentrations and hinders ion transport.

The thermodynamic V_{BPM} with 1 M H^+ and OH^- feedstocks is ~826 mV, based on a ΔpH of 14 across the membrane.[122] However, discrepancies were noticed between the V_{BPM} of **aBPM-GROX** and the thermodynamic value, particularly at $j > 100$ mA cm^{-2}, which could be attributed to several factors including ion and water mass transport limitations, H^+/OH^- leakage, ohmic resistances, etc. (**Figure 5.4d**). To resolve the role of ohmic resistance to this loss, a four-point electrical conductivity measurement was conducted on Nafion and PiperION and iR_{CEL} and iR_{AEL} were calculated at corresponding current densities. Solution ohmic losses ($iR_{solutions}$) were determined by measuring voltage drops across two Luggin capillaries without BPMs. It is noted that the CEL imposes significantly

ohmic losses (51.5 mV at 200 mA cm^{-2}) compared to AEL (4.1 mV at 200 mA cm^{-2}) due to the thickness difference (175 µm *c.f.* 15 µm). Furthermore, the CEL's ohmic losses are even greater than the solution's ohmic losses (~30.0 mV at 200 mA cm^{-2}). The solution ohmic loss corresponds to a mere ~300 µm distance between the Luggin capillary and the BPM surface, highlighting the effectiveness of using a Luggin capillary for V_{BPM} measurement.

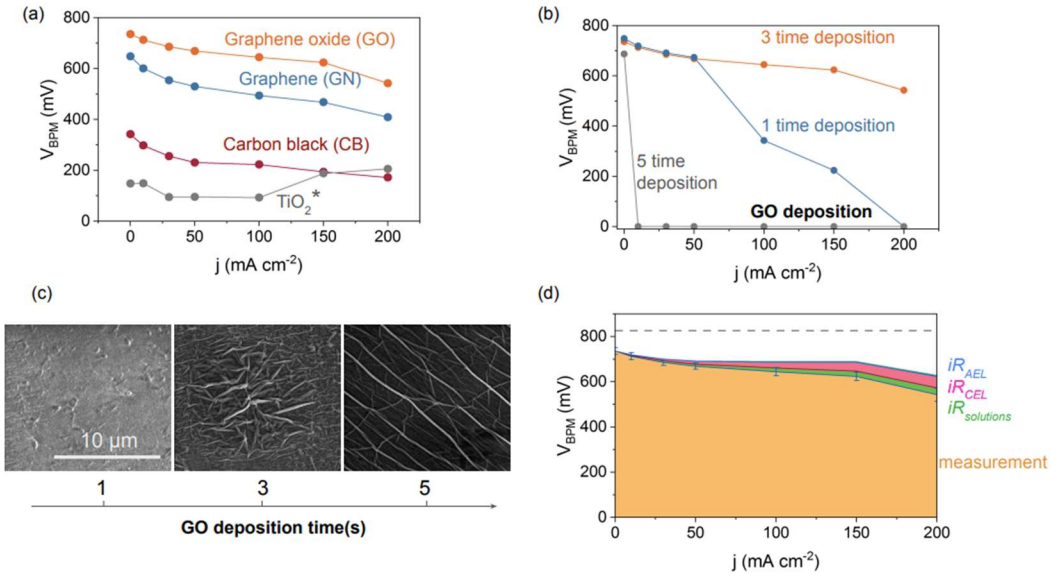

Figure 5.4 Electrochemical characterization of the catalyst furnished BPMs. (a) Polarization curves for the BPM containing graphene oxide (GO), graphene nanoplatelets (GN), carbon black (CB), and TiO_2 at the junctions. The TiO_2 furnished BPMs showed unstable V_{BPM}, and the values reported are average values for the first 30 seconds. The rest V_{BPM} values are average values over 30-200 seconds. (b) Polarization curves for the BPMs with various GrOx deposition times. The optimal performance was observed for three time GrOx deposition. (c) SEM images of GROX on the Nafion CEL after one-, three- and five-time deposition. (d) Sum of voltage contributions due to CEL ohmic loss, AEL ohmic loss, and solution ohmic loss. All BPMs are made from 175 µm Nafion and a 15 µm PiperION (**Figure S5.2**). All experiments are performed with 1 M HCl and 1 M KOH.

The power densities for Fumasep BPM, **aBPM**, and **aBPM-GROX** was also evaluated, at 0 to 200 mA cm^{-2} with 1 M H^+ and OH^- (**Figure 5.5a**). The Fumasep BPM exhibited a peak power density of 16.4 mW cm^{-2} at 30 mA cm^{-2} and quickly experienced a deleterious decrease at 50 mA cm^{-2}. Both **aBPM** and **aBPM-GrOx** have asymmetric architectures that facilitate rapid water transport, allowing them to operate at 200 mA cm^{-2}. **aBPM-GrOx** doubled the power density of **aBPM** because the GrOx layer significantly enhances the acid-base recombination.

A forward-bias BPM fails immediately once the junction is flooded, which dramatically amplifies the internal resistance and disrupts the junction structure, leading to "failure." To understand the stability of the **aBPM**s in forward bias, 24-hour durability of Fumasep BPM, **aBPM**, and **aBPM-GrOx** in the electrodialysis cell at 50 mA cm^{-2} was measured. The output voltage of the **aBPM** decreased ~6.8% after 24-hour operation, while the Fumasep BPM completely failed within the first 15 minutes. Incorporating the GrOx layer improves the BPM durability, resulting in only a ~1.6% voltage drop after 24 hours. All electrolytes were refreshed every 6 hours to ensure that the decreased performance was not from reactant concentration reduction. These results demonstrate that the asymmetric BPM architecture can sustainably remove water from the junctions and output a stable voltage for an extended period.

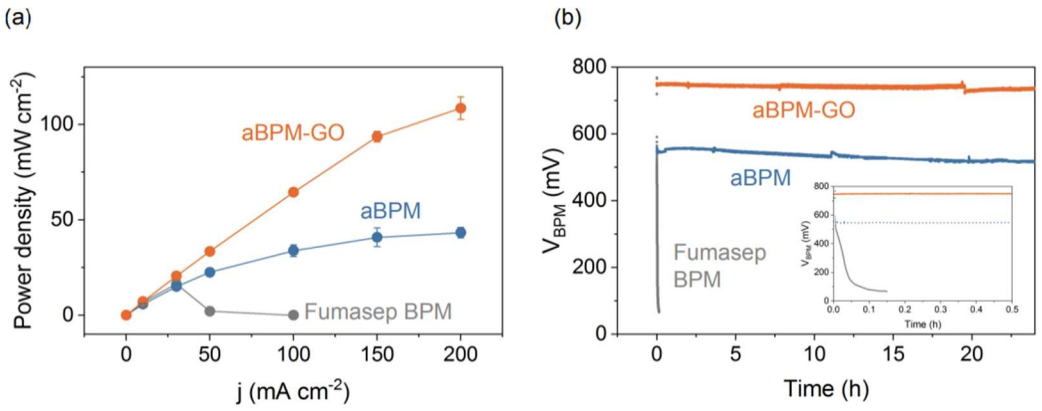

Figure 5.5 Evaluation of power density and durability of various BPMs. (a) Power density comparison of Fumasep BPM, **aBPM**, and **aBPM-GrOx** using 1 M HCl and 1 M KOH electrolytes at different current densities. (b) 24-hour durability test conducted at a constant current density of 50 mA cm^{-2}, with periodic electrolyte refreshment every 6 hours.

To maintain sustainable operations of a forward-bias BPM, it is crucial to manage water transport, effectively ensuring that the influx of water towards the membrane equals the efflux of water leaving the membrane. Water flow into BPM junctions occurs through two main mechanisms: 1) water generation via acid-base neutralization (represented as $J_{Reaction}$, **Equation 5.3**, V_{mol} = 18.015 ml mol^{-1}, F = 96485.33 s A mol^{-1}), and 2) water transport with solvated ions, also known as electro-osmotic drag (represented as J_{EOD}). Deuterium (D)-labeled electrolytes were employed to quantify the $J_{reaction}$ and J_{EOD} by directly measuring the water removal fluxes from AEL (represented as $J_{H2O, AEL}$) and CEL (represented as $J_{H2O, CEL}$) based on **Equation 5.4 and 5.5**. To accurately measure $J_{H2O, AEL}$ and $J_{H2O, CEL}$, 20 vol% D_2O was added to the acid and base chambers, respectively, and analyzed the D concentration at the opposite side of the membrane using a highly sensitive isotopic water analyzer (**Figure 5.6a**). **aBPM-GrOx** was used to study water transport because it is the only BPM that can operate sustainably at high current densities.

Further details on the experimental setup and analysis can be found in the Supporting Information.

$$J_{Reaction} = (I \times t \times V_{mol})/F \quad (5.3)$$

$$J_{H2O,\,AEL} + J_{H2O,\,CEL} = J_{reaction} + J_{EOD} \quad (5.4)$$

$$J_{EOD} = J_{H2O,\,AEL} + J_{H2O,\,CEL} - J_{Reaction} \quad (5.5)$$

Electrolysis was conducted for 60 minutes at current densities of 0, 30, 100, and 150 mA cm^{-2} and monitored the water fluxes from the AEL and CEL every 10 minutes. No change was observed in the D concentration in either the acid or base chamber when solution was flowed without any applied currents for 60 minutes (the electrolytes were recirculating), indicating minimal electrolyte crossover through diffusion. For water transport experiments with applied current, the amount of water that escaped from the AEL vs. the CEL was comparable at all tested current densities despite the CEL being approximately eight times thicker than the AEL (175 μm vs. 20 μm). This result was confirmed by the independent water osmosis rate measured through a 175 μm CEL ($J_{H2O,\,CEL}$, 0.001116 ml min^{-1}) and 20 μm AEL ($J_{H2O,\,AEL}$, 0.000672 ml min^{-1}).

In addition, it was observed that the influx of water (equaling efflux of water) from the BPM did not increase proportionally with the current density. Instead, it first decreased from 30 to 100 mA cm^{-2} and then increased as the current density increased from 100 to 150 mA cm^{-2}.[123] At 30 mA cm^{-2}, the average EOD coefficient measured in this work was ~5, indicating that a solvated proton or

hydroxide ion can transport more than five water molecules. However, the EOD coefficient decreased significantly with increasing current densities, reaching ~1 at 100 mA cm^{-2} and ~0.6 at 150 mA cm^{-2}, which is consistent with previous studies.[123] As the current density increases from 30 to 100 mA cm^{-2} in a BPM, J_{EOD} dominates the influx of water. However, at higher current densities of 100 to 150 mA cm^{-2}, the contribution of J_{EOD} and $J_{Reaction}$ to water influx becomes almost equal. When the current density surpasses 150 mA cm^{-2}, the $J_{Reaction}$ becomes the dominant factor, as the EOD coefficient drops to below 0.6. When $J_{Reaction}$ dominates the water influx, higher current densities (j > 150 mA cm^{-2}) result in an overall increase in water influx. However, as the primary drive force for water efflux, osmosis decreases at higher current densities because the concentration of H^+ and OH^- reduces at the electrolyte-membrane interface due to the rapid consumption of H^+ and OH^- as reactants. Eventually, the water influx surpasses the water efflux, leading to membrane failure.

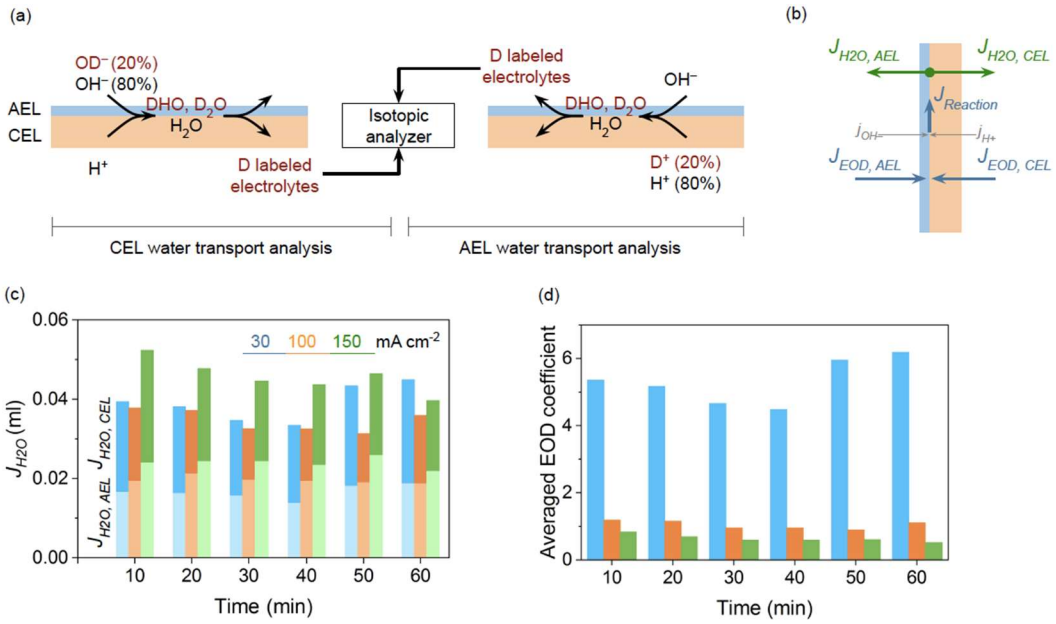

Figure 5.6 Water transport analysis in forward-bias BPMs. (a) Schematic diagram of the water transport analysis using deuterium (D)-labeled electrolytes. The acid chamber was fed with 20 atm% D^+ as feedstock, and the δD was monitored using an isotopic water analyzer in the base chamber for the AEL water transport analysis and in the acid chamber for the CEL water transport analysis. (b) Illustration of the water mass balance for a BPM in forward-bias mode, which accounts for water from acid-base reaction, electro-osmotic drag (EOD), and water removed from AEL and CEL ($J_{H2O,\ AEL}$ and $J_{H2O,\ CEL}$). (c) Non-cumulative $J_{H2O,\ AEL}$ and $J_{H2O,\ CEL}$ within 60 minutes at 30, 100 and 150 mA cm^{-2}. For instance, "20 mins" refers to 10-20 minutes. (d) Averaged EOD coefficient values measured at 30, 100, and 150 mA cm^{-2}. All experiments were carried out using **aBPM-GrOx**.

5.3 Conclusion

This work demonstrates the successful implementation and optimization of a forward bias BPM, composed of a Nafion membrane as CEL, PiperION membrane as AEL, and GrOx catalyst. Significant performance improvement over previously published work as well as the commercial Fumasep BPM are achieved. When tested in the custom flow cell, the **aBPM** achieved operation up to 200 mA cm^{-2} with a yield of ~580 mV voltage, establishing a power density of 109 mW cm^{-2}

[2]. Furthermore, this BPM demonstrated stability for over 24 hours at 50 mA cm^{-2} with a voltage decrease of only ~1.6%, significantly better than the commercial Fumasep BPM, which failed after only 10 minutes.

Furthermore, this high-performing BPM offers an unprecedented opportunity to fundamentally investigate water transport (employing isotopic labeling) and elucidation of failure mechanisms at a wide range of current densities. The results unveil the dominant mode of water transport at low, intermediate, and high current densities. At < 30 mA cm^{-2} water influx is predominantly due to EOD, then between ~100 and 150 mA cm^{-2} influx becomes dual-dominant between EOD and acid-base recombination, and finally, at current densities > 150 mA cm^{-2} acid-base recombination dominates water influx. In summary, we report a stable, high current density BPM for forward bias operation along with a novel investigation into water transport mechanisms in forward bias BPMs, elucidating three current density dependent water transport modes.

5.4 Materials and Methods

Materials: Nafion NR212 (50 μm, Fuel Cell Store), Nafion 115 (127 μm, Fuel Cell Store), PiperION A15R (15 μm, Versogen), PiperION 20 (20 μm, Versogen), PiperION 60 (60 μm, Versogen), Fumasep FAB-PK-130 (110-140 μm, Fuel Cell Store), Fumasep FKB-PK-130 (110-140 μm, Fuel Cell Store), Nafion D520 (5 wt% Ionomer, Fuel Cell Store, IonPower), graphene oxide paste (30 g/L, Graphene Supermarket), graphene nanoplatelets (6-8 nm thick, 25 μm wide), carbon black (Ketjenblack EC-600 JD), D_2O (99%, Sigma Aldrich), potassium chloride (KCl,

Sigma Aldrich), hydrochloric acid (HCl, Sigma Aldrich), potassium hydroxide (KOH, pellets, Sigma-Aldrich). All membranes were received in dry form, pretreated according to manufacturer's instructions before use, and stored in DI water (CEMs) or 1 M NaOH (AEMs). All chemicals were used as received.

Catalyst ink: The catalyst inks were prepared by reducing the concentration of graphene oxide paste (Graphene Supermarket) from 30 g/L to 10 g/L. However, the direct preparation of inks using a concentration of 10 g/L for graphene, activated carbon black, and TiO_2 was not feasible. To ensure a fair comparison, it was ensured that the catalysts effectively covered the entire membrane surface, similar to the coverage achieved with GO.

BPM fabrication: A pre-cut 1.5x1.5 cm square of Nafion membrane was soaked in DI water for at least an hour (after the pretreatment of 1 M HCl treatment at 90°C for 1 h). Once removed from the water bath, it was placed on a glass slide and gently dried using a Kim wipe. Next, the membrane was taped on all four sides to the glass slide with Kapton tape. Catalyst ink was then applied to the Nafion membrane using spin coating at 3000 rpm for 30 sec. The Nafion membrane with the catalyst was then heated in an oven at 100°C for 2 min. This process could be repeated for additional layers up to five layers. The Nafion membrane with the catalyst was then soaked in a 1 M HCl bath for at least two hours for rewetted and sandwiched with the desired thickness of PiperION membrane. Care was taken to press out any air pockets, and the membranes were tested immediately after assembly. The BPM without a catalyst did not require any catalyst deposition procedure.

Electrodialysis cell design/assembly: Figure 2 shows a schematic of the electrodialysis cell used for testing the BPMs in this work. The cell consisted of, from

left to right in schematic, an anode, an anolyte chamber, a CEM, a dilute chamber, an AEM, an acid chamber, a BPM (1 cm^2 active area), a base chamber, a CEM, a catholyte, and a cathode. Both the anode and cathode consisted of Ni foil with copper tape as leads. Aqueous 0.5 M K_2SO_4 was used as both the anolyte and the catholyte and was recirculated through both chambers at ~10 mL min^{-1}. Aqueous 1 M KCl was recirculated at ~2 mL min^{-1} through the dilute chamber and aqueous HCl and KOH flowed through the acid and base chambers at 20 mL min^{-1}. Both CEMs used in the cell stack were Nafion N324 (280 μm, Fuel Cell Store) and the AEM was Fumasep FAB-PK-130 (130 μm, Fuel Cell Store). Luggin capillaries holding Ag/AgCl reference electrodes (CHI111, CH Instruments) were placed in the acid and base chambers to allow for the most direct measurement of the voltage across the BPM.

Chronopotentiometry: After the electrodialysis cell described above was assembled, potentiostat (Biologic SP 300) leads were attached in a four-point measurement configuration so that a current could be applied across the full cell and the resulting voltage could be measured directly across the BPM. Chronopotentiometry measurements were used to obtain all reported data for all polarization curves. For each point, a chosen current was applied across the anode and cathode and held steady, and voltage reported here is the average voltage between the 30-200 sec. The current was then increased to the next value and the process was continued until all desired current measurements were performed. The final reported voltage values are averages of the voltage collected over the steady state region for each chronopotentiometry step.

Ohmic resistance measurements: the electrical conductivities of Nafion and PiperION are measured to be 68 and 74 mS cm^{-1} using a four-point probe, therefore

the iR_{CEL} and iR_{AEL} can be calculated at corresponding current densities. For the solution resistance measurement, no membrane was placed between the acid and base chambers. 1 M HCl was added to the chambers and the voltage drops were recorded at each current density (iR_{acid}), and the iR_{base} values were measured using the same methodology.

Electrochemical Impedance Spectroscopy (EIS): EIS measurements were performed in the same electrodialysis cell as the chronopotentiometry measurements. For each BPM tested, measurements were performed at 50 mA cm^{-2}. For each step, the current was held for 10 sec, then scanned from 600 kHz to 20 Hz with an amplitude of 5-10% of the current, recording every 0.5 sec.

Water transport measurement: 10 mL of D_2O was added to 40 mL of 1 M HCl as the acid feedstock, the deuterium atoms (D) present in the D_2O rapidly replaced the protons present in the electrolyte, reaching an equilibrium of $c(D^+) : c(H^+) = 1: 4$ as per **Equation 5.5**.

$$H^+ + D_2O \rightleftharpoons D^+ + DHO \qquad (5.5)$$

50 mL of 1 M KOH was used as the base feedstock. The water transport was measured at various current densities (0, 30, 100, and 150 mA cm^{-2}) using the test conditions described in the Chronopotentiometry section. Before electrolysis, the D containing electrolytes are recirculated for 10 min to ensure the D^+ or OD^- reach equilibrium with H^+ or OH^- within the membranes that attach to the fixed charges. After electrolysis for every 10 min, 50 µL of the electrolyte from the base chamber was transferred to a 2 mL vial and mixed with 950 µL of DI water. The δ D of the

resulting samples was measured using the Picarro L2140-i isotopic water analyzer. δ D is defined by **Equation 5.6** below, and a standard 500 ppm D sample was used for calibration.

$$\delta D = \left(\frac{\left(\frac{D}{H}\right)_{sample}}{\left(\frac{D}{H}\right)_{standard}} - 1 \right) \times 1000‰ \quad (5.6)$$

Excel was then used to calculate the amount of DHO generation. It should be noted that a D concentration of 156 ppm was used for the DI water that was used to dilute the samples. Because the original volume of KOH for the base chamber is 50 ml, and the samples were all diluted for 20-fold, therefore, the overall amount of treated electrolyte is 1000 ml. Finally, the amount of DHO (V (DHO), ml) required to obtain the $\left(\frac{D}{H}\right)$ can be calculated. The theoretical amount of DHO generated V (DHO, calculated) at various current densities can be calculated based on **Equation 5.7**. Note that the authors acknowledged that DHO is not the only product at the AEM side, D_2O could also be generated via D-H swapping, but it does not affect the calculations and the final results.

$$\text{V (DHO, calculated)} = (I \times t) / F \times 18.015 \text{ ml/mol} \quad (5.7)$$

where I represent the current passing through the BPMs, and t represents the electrolysis time. F is the Faraday constant (96485.33 s A mol^{-1}).

A similar methodology was used for the water transport of CEL measurement. 10 mL of D_2O was added to 40 mL of 1 M KOH as the acid feedstock. After electrolysis for every 10 min, 50 μL of the electrolyte from the acid chamber

was transferred to a 2 mL vial and mixed with 900 µL of DI water and 50 µL 1 M KOH. The reason to neutralize the sample before sending it to the Picarro L2140-i isotopic water analyzer is to protect the sensor of the instrument. However, the dilution factor remains 20 unchanged.

5.5 Supplemental Figures

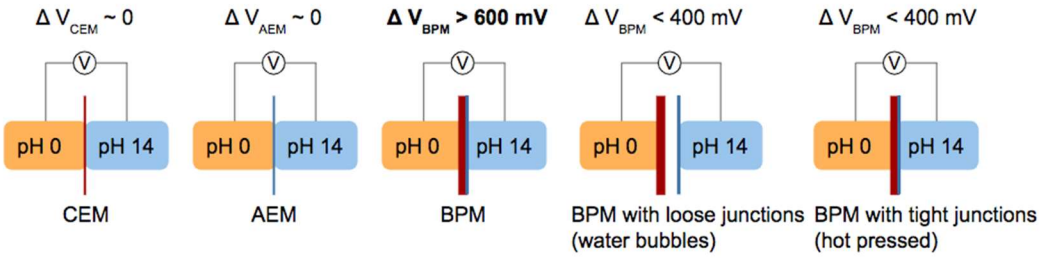

Figure S5.1 Investigation on the impact of the tightness of a forward-bias BPM junction on its performance. In a single CEM or AEM, there is no voltage drop due to the absence of Donnan repulsion for H^+ and OH^- ions, respectively. However, for BPM junctions, the thickness can be intentionally modified to three levels from left to right: electrostatic attached junction, loss junctions with water bubbles, or tight junctions with hot-pressed AEL and CEL. Results showed that the electrostatic attached junction exhibited the best performance, indicating that either too loose or too tight junctions are not ideal for a forward-bias BPM.

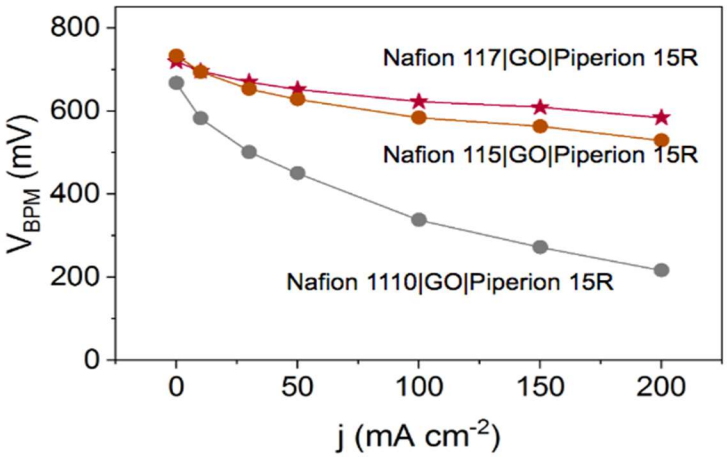

Figure S5.2 Optimization of AEL and CEL thickness after adding GrOx catalyst layer. The best combination is 175 μm thick Nafion with 15 μm thick PiperION.

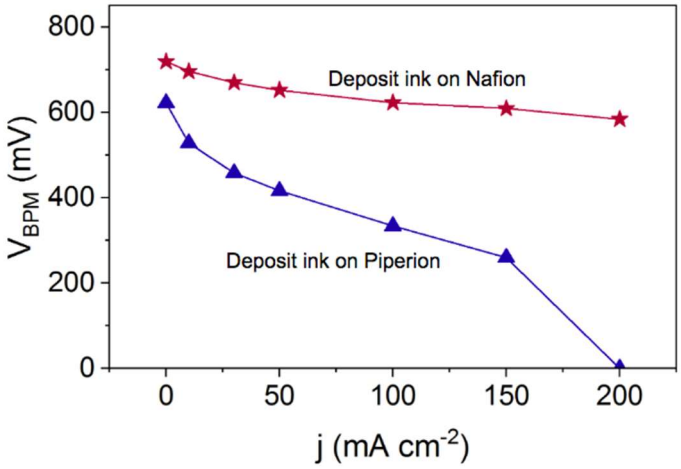

Figure S5.3 The BPM performance when depositing inks on Nafion or PiperION layers.

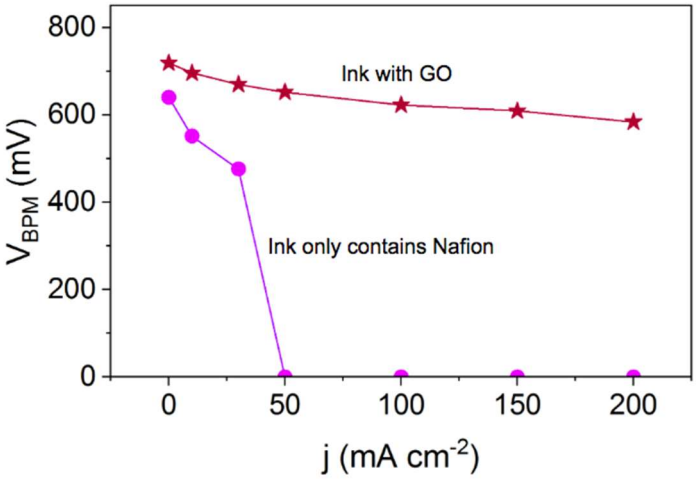

Figure S5.4 A control experiment showing the GrOx is the active catalyst.

Chapter 6: Bipolar Membranes for Electrochemically Mediated Carbon Removal

Content drawn from: Justin C. Bui, Éowyn Lucas, Eric W. Lees, Andrew K. Liu, Harry A. Atwater, Chengxiang Xiang, Alexis T. Bell, and Adam Z. Weber. Modeling Bipolar Membranes for Electrochemical Carbon Capture.

And: Yayuan Liu, Éowyn Lucas, Ian Sullivan, Xing Li, and Chengxiang Xiang. Challenges and opportunities in continuous flow processes for electrochemically mediated carbon capture. iScience. Volume 25, Issue 10. 2022. DOI: 10.1016/j.isci.2022.105153

6.1 Introduction

During my PhD, I assisted with writing a review paper about electrochemical flow systems for carbon removal. I also performed experimental measurements supporting a computational study on BPM reaction mechanisms in bicarbonate, carbonate, and simulated sea water electrolytes for carbon capture applications. This chapter combines those works, highlighting my main contributions. More details and supporting information can be found in the full texts cited at the beginning of this chapter.

As discussed in previous chapters of this thesis, carbon capture technology is vital for mitigation and reversal of climate change. This chapter focuses on BPM-ED systems and fundamentals for DAC. Currently, most DAC companies use solid or liquid sorbent materials to capture CO_2 from the atmosphere or a point source. One prominent example is Carbon engineering, which uses alkaline aqueous sorbents (i.e., $KOH_{(aq)}$) to capture ambient CO_2 as mixtures of (bi)carbonates. The CO2 is then released from the sorbent via thermal regeneration, creating a pure CO2 stream which can be sequestered or converted to useful products. [124] **Figure 6.1a** depicts a typical

DAC process. Unfortunately, this method for CO2 removal is energy intensive and expensive due mainly to a significant thermal energy penalty (>150 kJ mol^{-1}) required to regenerate the sorbent material.[125] Furthermore, the thermal energy is typically provided via burning of fossil fuels, which results in CO_2 emissions and reduces the net amount of CO_2 removed from the atmosphere.

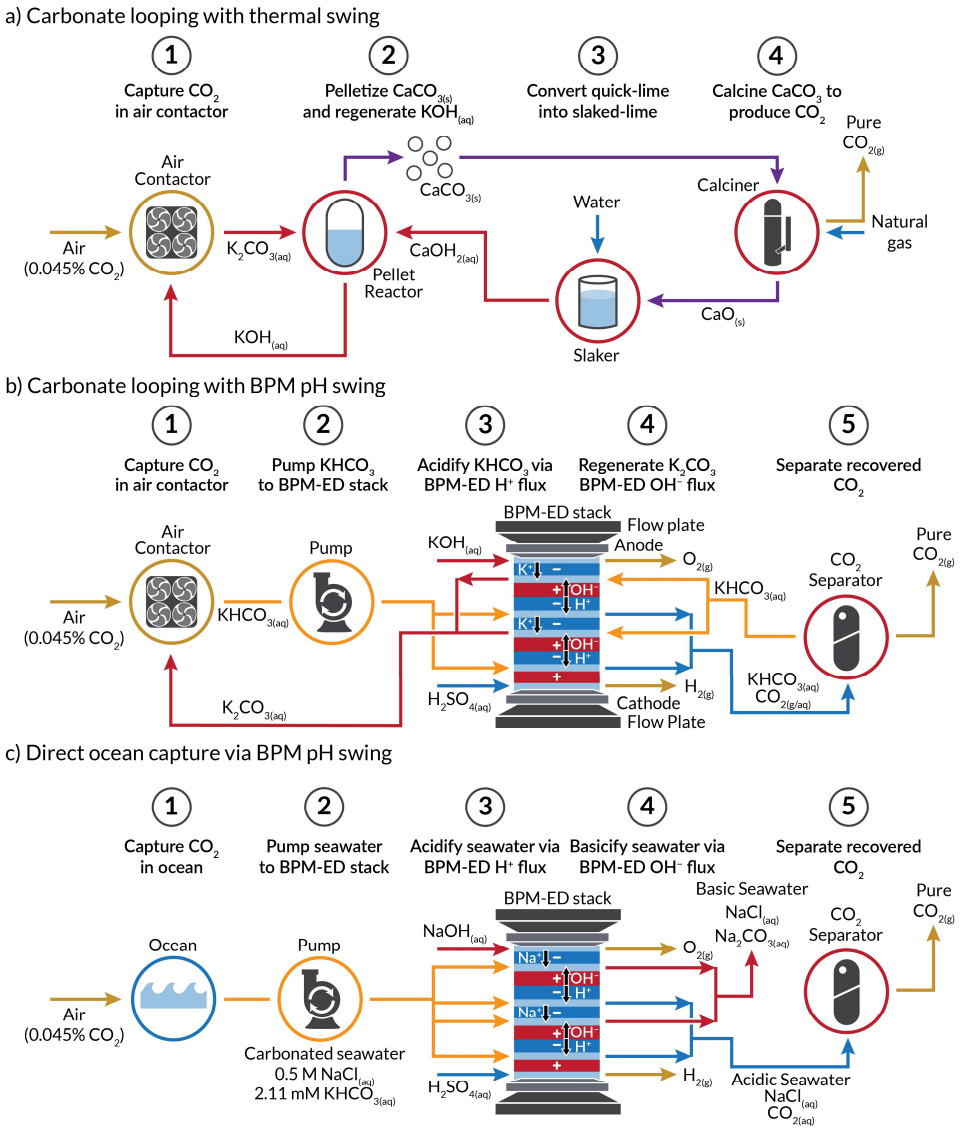

Figure 6.1 Process flow diagrams of various carbon capture processes. (a) Carbonate looping with thermal swing desorption. (b) Carbonate looping with electrochemical pH swing desorption via BPM. (c) Direct ocean capture with electrochemical pH swing desorption via BPM.

As discussed in previous chapters, electrochemically-mediated carbon capture (EMCC) can address the challenges associated with thermal sorbent regeneration by using low-cost renewable electricity for capture and release of CO_2 from the sorbent.[126–138] Specifically, BPM-ED is a promising EMCC technology, which uses WD to mediate CO_2 capture and sorbent regeneration, as depicted in **Figure 6.1b**.[139–141] A key advantage of BPM-ED is the use of water as the reactant, which enables higher current densities than other EMCC technologies due to the high concentration of water (55 M) in aqueous CO_2 capture solutions. However, the energy intensity of BPM-ED typically exceeds 300 kJ mol^{-1} because of the water dissociation overpotential and ohmic resistances in the BPM and current commercial BPMs struggle to maintain stable operation above 100 mA cm^{-2}. Therefore, further optimization is required for BPM-ED to become more efficient than thermal CO_2 sorbent regeneration.[142]

$$\mathrm{H_2O} \overset{k_1, k_{-1}}{\leftrightarrow} \mathrm{H^+ + OH^-} \qquad K_1 = 1 \times 10^{-14} \quad (2)$$

$$\mathrm{CO_{2(aq)} + H_2O_{(l)}} \overset{k_2, k_{-2}}{\leftrightarrow} \mathrm{H^+_{(aq)} + HCO^-_{3(aq)}} \qquad K_2 = 4.27 \times 10^{-7} \quad (3)$$

$$\mathrm{HCO_3^-} \overset{k_3, k_{-3}}{\leftrightarrow} \mathrm{H^+ + CO_3^{2-}} \qquad K_3 = 4.58 \times 10^{-11} \quad (4)$$

$$\mathrm{CO_{2(aq)} + OH^-} \overset{k_4, k_{-4}}{\leftrightarrow} \leftrightarrow \mathrm{HCO_3^-} \qquad K_4 = 4.27 \times 10^{7} \quad (5)$$

$$HCO_3^- + OH^- \overset{k_5, k_{-5}}{\leftrightarrow} H_2O + CO_3^{2-} \qquad K_5 = 4.58 \times 10^3 \quad (6)$$

The energy intensities for BPM-ED reported in the literature (300-1000 kJ mol^{-1} CO_2) are significantly higher than the minimum thermodynamic energy actually required to capture CO_2 from air (20 kJ mol^{-1}).[136] Unfortunately, very few theoretical studies have simulated BPMs immersed in carbon-containing solutions to resolve the dominant energy losses and there is little precedent for modeling the transport of dilute carbon species in seawater feedstocks used for DOC.[135,143] In this chapter, results from a comprehensive model of BPM-ED based on prior work modeling multi-component transport in BPMs are presented,[144] now with the homogeneous reaction kinetics of reactive carbon species (**Equations 2-5**). Furthermore, the model is validated to experimental data in various carbon-containing solutions and is used to elucidate the nature of *in situ* CO_2 generation and sorbent regeneration in BPMs employed for EMCC. Experimental work visualizing and examining the dependance of bubbling on flow rate and current density is also presented.

6.2 Results and Discussion

To understand the transport and reaction kinetics of reactive carbon species in BPMs, experimental polarization curves were taken in the custom electrodialysis cell for a BPM immersed in three electrolytes relevant to carbon removal systems: 1 M $KHCO_3$, 0.5 M $KHCO_3$, and simulated seawater (0.00211 M $NaHCO_3$ + 0.5 M NaCl). Simulations of the BPM under polarization in these varying electrolytes were

run and compared to the experimentally measured polarization curves. Strong agreement is seen for all three carbon-containing electrolytes for a single set of fitting parameters (**Figure 6.2a** and **Figure 6.3**). Remarkably, the simulation can capture the non-intuitive polarization behavior occurring at current densities < 20 mA cm^{-2}. At this region, there is an initial onset in current density at ~0.4 V of applied membrane potential for both the 0.5 M $KHCO_3$ and 1 M $KHCO_3$ BPMs. The current density of these BPMs increases approximately linearly until ~0.7 V where it then takes off exponentially. For the seawater scenario, more typical BPM polarization behavior is observed. The current density does not have an initial takeoff at 0.4 V, so between 0.4 and 0.8 V the seawater BPM drives less current density than the $KHCO_3$ BPMs. However, past ~0.7 V the current generated in the seawater BPM exceeds that of the $KHCO_3$ BPMs.

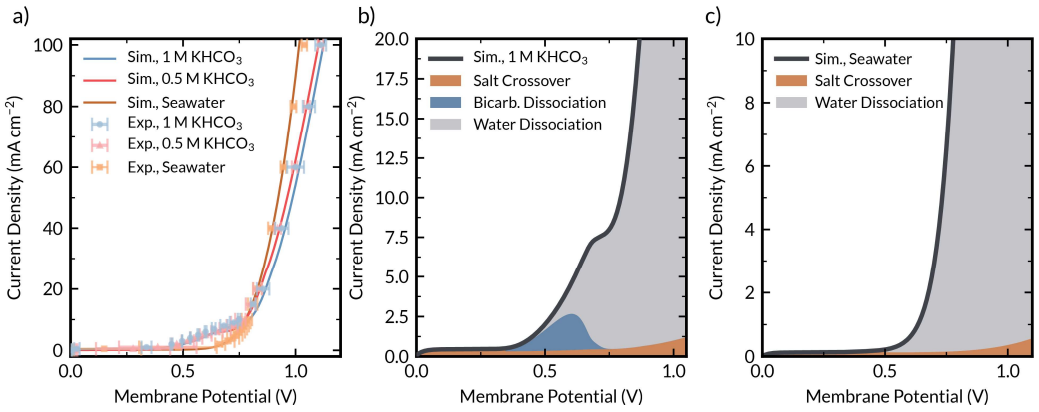

Figure 6.2 (a) Agreement between experimental (markers with error bars) and simulated (solid lines) polarization curves for BPMs immersed in various solutions of aqueous bicarbonate. (b-c) Breakdown of partial current density in the BPM junction due to contributions of salt crossover (orange), bicarbonate dissociation (blue), and water dissociation (gray) for a BPM immersed in (b) 1 M $KHCO_3$ and (c) simulated seawater. The y-scale for panels (b) and (c) are zoomed into highlight the unique behavior of the carbon-containing BPMs at low current densities.

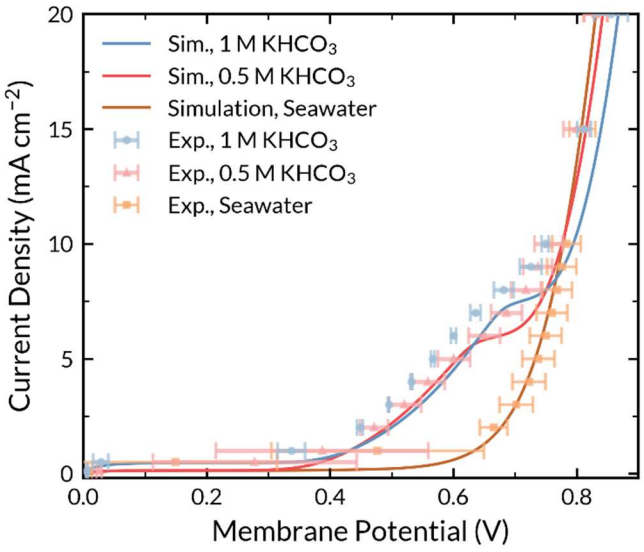

Figure 6.3 Comparison of experimental (markers) and simulated (solid lines) polarization curves from the 4-probe BPM measurement in various electrolytes for $i < 20$ mA cm^{-2} (within the salt crossover and bicarbonate dissociation regime).

Within the BPM junction, the current density is due to either the crossover of unreactive co-ions (K^+, Na^+, or Cl^-), or to the presence of electric field enhanced, net-charge-generating dissociation reactions. These contributions to the overall polarization curve were computationally determined and are shown in **Figure 6.2b** and **6.2c** for BPMs operating in 1 M $KHCO_3$ and simulated seawater, respectively. As discussed in **Chapter 1**, the current density for the simulated seawater case is primarily driven by salt crossover at low potentials and WD at high potentials.[145,146] The 1 M $KHCO_3$ polarization curve, however, is more intriguing. While previous studies have suggested that the low applied potential current onset for BPMs in weak buffer electrolytes is entirely driven by titration currents resulting from dissociation of the weak acid buffer (i.e., the HCO_3^- anion in this case) in the BPM junction,[145,147,148] the model suggests that current density in the initial linear feature is

still primarily dominated by electric field enhanced WD. Field-enhanced dissociation of the buffering anion does contribute slightly, but at most accounts for only 50% of the observed current density. Therefore, the model suggests that the use of 1 M $KHCO_3$ buffer electrolyte forces an early onset of the electric-field-enhanced water dissociation reaction. The experimentally supported simulations hence clarify that the accelerated current onset for $KHCO_3$-exchanged BPMs is largely due to a reduction in the rate of interfacial recombination due to reaction of WD generated OH^- with HCO_3^- to form CO_3^{2-} *via* what is essentially an indirect HCO_3^- dissociation pathway (water dissociation followed by bicarbonate to carbonate interconversion). In turn, clarifying that the eventual increase of the seawater current density beyond the $KHCO_3$ current densities is due to the seawater BPM possessing a larger electric field at a given membrane potential.

Importantly, the model enables spatial resolution of *in situ* CO_2 regeneration, which is shown to occur only at the interface between the CEL and catholyte, as the concentration of (bi)carbonates is too small within the CEL itself (due to Donnan exclusion) to facilitate reaction with WD generated H^+. Therefore, at the surface of the CEL, H^+ from WD reacts with HCO_3^- in the electrolyte to form CO_2. The CO_2 solubility limit is eventually reached in the catholyte at the surface for the CEL, leading to the formation of bubbles. This process was clearly visualized experimentally when the BPMs were tested in (bi)carbonates in the custom electrolysis cell (**Figure 6.4**) and has also been reported in prior studies of BPMs operated in $KHCO_3$ solutions.[149,150]

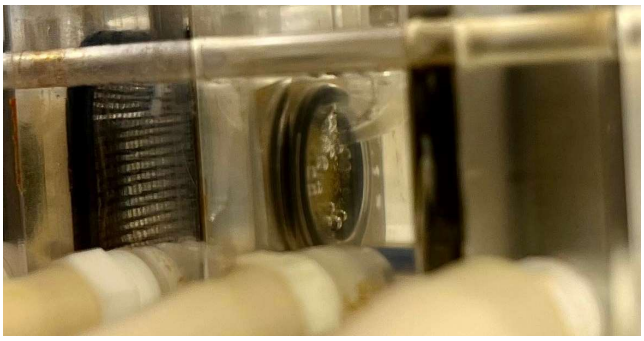

Figure 6.4 Image of bubbles forming at the surface of the CEL of a Fumasep BPM with applied current.

On the AEL side of the BPM, pH increases do not occur as readily with increasing cell potential because the AEL is fully (bi)carbonate exchanged at equilibrium and the presence of (bi)carbonates in high concentrations buffers against changes in pH and pOH. However, past potentials of 0.5 V, the pH does increase within the AEL, and the concentration of dissolved CO_2 decreases significantly due to equilibrium reactions with WD generated OH^-. At the same time, HCO_3^- is consumed to form CO_3^{2-} in accordance with equilibrium, decreasing the concentration of HCO_3^- in the AEL and increasing that of CO_3^{2-}, at high potential. Once essentially all the HCO_3^- in the AEL has been consumed ($V > 0.7$ V), the pH in the AEL increases much more rapidly, and the generated OH^- can escape the BPM and react with HCO_3^- anions in the anolyte. While the concentration of HCO_3^- in the AEL tends to zero at 1.0 V of applied potential, the concentration remains near the bulk concentration in the electrolyte, demonstrating that there is an abundance of reactive (bi)carbonate to consume WD generated OH^- anions.

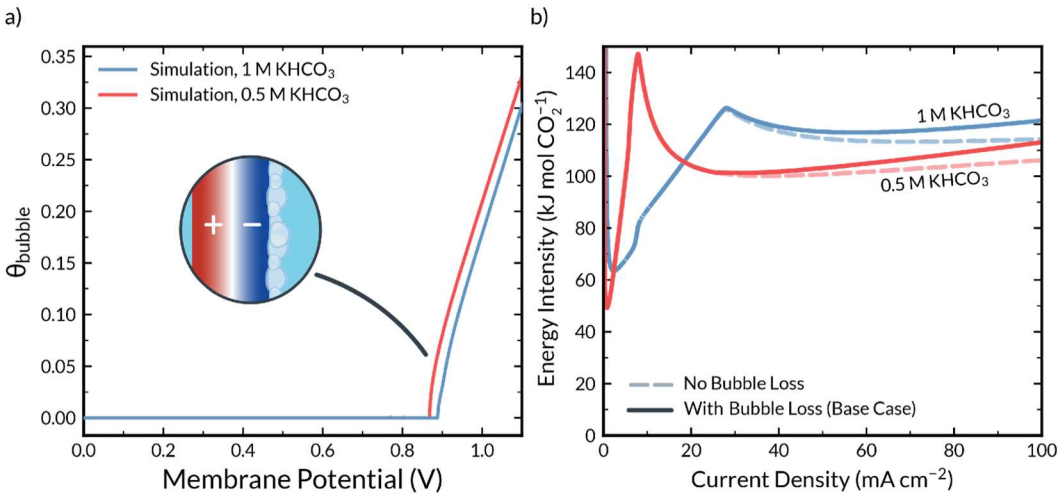

Figure 6.5 Effect of CO_2 bubble formation on energetic penalties in BPM-ED EMCC. (a) Simulated bubble coverage as a function of applied membrane potential. (b) Simulated energy intensity of a BPM with no bubble management (solid lines) and perfect bubble management (dashed lines).

When developing practical electrochemical devices, management of bubbles is a critical element to consider.[151–153] This is especially true for carbon capture devices that must account for generation of CO_2 gas from an aqueous (bi)carbonate electrolyte. The model presented herein enables a simulation of the bubble coverage on the CEL, as well as an understanding of how the bubble coverage affects the energy requirements for BPM-ED EMCC. Analysis of the bubble coverage in these simulations shows that the bubble coverage of the BPM exceeds 30% at high applied potentials and current densities due to super saturation of the electrolyte (**Figure 6.5a**). This high bubble coverage is consistent with visual observation of the CEL during operation. Additionally, the analysis of the energy requirements with and without losses due to bubble coverage reveals that bubble effects account for nearly 10 kJ mol^{-1} of energy loss (**Figure 6.5b**) for both 1 M $KHCO_3$ and 0.5 M $KHCO_3$ at

100 mA cm^{-2}. Therefore, managing bubbles is indeed crucial to improving energy efficiencies for BPM-ED EMCC.

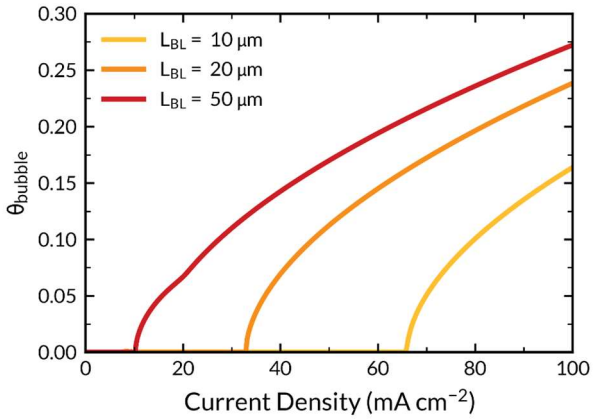

Figure 6.6 Effect of boundary layer thickness on the simulated bubble coverage on the CEL.

Previous knowledge from water electrolysis shows that bubble coverage losses can be reduced by controlling flow rate, increasing gas headspace pressure,[154] or employing a surfactant to reduce surface tension and bubble size.[155,156] The effect of flow rate can be represented in our model through the thickness of the anolyte and catholyte diffusion boundary layers (**Figure 6.6**). Lower flow rates are represented by thicker boundary layers, and higher flow rates are represented by thinner boundary layers.[157] The model shows that changing the flow rate has little effect on the polarization curve (i.e., the energetic requirements) or the overall rate of CO_2 efflux from the catholyte (**Figure 6.7**).

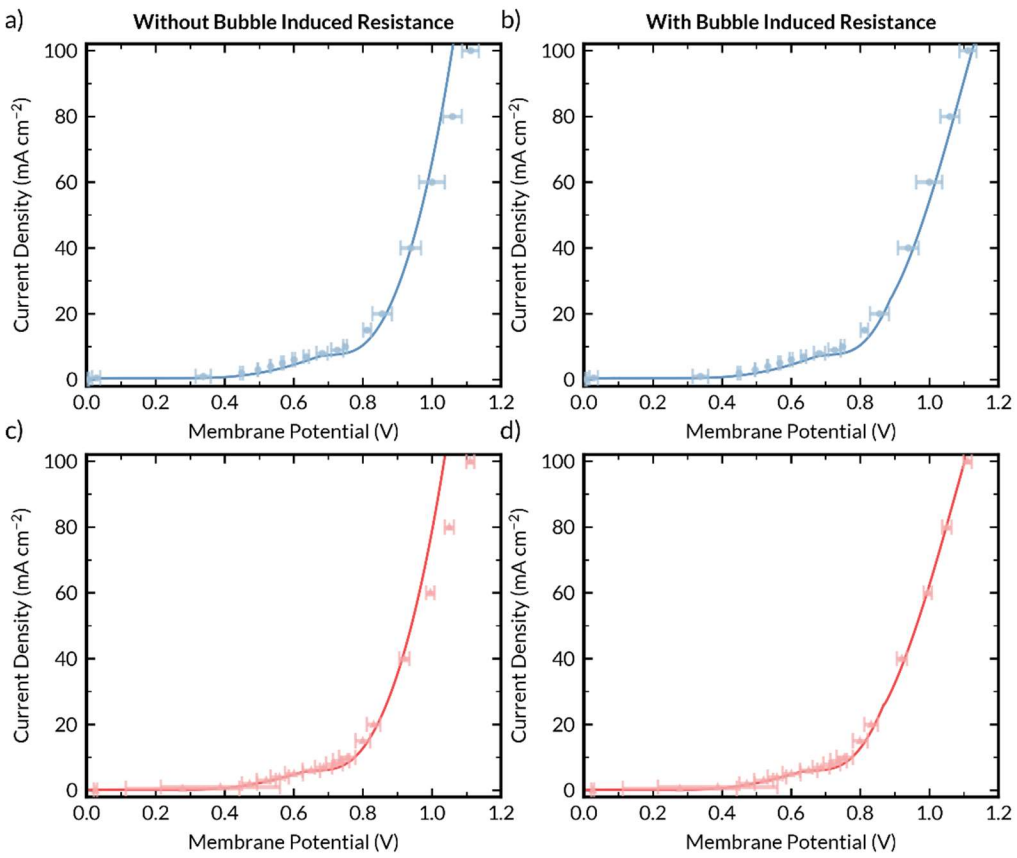

Figure 6.7 Impact of bubble induced resistances on BPM polarization curves for BPMs immersed in (a, b) 1 M $KHCO_3$ and (c, d) 0.5 M $KHCO_3$.

Increasing flow rate, however, does change the current density for which bubbling is observed. At the base case boundary layer thickness of 25 μm, (corresponding to a Reynolds number (Re) of 18,000, which is in the laminar flow regime over a smooth flat plate[158]), bubbling occurs at a current density of approximately 20 mA cm^{-2}, consistent with experiment. However, for a boundary layer thickness of 10 μm, (corresponding to Re of 111,000, still in the laminar flow regime for a flat plate [158]), bubbling does not occur until 60 mA cm^{-2}. The delay on the onset of bubbling occurs because the higher Re accounts for faster transport of CO_2 away from the reactive CEL/electrolyte boundary, preventing supersaturation

and keeping CO_2 dissolved within the aqueous electrolyte. Therefore, flow-rate management could be key to mitigating losses due to bubble coverage.

Further experiments were also performed (using the custom electrolysis cell) to understand the effect of flow rate, through the acid and base chambers, on the amount of bubbling that occurs at the surface of the CEM. To measure the amount of bubbling, chronopotentiometry experiments were performed between 0 and 100 mA cm^{-2}, and the average and standard deviation of the measured voltage was calculated for the last 60 sec of each current step. Using this method, a larger standard deviation indicates more bubbling. **Figure 6.8a** compares standard deviation of voltage vs. current density for three different flow rates (0.2, 1, and 5 mL min^{-1}). This shows that the amount of bubbling increases much more quickly at slower flow rates than at faster flow rates, as predicted from the model. **Figures 6.8b-d** show voltage vs. time for the three different flow rates examined. The most noise due to the formation of bubbles can be seen for the slowest flow rate (0.2 mL min^{-1}, **Figure 6.8b**).

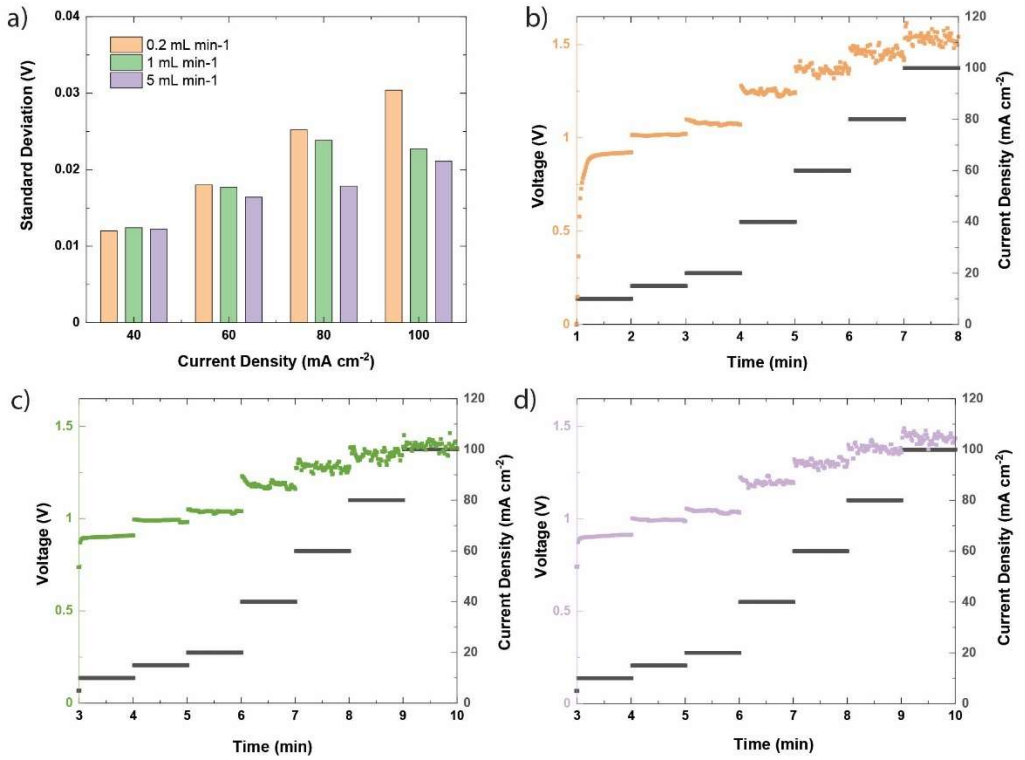

Figure 6.8 Experimental measurements of bubbling at CEL surface of Fumasep BPM with varying flow rate. (a) Comparison of the current density at which bubbling begins based on flow rate through the cell, via standard deviation of measured voltage. Voltage vs. time for current step measurements at (b) 0.2 mL min^{-2}, (c) 1 mA cm^{-2}, and (d) 5 mA cm^{-2}.

Figure 6.9a-b present polarization curves for Fumasep tested at each flow rate in 1 M $KHCO_3$ and 0.5 M NaCl, respectively. Comparing the two plots indicates that the addition of bicarbonate species into the electrolyte increases the average voltage measured at each current density. Furthermore, without the bicarbonate species present (**Figure 6.9b**), flow rate has no effect of the measured BPM voltage. However, in the presence of bicarbonate (**Figure 6.9a**), the average voltage is highest for the slowest flow rate, indicating that an increase in bubbles over the faster flow rates leads to decreased surface area and increased resistance. This experimental data

further supports the importance of flow rate and bubble mitigation on maintaining low cell voltages when using BPMs for carbon removal.

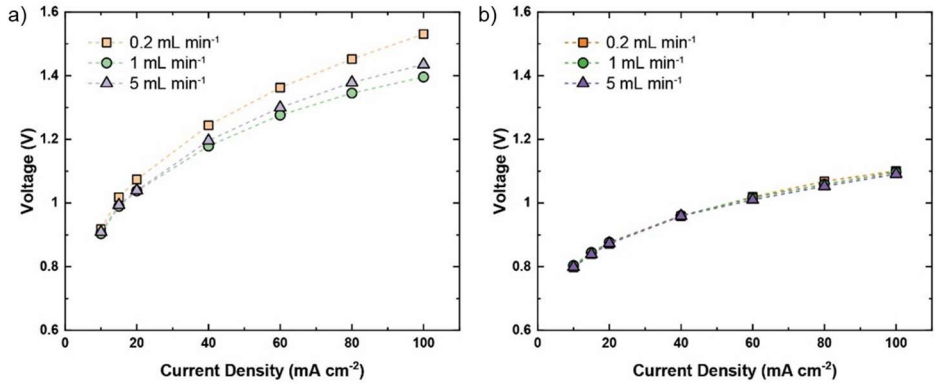

Figure 6.9 Polarization curves depicting average voltage vs. current density for Fumasep tested in (a) 1 M $KHCO_3$ and (b) 0.5 M NaCl.

6.3 Conclusion

Electrochemically mediated carbon capture strategies have the potential to displace thermal desorption techniques used in DAC because they operate with lower energy requirements at ambient temperatures and pressure. Bipolar membrane electrodialysis (BPM-ED) is a promising technique that uses H^+ and OH^- generated by electric field enhanced water dissociation (WD) in the BPM to simultaneously drive the release of CO_2 and the recovery of CO_3^{2-} from an electrolyte containing reactive carbon species. Unfortunately, the mechanisms, local environments, and energy losses in BPM-ED systems for carbon capture have been poorly understood, especially at the micron scale level within the BPM itself. Herein, simulations matched closely by experiment were developed and used to resolve the rates of the various kinetic and transport processes (field enhanced water or bicarbonate dissociation, homogeneous buffer reactions, salt crossover, etc.) occurring within

BPMs immersed in three reactive carbon solutions relevant to carbon capture: 1 M $KHCO_3$, 0.5 M $KHCO_3$, and simulated seawater. Simulations reveal that an early onset in observed current density for (bi)carbonate exchanged BPMs is due to field enhanced dissociation of the bicarbonate anions as well as a reduction in H^+/OH^- recombination due to competitive reaction of OH^- with HCO_3^- to form CO_3^{2-} indirectly.

Furthermore, analysis of energetics and bubble coverage effects reveal that one of the greatest opportunities for optimization of these systems are through the management of bubbles. This is supported through experimental observation and analysis of the onset of bubbling vs. current density at multiple flow rates. The experimental work indicated that faster flow rates can in fact delay to onset of bubbling, allowing for operation at higher current densities without resistance losses from bubbles. Ultimately, this work provides substantial insight into the mechanistic behavior of reactive carbon species in BPM systems, relevant to many electrochemical carbon capture and conversion technologies, and elucidates the promise of BPMs in performing BPM-ED for carbon capture at current densities exceeding 100 mA cm^{-2}.

6.4 Materials and Methods

Chemicals: All chemicals were used as purchased. Sodium hydroxide (NaOH, Macron Chemicals), sodium chloride (NaCl, VWR Chemicals), sodium bicarbonate ($NaHCO_3$, ≥99.5%, Sigma-Aldrich), potassium bicarbonate ($KHCO_3$, 99.7-100.5%, J. T. Baker), and potassium carbonate (K_2CO_3, 99.997%, Thermo Scientific). Simulated seawater in this work consists of 0.5 M NaCl with 0.00211 M $NaHCO_3$.

Electrodialysis Cell: Experimental current density-voltage measurements were obtained using a house-made five-chamber electrodialysis cell with Luggin capillaries. The cell was constructed, as depicted in **Figure S1,** using a Ni foil (VWR) anode and cathode, Nafion N324 CEMs (FuelCellStore), Fumasep FAB-PK-130 AEM (Fuelcellstore), and Fumasep FBM-PK BPM (Fuelcellstore). The active area of the BPM in this specific cell was 1 cm^2. Copper tape was used as leads for the Ni electrodes and Ag/AgCl (CH instruments, CHI111P) reference electrodes were placed in custom made glass Luggin capillaries on either side of the BPM.

Electrochemical measurements: Once the electrodialysis cell was assembled, a peristaltic pump (Ismatec ISM4408) was used to flow 1 M NaOH (10 mL min^{-1}) through the outer chambers, 3 M NaCl (10 mL/min) through the dilute chamber (chamber between CEM and AEM), and the relevant bicarbonate, carbonate, or simulated seawater solution (0.2 mL/min) through the chambers on either side of the BPM. These flowrates remained constant through all measurements. Once all chambers were filled, leads from a SP-300 BioLogic potentiostat were connected to the cathode, anode, and reference electrodes in a four-point measurement configuration. Current density-voltage measurements were then obtained by applying a chosen current across the cathode and anode and measuring the voltage between the two Ag/AgCl reference electrodes. Measurements were started at 0.1 mA cm^{-2} and increased stepwise through each current density to 100 mA cm^{-2} (EC-lab® software). Each current step was held constant for 20 minutes to obtain a steady-state voltage. The final voltage collected at each current step was reported in the current density-voltage plots, apart from some of the higher current density steps.

During the 1 M $KHCO_3$ and 0.5 M $KHCO_3$ experiments, CO_2 bubbles formed at the surface of the electrode at higher current densities ($\geq$ 20 mA/cm^{-2}) causing a significant amount of noise in the data. For these measurements, the voltage reported was taken as the average over the current step.

Experimental bubble measurements: Commercial Fumasep BPMs were used for all experiments. All tests were performed in our custom electrodialysis flow cell, flowing 1 M $KHCO_3$ (unless otherwise stated). Stirring in the acid and base chambers for implemented at for all experiments to minimize mass transport effects other than flow. Chronopotentiometry measurements were stepped from 0 to 100 mA cm^{-2}, holding for 2 min at each current and measuring the resulting voltage across the BPM. Average and standard deviation of the voltage at each current step with the calculated for the final 60 seconds of each step. The standard deviation of the voltage was then used as a metric to determine the amount of bubbling at each current.

Chapter 7: Summary and Outlook

This thesis presents a range of work focused on developing and implementing bipolar membranes (BPMs) for direct ocean capture (DOC) of carbon, direct air capture (DAC) of carbon, and energy storage. The main BPM presented in this text was successfully designed to overcome water transport limitations that currently exist in commercial BPMs and prevent stable high current density operation. The novel BPM was also engineered to maximize membrane and catalyst adhesion, while minimizing resistive voltage losses and membrane degradation. The high current density BPM (HCD-BPM) consists of a simple combination of a Nafion CEL, PiperION AEL, and GrOx catalyst and has achieved record breaking performance (~1.1 V @ 1 A cm^{-2}), H^+ and OH^- efficiency (> 90% above 100 mA cm^{-2}), and stability (>1000 hour at 80 mA cm^{-2}, >100 hours at 500 mA cm^{-2}, and >60 hours at 1 A cm^{-2}). The HCD-BPM was also successfully scaled 6-fold and implementation into a multi-cell electrodialysis stack designed for integration into a DOC system. Furthermore, forward bias testing of the HCD-BPM indicated its excellent potential for implementation into an acid/base flow battery. Finally, due to its simple structure, the HDC-BPM was an ideal candidate for fundamental studies probing the experimentally elusive inner workings of a BPM. Specifically, the membrane was employed to successfully examine the structure of the CEL/AEL junction, in-situ pH with applied current, and mechanisms of water transport.

Although significant performance improvements and fundamental insights have been achieved, challenges still reaming for which the HCD-BPM is well equipped to address. The main challenges necessary to overcome for

industrial/commercial implementation of the HCD-BPM are: i) increased stability, ii) stronger junction adhesion, and iii) fabrication modification for ease of scaling.

Although over 1000 h of continuous stability was achieved at 80 mA cm-2, similar thousand or multi thousand-hour measurement for high current density operation (> 200 mA cm^{-2}) are a prerequisite to commercial implementation. The HCD-BPM does not suffer from water transport limitations (as current commercial BPMs do), however, an independent high current density challenge of membrane over heating presented itself in this work. Therefore, to accomplish the goal of > 1000 hours of stability at high current densities, implementation of system temperature controls or use/development of high temperature resistant membrane will be necessary.

The second challenge of improved BPM junction adhesion has proven critical to overcome for scaled operation of the HCD-BPM. For small area (1 cm^2) tests, electrostatic interactions between the CEL and AEL proved strong enough to prevent delamination. Once scaled to an active area of 6 cm^2, however, membrane warping, wrinkling, and delamination was observed after BPMs were removed from the testing cell. Reduces mechanical stability due to a larger free standing BPM active area and high flow rates typically used in BPM-ED cell stacks are the most likely culprits causing the observed BPM deformation. Addition of a chemical adhesive layer at the BPM junction should be implemented to improve mechanical stability, however, the benefits from this improved adhesion will need to be weighed against resistive voltage losses that will inevitably occur.

To overcome the third challenge of BPM development, fabrication methods will need to be modified in order to make larger area membranes, which will be necessary for commercial applications. Specifically, the methods used for fabrication of the 1 and 6 cm^2 active area BPMs employed the technique of spin coating for catalyst deposition, which is not conducive to scaling. Ideally, nearly identical BPMs can be fabricated through casting of the CEL and AEL and either casting or spray coating of the catalyst layer. These techniques are much more suited to scaling and eventual roll to roll processing for commercial production.

The HCD-BPMs will also be useful for future studies of BPM fundamentals. There is still significant space for experimental and in-situ studies of pH in an around a BPM. Initial work using confocal microscopy with fluorescent pH sensitive dyes allowed for three-dimensional visualization of the HCD-BPM structure as well as measurement and visualization of the change in pH with applied current just a few μm from the surface of the BPM. Visualization changes in pH with applied current within the BPM layers proved challenging because the BPMs shifted on the order of 100 μm when current was applied. With improved cell design including added mechanical support for the BPM, however, the pH within the BPM could be directly visualized opening a door to many fundamental insights.

Finally, as presented for the forward bias studies in chapter 5, the HCD-BPM may be used for further investigation of water transport mechanisms. The work in chapter 5 specifically explored water transport in forward bias operations. These same measurements, employing isotope labeling of water, can be implemented in reverse bias experiments. With this direct insight into water transport, failure

mechanisms theorized to be due to water transport limitations could be experimentally proven, granting insight into how to overcome this cause of membrane failure.

Appendix 1: Nanoporous Copper as a Catalyst for CO_2 Reduction

Note: This section of the thesis presents work accomplished in the first two year of my PhD, prior to taking a year leave of absence. When I returned to Caltech, I did not continue directly working on this project, however, I have worked with and advised other graduate students in the group who are continuing this effort.

A1.1 Introduction

With the growing threat of climate change, as discussed in **Chapter 1**, it is becoming increasingly important to reduce the amount of anthropogenic CO_2 released into the atmosphere.[6–8] One technology that can help to mitigate atmospheric CO_2 levels is electrochemical CO_2 reduction to fuels.[159,160] This technology utilizes CO_2 removed from the atmosphere via DAC or DOC, electrochemically converting it to commodity chemical and fuels and creating a closed loop cycle for CO_2 removal and use.[159,161–163] A significant quantity of work has been published on materials catalysts for CO_2 reduction, all focused on overcoming two main challenges: selectivity and efficiency.[70,159,160,164–166] When performing electrochemical reduction on CO_2, there are many possible products that can form, therefore, it is critical to develop catalyst materials that are selective for one specific product.[167–169] Furthermore, with regards to catalyst material design, it is essential to improve the efficiency at which products are formed, in turn reducing the energy input necessary to drive reduction reactions.[111,167,170]

Previous work has revealed Cu as a highly active catalyst capable of efficient CO_2 conversion to a wide range of products.[171–176] In addition, it is widely understood

that high surface area catalysts lead to an increase in energy efficiency.[111,165,171,177] In this chapter, fabrication, material characterization, and electrochemical testing of high surface area nanoporous copper (np-Cu)[178–182] electrodes for CO_2 reduction is reported. Procedures for depositing a copper/aluminum alloy and subsequently etching away the aluminum are perfected as a repeatable method for fabrication of np-Cu (**Figure A1.1**). The np-Cu electrodes are then electrochemically tested and shown to be more selective than planar Cu electrodes for CO_2 reduction to ethylene (C_2H_4) over carbon monoxide (CO) and hydrogen (H_2).

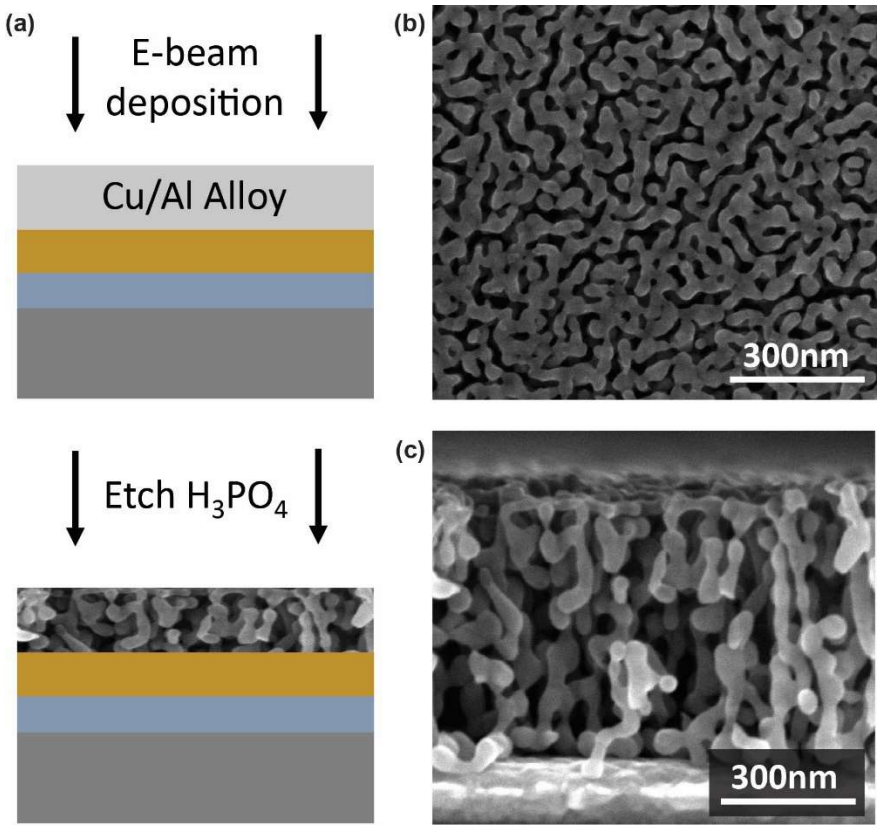

Figure A1.1 (a) Deposition and etching for fabrication of NP Cu. (b) and (c) SEM images of top view and cross- section of NP Cu, respectively.

A1.2 Results and Discussion

In this work, np-Cu was fabricated for use as an efficient and selective CO_2 reduction catalyst. An ideal and repeatable np-Cu fabrication technique was achieved through deposition of a Cu/Al alloy and subsequent etching with H_3PO_4, the results of which are shown with SEM images in **Figure A1.1b-c**. The etched np-Cu samples were then electrochemically tested to measure current efficiency and product selectivity. A compression flow cell was utilized for electrochemical tests, as descried in **Section A1.4**. The amount of each resulting product was measured with a gas chromatographer and used to calculate Faradaic efficiency (FE) and partial current density for each product detected. FE for e-beam deposited planar Cu (10nm Ti, 200nm Cu) and np-Cu (10nm Ti, 200nm Cu, 25onm np-Cu) at 3 different potentials (-0.9, -1.1, -1.3 V vs. RHE) were compared (**Figure A1.2**), revealing that FE for ethylene is significantly increased for np-Cu electrodes over planar electrodes, with a max FE for ethylene of ~35% at -1.1V vs. RHE. Examining the partial current densities of each product (**Figure A1.2c-d**), it is seen that H_2 from the competing water electrolysis half reaction is dominate product, with ethylene (C_2H_4) in second place. The production of H_2, however, is significantly reduced for np-Cu over planar Cu.

This increased selectivity toward ethylene seen for the np-Cu is hypothesized to occur due to Cu's intermediate binding energy for CO, as well as the exposure of catalytically active grain boundaries and surface facets. An intermediate binding energy for CO indicates that CO will remain on the catalyst surface long enough for further reaction to occur, forming high carbon products, but not so long that the

competing water electrolysis reaction will dominate. The np-Cu catalyst presented here shows these qualities, however, future work to eliminate H_2 as a product will be essential to eliminate a need for subsequent product separation.

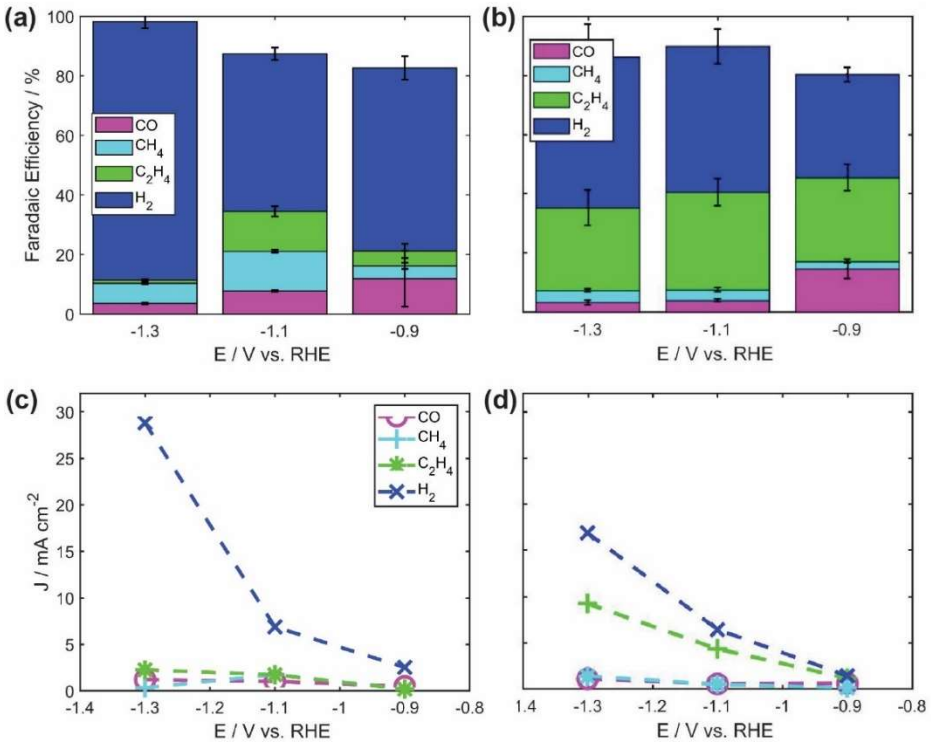

Figure A1.2 (a) and (b) are the Faradaic Efficiencies and (c) and (d) are the current densities of CO, CH4, C2H4, and H2 at three different potentials (-1.3, -1.1, -0.9 V vs. RHE) for planar Cu (10nm Ti and 200nm Cu on glass) and NP Cu (10nm Ti, 200nm Cu, and 250nm NP Cu on glass), respectively.

Beyond the electrochemical measurements already discussed, further structural development of the np-Cu catalysts was explored. First, multiple tunable parameters were considered to alter the morphology of the electrodes: ligament size, sample porosity, and total thickness. Ligament size and porosity were seen to simultaneously shift depending on the ratio of Cu to Al in the initial deposited alloy

(**Figure A1.3**). The thinnest and most porous ligament structure is observed for samples prepared with 15 vol% of Cu in the original alloy. Samples etched from 20 vol% Cu have an intermediate ligament size and porosity and those made from 25 vol% Cu show the largest and most dense ligament distribution. Further electrochemical experiments are necessary to determine if this variation in ligament size and porosity influences product distribution and current efficiency.

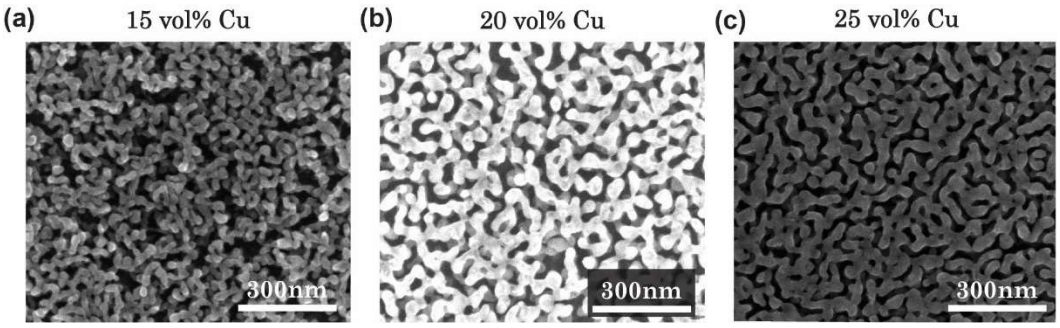

Figure A1.3 SEM images of NP Cu etched from 25 vol%, 20 vol%, and 15 vol% Cu/Al Alloy, respectively.

Another parameter investigated was the thickness of the np-Cu electrodes. The final thickness was modulated by simply changing the thickness of Cu/Al alloy initially deposited. Fully etched np-Cu samples were produced from a 1000 μm thick Cu/Al alloy (**Figure A1.4**) indicating that the thickness of these catalysts can in fact be modified. These thick samples, however, show voids not seen in the thinner samples prepared from 500 μm thick alloys. Future electrochemical characterization is necessary to understand how the change in thickness and presence of voids may shift current efficiency and product distribution.

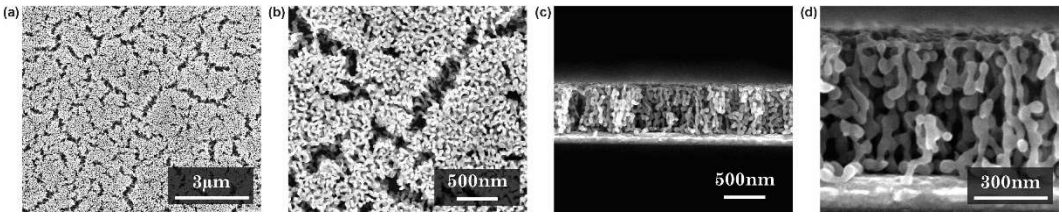

Figure A1.4 SEM images for visualization of 1 um thick NP Cu sample. (a) and (b) show trenches in top-down visualization. (c) and (d) uniformity of NP Cu through cross section of sample.

A1.3 Conclusion and Outlook

In this section, np-Cu electrodes fabricated using electron beam co-deposition of a copper/aluminum (Cu/Al) alloy are presented. These nanoporous structures are preferable to planar Cu because they have a higher electrochemical surface area and contain an increased quantity of high index facets, which lead to selectivity toward desirable high carbon products. When electrochemical testing and product analysis were conducted, the np-Cu samples are shown to increase the selectivity of CO_2 reduction towards ethylene (to > 35%), when compared to products made by planar Cu electrode. Although this result is promising, more work needs to be done to suppress the hydrogen evolution reaction and improve current efficiencies. Initial work varying membrane morphology was also presented, however, electrochemical testing and product analysis is still necessary for evaluation of these structures.

One method that has been previously investigated in planar Cu systems for improved product selectivity is the addition of gold nanoparticle, forming new catalytically active grain boundaries between the gold and the copper.[183] A similar deposition technique was used to deposit Au nanoparticles on the surface of np-Cu samples. The fabrication was successful, as seen in **Figure A1.5**, however, as with

the varied morphologies described previously, electrochemical testing and product analysis remains necessary to determine performance for selective CO_2 reduction.

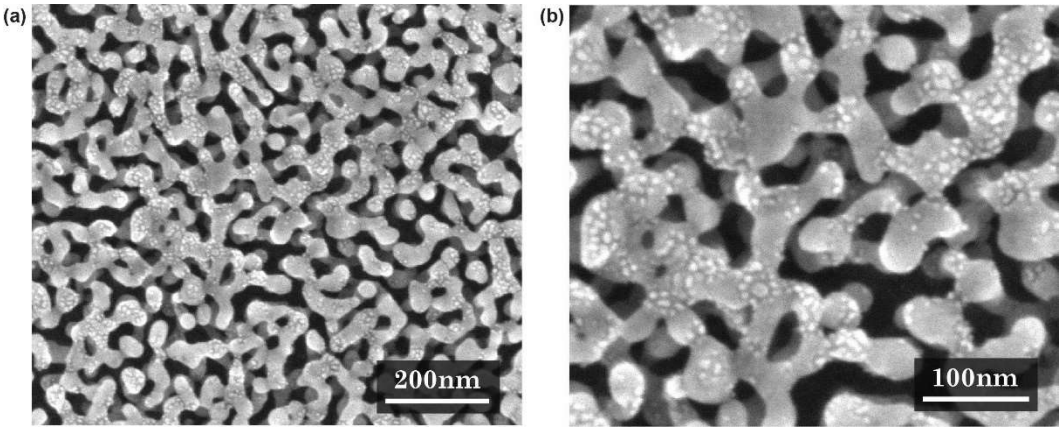

Figure A1.5 SEM images of NP Cu coated with gold nano particles deposited using e-beam evaporation.

Lastly, a promising method for suppression of water electrolysis is the implementation of gas diffusion electrodes (GDE), porous electrodes that allow for pure CO_2 flow across one side and electrolyte flow across the other.[105,106,184] GDEs have been previously employed in electrochemical CO_2 reduction systems and can drastically improve current efficiencies because of the significantly higher concentration of CO_2 present as well as suppress H_2 evolution by limiting the amount of aqueous electrolyte present at reaction sites.[184–186] The built in porosity of the np-Cu catalysts make them an ideal candidate for use in a GDE. Initial fabrication of np-Cu GDEs by deposition and etching Cu/Al alloys on a porous carbon substrate was successfully (**Figure A1.6**). Future work should be done to implement these np-Cu GDEs into electrochemical cells to evaluate performance and product distribution.

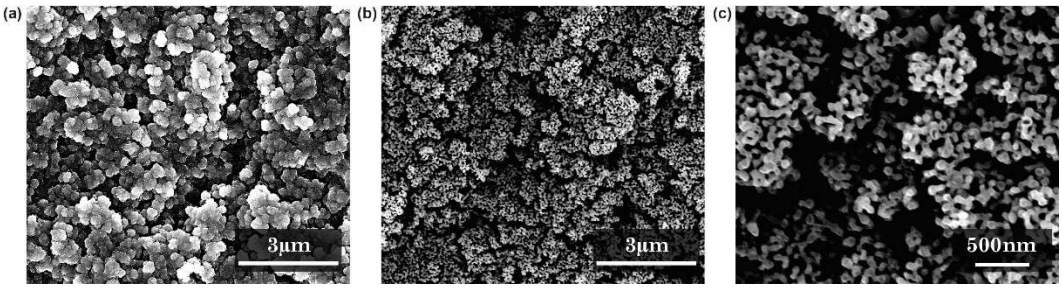

Figure A1.6 SEM images of (a) carbon paper and (b), (c) NP Cu coated carbon paper.

A1.4 Materials and Methods

Materials: Potassium carbonate (99.995%, Sigma Aldrich), Nitric Acid (18 M EMD Millipore Corporation), Si [p-type, 0-10 Ω cm, (100) orientation, 620 ± 25 µm thick, University Wafers], Pt foil (99.99% , 0.05 mm thick, Alfa Aesar), and Phosphoric Acid (85%, Fisher Chemical) were used without modification unless otherwise noted. The materials for electron beam deposition materials were ordered from Plasmaterials. The materials used were, Cu (99.9999%, 9 mm and down random size pieces), Al (99.99%, 0.250" Dia x 0.250 Long Pellets), and Cr (99.95%, 1-3mm Random Size Pieces). All water used for experiments was deionized and filtered through a 0.22 µm Millipak Express 40, serial number 0826.

E-beam deposition: The e-beam deposition system (System 02520, Angstrom Engineering) was used to deposit material onto Si substrates. First, 10nm of Cr was deposited as an adhesion layer. Second, 200nm of Cu was deposited to fully cover the Cr. Finally, 250-1000nm of Cu and Al was co-deposited. Calculation for the ratio of Cu to Al are shown in a sperate document. Samples were made with 25, 20, and 15 vol% Cu. The deposition rates and thicknesses for the Cu/Al co-deposition are calculated in "E-beam deposition rates" excel document.

Etching of alloy: After deposition, samples were etched in 5M H_3PO_4. Samples were etched for 30 min – 1 hour and removed from H_3PO_4 when samples became visually darker. After etching was complete, samples were rinsed with deionized water and dried with N_2.

SEM: A Nova200 Nanolab Dualbeam FIB/SEM with an acceleration voltage of 15 keV and spot size of 3 was used to image the structure of the fabricated samples. Cross section images were taken by breaking the samples and rotating them 90° when placed in the SEM.

Electrochemical Experiments: A two compartment, three electrode, compression cell made of polyether ether ketone (PEEK) was used to perform all electrochemical experiments. Construction of this cell is well known by multiple other people in the group. The electrolyte used for all tests is 50 mM K_2CO_3. The membrane used to separate the compartments is and anion exchange membrane (Selemion AMV). The np-Cu is the working electrode, Pt foil is used as the counter electrode and the reference electrode was Ag/AgCl. In between uses, the cell components made of PEEK were soaked in 10 wt% HNO_3. Before use, the components were rinsed in deionized water and then sonicated in deionized water for 10 min. This process was repeated four times to ensure full removal of HNO_3. The Pt foil was also cleaned in HNO_2 before use and then rinsed and flame annealed by holding a flame to the foil until it glows red then rinsing the foil in water and drying. The flame anneal process is repeated twice. The 50 mM K_2CO_3 electrolyte was saturated with CO_2 by bubbling CO_2 (Research grade from Airgas) into the electrolyte for 30 min prior to experiments. Each electrolyte compartment was bubbled with CO_2 at a rate of 5

SCCM. The outflowing gas was sent through a flow meter to check that the flow of CO_2 in and out of the cell was equal. The outflowing gas was sent through a vapor trap to remove all water from the air before it was fed into a gas chromatograph (GC) (SRI-8610). All experiments were performed at room temperature using a potentiostat (Biologic VSP300). Before each experiment, potentiostatic electrochemical impedance spectroscopy (PEIS) was performed to determine the solution resistance of the cell. The applied electrochemical potential was then compensated by 85% using iR compensation of the potentiostat.

Product Analysis: As explained above, all gas products were fed into a GC. Chronoamperometry was used to hold the working electrode at a set potential for 2 hours. During this time, the GC collected product information every 15 minutes. Quantitative analysis of gaseous products was based on calibration with several gas standards over many orders of magnitude in concentration. Between different potential experiments all the electrolyte was removed and stored for liquid product analysis. The cell was then rinsed three times with water before new electrolyte was add and bubbled with CO_2.

Data Analysis: The Matlab files used to analyze and plot all electrochemical and GC data are included in the np-Cu Paper folder along with this document.

Appendix 2: Lessons Learned

This section of the thesis describes best practices and lessons learned during my PhD experience and presents supporting figures and data.

A2.1 Material Selection and BPM Fabrication

Many configurations of CEL, AEL, and catalysts were considered when fist developing the BPM presented in this thesis. Some configurations were direct laminations between purchased CEL and AEL polymer sheets, while others started with polymer powder or ionomer and were cast into layers. Below is a list of all AEL and CEL combinations investigated while perfecting the HCD-BPM:

- Fumasep AEM + Nafion ionomer
- Fumasep AEM + Nafion ionomer (from powder)
- Sustainion AEM + Nafion ionomer
- Sustainion AEM + Nafion ionomer (from powder)
- Sustainion AEM + Nafion ionomer
- Sustainion AEM + Nafion ionomer (from powder)
- PiperION AEM + Nafion ionomer
- PiperION AEM + Nafion ionomer (from powder)
- Sustainion ionomer + Nafion CEM
- PiperION ionomer + Nafion CEM
- Sustainion AEM + Nafion CEM
- PiperION AEM + Nafion CEM

For membranes cast via spin coating, ultimate membrane layer thickness was determined by performing the membrane spin coating procedure on a Si substrate and measuring the thickness by scratching the deposited layer and scanning with a profilometer. The results of these measurements for several different membranes are reported in **Table A2.1**

Table A2.1 Measured membrane thickness on Si for Nafion D2020, Sustainion, PiperION A, PiperION B, and PiperION C after spin coating 1-4 layers at 3000 rpm for 30 sec.

Number of Coats	Nafion (20 wt%)	Sustainion (5 wt%)	PiperION A (5 wt%)	PiperION B (5 wt%)	PiperION C (5 wt%)
1	1.8 µm	0.25 µm	0.40 µm	0.55 µm	0.50 µm
2	3.3 µm	0.33 µm	1.7 µm	2.0 µm	1.0 µm
3	3.6 µm	0.35 µm	2.8 µm	2.6 µm	1.9 µm
4		0.38 µm	4.1 µm	5.3 µm	0.9 µm ?

During the fabrication procedure development process, the four main methods attempted were spin coating, hot pressing, casting, and sandwiching (**Figure A2.1**). Many of these trails led to warping, wrinkling, and cracking of the resulting BPM (**Figure A2.2**). While some fabrication trials resulted in immediately noticeable failure, others appeared successful and required electrochemical testing to evaluate performance. Numerous more layer combinations and lamination methods were eliminated when electrochemical characterization showed high voltages at low currents (**Figure A2.3**). The list below details the main observations made during the process of elimination for determining the best membrane combination and fabrication method.

1. All Sustainion membranes are incredible mechanically fragile and not capable of implementation into a full BPM layered structure.
2. Hot pressing the BPM after layering it only made its operational performance worse.

3. When depositing catalyst ink or binding layers to dry membrane surfaces, it is critical to simultaneously heat or wick off all water quickly (as in spin coating), otherwise the dry membrane will warp and wrinkle (sometimes permanently).

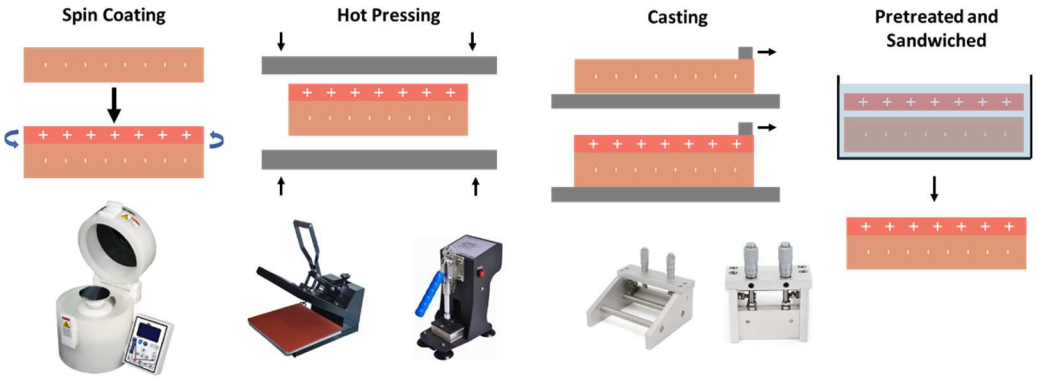

Figure A2.1 Diagrams of how each attempted BPM fabrication method (spin coating, hot pressing, casting, and sandwiching) was performed along with relevant laboratory tools.

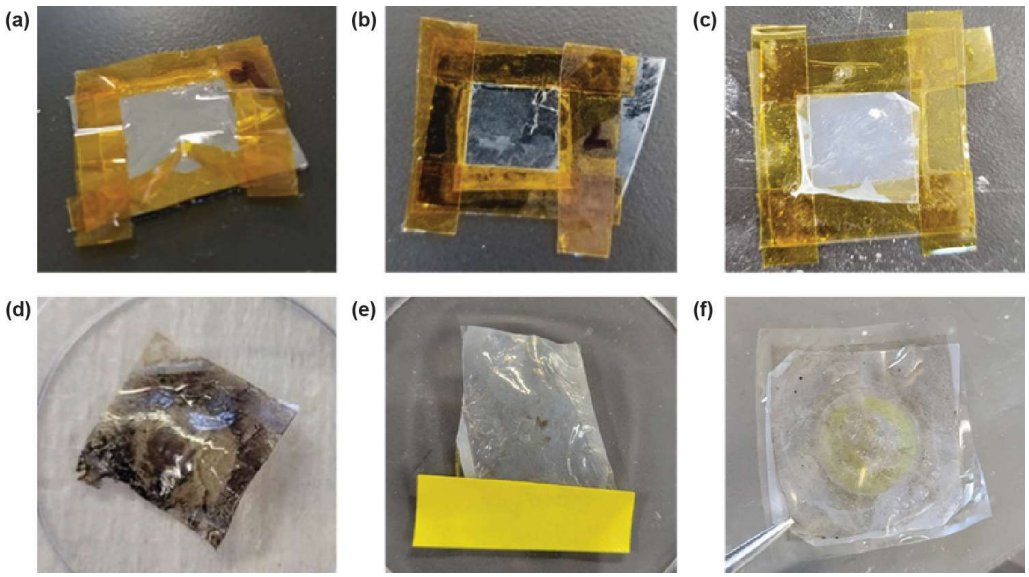

Figure A2.2 Images of BPM fabrication trials. (a) warping of base membrane sheet during catalyst depositions, (b) cracking of base membrane sheet during catalyst deposition, (c) wrinkling of AEM when using ionomer as a binder, (d) full BPM with 30 g/L GrOx paste in junction, (e) wrinkled BPM after testing, and (f) discolored BPM after testing.

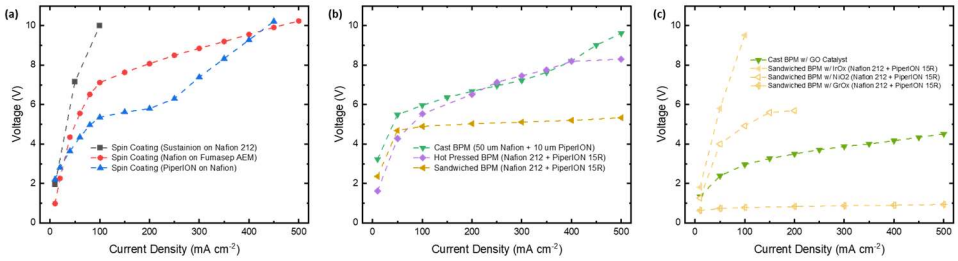

Figure A2.3 Polarization curves for (a) spin coated BPMs with varying CEL and AEL composition, (b) BPMs constructed from Nafion and PiperION comparing fabrication techniques, and (c) BPMs with varying catalyst materials.

Finally, a simple sandwiched lamination between a CEM sheet and an AEM sheet was determined to be ideal fabrication method. Detailed fabrication steps are reported below and shown in **Figure A2.4**.

1. Start with a clean glass slide.
2. Place pretreated Nafion on glass slide and dab dry with Kim wipe.
3. Tape all four sides being careful to keep the membrane flat without any air pockets between it and the glass slide.
4. Spin coat catalyst onto Nafion. Be sure to drop catalyst ink onto the Nafion after spinning has begun to prevent wetting and wrinkling of the membrane.
5. Place the catalyst coated Nafion in an oven at ~100°C and heat for ~2 min to fully dry catalyst ink.
6. Repeat steps for and 5 as many times as desired.
7. Store this Nafion and catalyst portion of the BPM in its dry form taped to the glass slide until ready to use.
8. Just before testing, use a razor blade to cut out Nafion just on the inside edge of the tape and rewet the membrane.
9. Gently place a wetted AEM on top of the catalyst coated Nafion.
10. Smooth out any bubbles gently, and test!

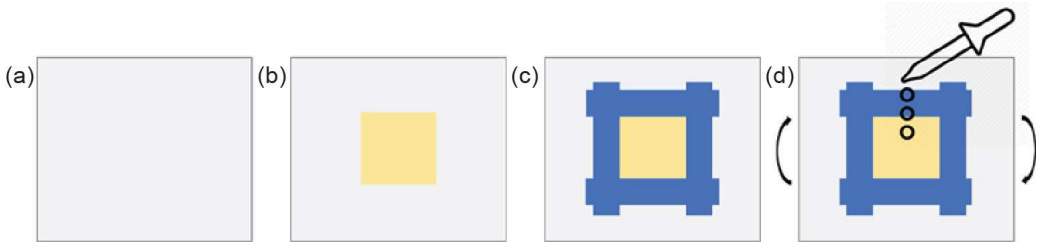

Figure A2.4 Diagram of method used for depositing a catalyst layer onto a membrane (CEM or AEM) sheet via spin coating. (a) start with a clean glass slide, (b) place pretreated and wetted CEM or AEM piece of desired size on the glass slide, then dab dry with a Kim wipe, (c) tape down all four sides of the membrane to the glass slide, and (d) drop on GrOx ink while spinning at 3000 rpm for 30 sec.

To perfect the above-described fabrication methods even further, several trials were performed using Nafion ionomer as a binder between the CEL and AEL as well as applying a heat treatment to the fully laminated BPMs. The list below details each of the BPMs fabricated in these trials. Polarization curves for most of these BPMs are given in **Figure A2.5**. The BPMs not seen in this figure became delaminated during the fabrication process. After these trials the process described in steps 1-10 above remained the ideal fabrication.

- Original – Sandwiched BPM with GO
- 2 – GROX baked, BPM baked, w/ ionomer glue
- 3 – GROX baked, BPM baked, w/o ionomer glue
- 4 – GROX baked, w/o ionomer glue
- 5 – GROX baked, w/ ionomer glue (dry)
- 6 – GROX baked, w/ ionomer glue (wetted)
- GROX baked – 100°C for 2 min
- BPM baked – 100°C for 90 min

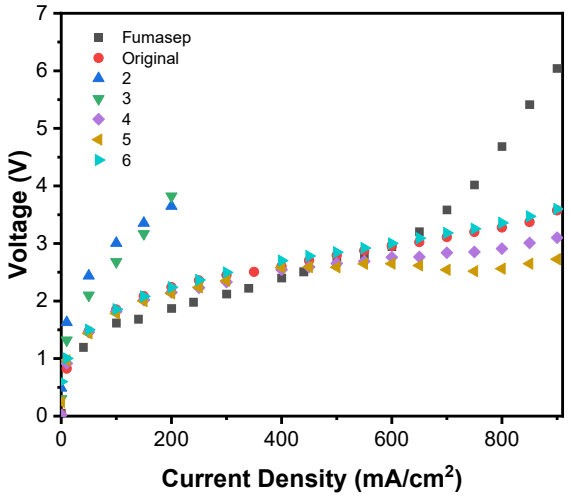

Figure A2.5 Polarization curves for BPM heat treatment trials.

One more set of fabrication trials was attempted, in which GrOx catalyst inks were made with Nafion and PiperION ionomers as binding agents. BPMs were then fabricated both Nafion and PiperION as the original membrane that catalyst was spin coated onto, and each original membrane condition was tested with both inks (**Figure A2.6**). It is noted that when Nafion was added to the catalyst ink, the GrOx remains well dispersed and suspended. However, when PiperION ionomer was added, the GrOx formed aggregates within the ink, making it impossible to deposit uniform coatings.

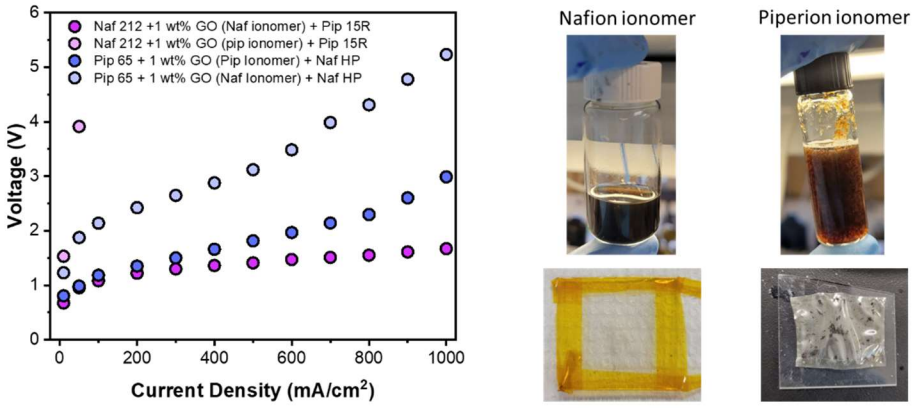

Figure A2.6 Polarization curves for BPMs fabrication trials with varying ionomer types in GrOx ink and images of the inks and samples.

A2.2 Material Characterization

Clear SEM cross sections of BPMs can be challenging to obtain due to sample charging because the polymers are not electronically conductive. It can also be challenging to create a clean cut for a smooth cross section. In Chapter 2, an SEM of the HCD-BPM is shown that was prepared by imbedding it in a reason and slicing it with a microtome. Before developing this technique, however, SEMs were taking on samples slices with a razor blade (**Figure A2.7**). Although these cross sections are rough, they clearly show an uneven GROX layer at the interface between the CEL and AEL. Further examination of microtome sliced BPMs should be used to understand the uniformity of catalyst layers.

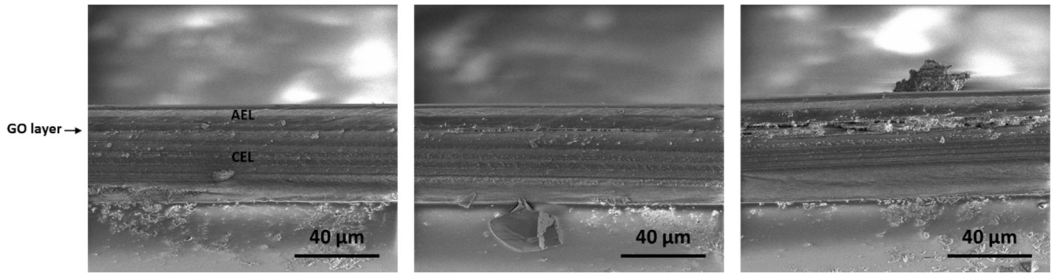

Figure A2.7 SEM cross section of BPMs constructed from Nafion 212, GrOx ink, and PiperION 15R.

Raman microscopy was also used to characterize the GrOx catalyst but was not reported in previous chapters because challenges with the instrument made it impossible to complete the characterization. Initial spectra, however, of GrOx before and after use as a catalyst in a BPM show the G (C-C stretching) and D (breathing mode of aromatic rings) bands expected for graphene oxide. The intensity of D band depends on number of defects and O atoms present in the GrOx sample. The ratio of the D band intensity to the G band intensity (I_D/I_G) is an indirect indication of the disorder in the material. When the spectra shown in Figure A2.9 were analyzed, the following ratios were calculated: Before $I_D/I_G = 0.94$ After $I_D/I_G = 1.47$. Increase of the ratio after testing may indicate an increase in disorder in the sample. A shift in both the D and G band peaks after testing suggests mechanical strain in the graphene oxide sample. To verify these results, however, more tests should be performed. Furthermore, Raman x-y scans of the GrOx deposited on Nafion before and after testing could be more insightful for determining possible degradation or shifts in the GrOx catalyst layer, especially after long term experiments.

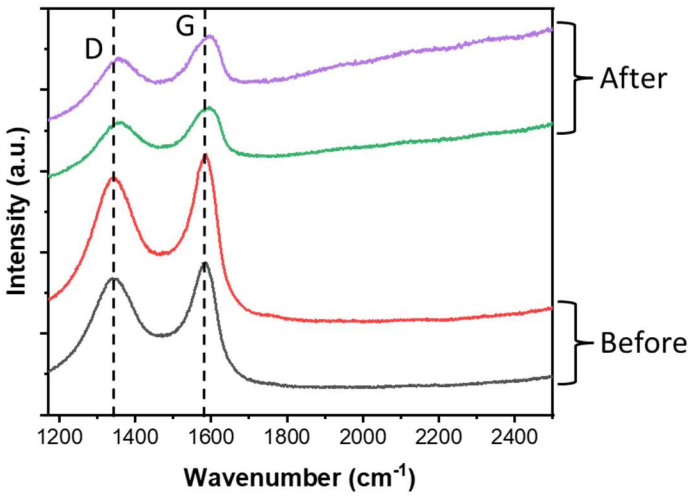

Figure A2.8 Raman spectra for GrOx catalyst layer on Nafion 212 before and after electrochemical testing.

References

1. Pärnamäe, R. *et al.* Bipolar membranes: a review on principles, latest developments, and applications. *J Memb Sci* **617**, 1–25 (2021).
2. Hoppe, C. J. M., Langer, G., Rokitta, S. D., Wolf-Gladrow, D. A. & Rost, B. Implications of observed inconsistencies in carbonate chemistry measurements for ocean acidification studies. *Biogeosciences* **9**, 2401–2405 (2012).
3. Understanding the science of ocean and coastal acidification | US EPA. https://www.epa.gov/ocean-acidification/understanding-science-ocean-and-coastal-acidification.
4. De Luna, P. *et al.* What would it take for renewably powered electrosynthesis to displace petrochemical processes? *Science (1979)* **364**, (2019).
5. United nations. *Paris agreement*. https://unfccc.int/sites/default/files/english_paris_agreement.pdf (2015).
6. Climate change 2022: mitigation of climate change. https://www.ipcc.ch/report/ar6/wg3/?itid=lk_inline_enhanced-template.
7. McKay, D. I. A. *et al.* Exceeding 1.5°C global warming could trigger multiple climate tipping points. *Science (1979)* **377**, (2022).
8. Rogelj, J. *et al.* Scenarios towards limiting global mean temperature increase below 1.5 °C. *Nature Climate Change 2018 8:4* **8**, 325–332 (2018).
9. Giesbrecht, P. K. & Freund, M. S. Recent advances in bipolar membrane design and applications. *Chemistry of Materials* **32**, 8060–8090 (2020).
10. Liu, Y., Lucas, É., Sullivan, I., Li, X. & Xiang, C. Challenges and opportunities in continuous flow processes for electrochemically mediated carbon capture. *iScience* **25**, 105153 (2022).
11. The emissions gap report 2017 : a UN environment synthesis report.
12. Xu, T. Ion exchange membranes: State of their development and perspective. *J Memb Sci* **263**, 1–29 (2005).
13. Ran, J. *et al.* Ion exchange membranes : New developments and applications. *J Memb Sci* **522**, 267–291 (2017).
14. Luo, T., Abdu, S. & Wessling, M. Selectivity of ion exchange membranes: a review. **555**, 429–454 (2018).
15. Frilette, V. J. Preparation and characterization of bipolar ion-exchange membranes. *Journal of Physical Chemistry* **60**, 435–439 (1956).
16. Mitchell, J. B., Chen, L., Langworthy, K., Fabrizio, K. & Boettcher, S. W. Catalytic proton-hydroxide recombination for forward-bias bipolar membranes. *ACS Energy Lett* **7**, 3967–3973 (2022).

17. Ramírez, P., Rapp, H. J., Mafé, S. & Bauer, B. Bipolar membranes under forward and reverse bias conditions. Theory vs. experiment. *Journal of Electroanalytical Chemistry* **375**, 101–108 (1994).

18. Al-Dhubhani, E., Pärnamäe, R., Post, J. W., Saakes, M. & Tedesco, M. Performance of five commercial bipolar membranes under forward and reverse bias conditions for acid-base flow battery applications. *J Memb Sci* **640**, 119748 (2021).

19. Kressman, T. R. E. & Tye, F. L. The effect of current density on the transport of ions through ion-selective membranes.

20. Simons, R. Strong electric field effects on proton transfer between membrane-bound amines and water. *Nature 1979 280:5725* **280**, 824–826 (1979).

21. Strathmann, H., Krol, J. J., Rapp, H. J. & Eigenberger, G. Limiting current density and water dissociation in bipolar membranes. *J Memb Sci* **125**, 123–142 (1997).

22. Chlanda, F. P. *et al.* United States Patent (19) Chlanda et al. 54 Bipolar membranes and method of making same.

23. Mani, K. N., Chlanda, F. P. & Byszewski, C. H. Aquatech membrane technology for recovery of acid/base values for salt streams. *Desalination* **68**, 149–166 (1988).

24. Emrén, A. T. & Holmström, V. J. M. Energy storage in a fuel cell with bipolar membranes burning acid and hydroxide. *Energy* **8**, 277–282 (1983).

25. Langie, K. M. G. *et al.* Toward economical application of carbon capture and utilization technology with near-zero carbon emission. *Nature Communications 2022 13:1* **13**, 1–10 (2022).

26. Erans, M. *et al.* Direct air capture: process technology, techno-economic and socio-political challenges. *This journal is Cite this: Energy Environ. Sci* **15**, 1360 (2022).

27. Sabatino, F., Gazzani, M., Gallucci, F. & Van Sint Annaland, M. Modeling, optimization, and techno-economic analysis of bipolar membrane electrodialysis for direct air capture processes. *Ind Eng Chem Res* **61**, 12668–12679 (2022).

28. Blommaert, M. A. *et al.* Insights and challenges for applying bipolar membranes in advanced electrochemical energy systems. *ACS Energy Lett* **6**, 2539–2548 (2021).

29. Mafé, S., Ramírez, P. & Alcaraz, A. Electric field-assisted proton transfer and water dissociation at the junction of a fixed-charge bipolar membrane. *Chem Phys Lett* **294**, 406–412 (1998).

30. Martinez, R. J. & Farrell, J. Quantifying electric field enhancement of water dissociation rates in bipolar membranes. *Ind Eng Chem Res* **58**, 782–789 (2019).

31. Bui, J. C., Digdaya, I., Xiang, C., Bell, A. T. & Weber, A. Z. Understanding multi-ion transport mechanisms in bipolar membranes. *ACS Appl Mater Interfaces* **12**, 52509–52526 (2020).

32. Bui, J. C., Corpus, K. R. M., Bell, A. T. & Weber, A. Z. On the nature of field-enhanced water dissociation in bipolar membranes. *Journal of Physical Chemistry C* **125**, 24974–24987 (2021).

33. McDonald, M. B., Freund, M. S. & Hammond, P. T. Catalytic, conductive bipolar membrane interfaces through layer-by-layer deposition for the design of membrane-integrated artificial photosynthesis systems. *ChemSusChem* **10**, 4599–4609 (2017).

34. Chen, L., Xu, Q., Oener, S. Z., Fabrizio, K. & Boettcher, S. W. Design principles for water dissociation catalysts in high-performance bipolar membranes. *Nature Communications 2022 13:1* **13**, 1–10 (2022).

35. Yan, Z. *et al.* The balance of electric field and interfacial catalysis in promoting water dissociation in bipolar membranes. *Energy Environ Sci* **11**, 2235–2245 (2018).

36. Ge, Z. *et al.* Beneficial use of a coordination complex as the junction catalyst in a bipolar membrane. *ACS Appl Energy Mater* **3**, 5765–5773 (2020).

37. Eswaraswamy, B., Suhag, A., Goel, P., Mandal, P. & Chattopadhyay, S. Potential of montmorillonite nanoclay as water dissociation catalyst at the interface of bipolar membrane. *Sep Purif Technol* **295**, 121257 (2022).

38. Eswaraswamy, B., Mandal, P., Goel, P. & Chattopadhyay, S. Potential of dipicolinic acid as a water-dissociating catalyst in a bipolar membrane. *Cite This: ACS Appl. Polym. Mater* **2021**, 6229 (2021).

39. McDonald, M. B. & Freund, M. S. Graphene oxide as a water dissociation catalyst in the bipolar membrane interfacial layer. *ACS Appl Mater Interfaces* **6**, 13790–13797 (2014).

40. Xue, Y., Wang, N., Huang, C., Cheng, Y. & Xu, T. Catalytic water dissociation at the intermediate layer of a bipolar membrane: The role of carboxylated Boltorn® H30. *J Memb Sci* **344**, 129–135 (2009).

41. Oener, S. Z., Foster, M. J. & Boettcher, S. W. Accelerating water dissociation in bipolar membranes and for electrocatalysis. *Science (1979)* **369**, 1099–1103 (2020).

42. Shen, C., Wycisk, R. & Pintauro, P. N. High performance electrospun bipolar membrane with a 3D junction. *Energy Environ Sci* **10**, 1435–1442 (2017).

43. Al-Dhubhani, E. *et al.* Entanglement-enhanced water dissociation in bipolar membranes with 3D electrospun junction and polymeric catalyst. *ACS Appl Energy Mater* **4**, 3724–3736 (2021).

44. Powers, D. *et al.* Freestanding bipolar membranes with an electrospun junction for high current density water splitting. *ACS Appl. Mater. Interfaces* **14**, 36092–36104 (2022).

45. Lucas, É., Han, L., Sullivan, I., Atwater, H. A. & Xiang, C. Measurement of ion transport properties in ion exchange membranes for photoelectrochemical water splitting. *Front Energy Res* **10**, 1383 (2022).

46. Wilhelm, F. G., Van Der Vegt, N. F. A., Strathmann, H. & Wessling, M. Comparison of bipolar membranes by means of chronopotentiometry. *J Memb Sci* **199**, 177–190 (2002).

47. Aritomi, T., van den Boomgaard, T. & Strathmann, H. Current-voltage curve of a bipolar membrane at high current density. *Desalination* **104**, 13–18 (1996).

48. Krol, J. J., Jansink, M., Wessling, M. & Strathmann, H. Behaviour of bipolar membranes at high current density water diffusion limitation. *Sep Purif Technol* **14**, 41–52 (1998).

49. Ozkan, M., Nayak, S. P., Ruiz, A. D. & Jiang, W. Current status and pillars of direct air capture technologies. *iScience* **25**, (2022).

50. Fasihi, M., Efimova, O. & Breyer, C. Techno-economic assessment of CO_2 direct air capture plants. *J Clean Prod* **224**, 957–980 (2019).

51. Sabatino, F. *et al.* Evaluation of a direct air capture process combining wet scrubbing and bipolar membrane electrodialysis. (2020) doi:10.1021/acs.iecr.9b05641.

52. Jayarathna, C., Maelum, M., Karunarathne, S., Andrenacci, S. & Haugen, H. A. Review on direct ocean capture (DOC) technologies. (2022).

53. Sharifian, R., Boer, L., Wagterveld, R. M. & Vermaas, D. A. Oceanic carbon capture through electrochemically induced in situ carbonate mineralization using bipolar membrane. *Chemical Engineering Journal* **438**, (2022).

54. Digdaya, I. A. *et al.* A direct coupled electrochemical system for capture and conversion of CO_2 from oceanwater. *Nat Commun* **11**, 1–10 (2020).

55. de Lannoy, C. F. *et al.* Indirect ocean capture of atmospheric CO_2: part I. Prototype of a negative emissions technology. *International Journal of Greenhouse Gas Control* **70**, 243–253 (2018).

56. Eisaman, M. D. *et al.* Indirect Ocean capture of atmospheric CO_2: Part II. Understanding the cost of negative emissions. *International Journal of Greenhouse Gas Control* **70**, 254–261 (2018).

57. Li, Y. C. *et al.* Electrolysis of CO_2 to syngas in bipolar membrane-based electrochemical cells. *ACS Energy Lett* **1**, 1149–1153 (2016).

58. Wrubel, J. A., Chen, Y., Ma, Z. & Deutsch, T. G. Modeling water electrolysis in bipolar membranes. *J Electrochem Soc* **167**, 114502 (2020).

59. Thiele, S. *et al.* Bipolar membrane electrode assemblies for water electrolysis. *ACS Appl Energy Mater* **3**, 9635–9644 (2020).

60. Ge, Z. *et al.* High-performance bipolar membrane for electrochemical water electrolysis. *J Memb Sci* **656**, (2022).

61. Mayerhöfer, B. *et al.* On the effect of anion exchange ionomer binders in bipolar electrode membrane interface water electrolysis. *J Mater Chem A Mater* **9**, 14285–14295 (2021).

62. Blommaert, M. A., Verdonk, J. A. H., Blommaert, H. C. B., Smith, W. A. & Vermaas, D. A. Reduced ion crossover in bipolar membrane electrolysis via increased current density, molecular size, and valence. *ACS Appl. Energy Mater* **2020**, 2022 (2020).

63. Wang, X. *et al.* Balancing water dissociation and current densities to enable sustainable hydrogen production with bipolar membranes in microbial electrolysis cells. *Environ. Sci. Technol* **53**, 14761–14768 (2019).

64. Yan, Z., Hitt, J. L., Zeng, Z., Hickner, M. A. & Mallouk, T. E. Improving the efficiency of CO_2 electrolysis by using a bipolar membrane with a weak-acid cation exchange layer. *Nat Chem* **13**, 33–40 (2021).

65. Pärnamäe, R. *et al.* The acid–base flow battery: sustainable energy storage via reversible water dissociation with bipolar membranes. *Membranes 2020, Vol. 10, Page 409* **10**, 409 (2020).

66. Metlay, A. S. *et al.* Three-chamber design for aqueous acid-base redox flow batteries. *ACS Energy Lett* **7**, 908–913 (2022).

67. Yan, Z. *et al.* High-voltage aqueous redox flow batteries enabled by catalyzed water dissociation and acid-base neutralization in bipolar membranes. *ACS Cent Sci* **7**, 1028–1035 (2021).

68. Weng, G. M., Li, C. Y. V. & Chan, K. Y. High-voltage pH differential vanadium-hydrogen flow battery. *Mater Today Energy* **10**, 126–131 (2018).

69. Thiele, S. *et al.* On the effect of anion exchange ionomer binders in bipolar electrode membrane interface water electrolysis on the effect of anion exchange ionomer binders in bipolar electrode membrane interface water electrolysis. **9**, 14105–14610.

70. Zhou, X. *et al.* Solar-driven reduction of 1 atm of CO_2 to formate at 10% energy-conversion efficiency by use of a TiO_2-protected III-V tandem photoanode in conjunction with a bipolar membrane and a Pd/C cathode. *ACS Energy Lett* **1**, 764–770 (2016).

71. Xu, J. *et al.* Review on electrochemical carbon dioxide capture and transformation with bipolar membranes. *Chinese Chemical Letters* 108075 (2022) doi:10.1016/j.cclet.2022.108075.

72. Jin, S., Wu, M., Jing, Y., Gordon, R. G. & Aziz, M. J. Low energy carbon capture via electrochemically induced pH swing with electrochemical rebalancing. doi:10.1038/s41467-022-29791-7.

73. Oener, S. Z., Twight, L. P., Lindquist, G. A. & Boettcher, S. W. Thin cation-exchange layers enable high-current-density bipolar membrane electrolyzers via improved water transport. *ACS Energy Lett* **6**, 1–8 (2021).

74. Vermaas, D. A., Wiegman, S., Nagaki, T. & Smith, W. A. Ion transport mechanisms in bipolar membranes for (photo)electrochemical water splitting. *Sustain Energy Fuels* **2**, 2006–2015 (2018).

75. Sun, K. *et al.* A stabilized, intrinsically safe, 10% efficient, solar-driven water-splitting cell incorporating earth-abundant electrocatalysts with steady-state pH gradients and product separation enabled by a bipolar membrane. *Adv Energy Mater* **6**, 1600379 (2016).

76. Vargas-Barbosa, N. M. *et al.* Assessing the utility of bipolar membranes for use in photoelectrochemical water-splitting cells. *ChemSusChem* **7**, 3017–3020 (2014).

77. McDonald, M. B., Bruce, J. P., McEleney, K. & Freund, M. S. Reduced graphene oxide bipolar membranes for integrated solar water splitting in optimal pH. *ChemSusChem* **8**, 2645–2654 (2015).

78. Schulte, L., White, W., Renna, L. A. & Ardo, S. Turning water into a protonic diode and solar cell via doping and dye sensitization. *Joule* **5**, 2380–2394 (2021).

79. Alcaraz, A., Ramírez, P., Mafé, S., Holdik, H. & Bauer, B. Ion selectivity and water dissociation in polymer bipolar membranes studied by membrane potential and current-voltage measurements. *Polymer (Guildf)* **41**, 6627–6634 (2000).

80. Strathmann, H., Krol, J. J., Rapp, H. J. & Eigenberger, G. Limiting current density and water dissociation in bipolar membranes. *J Memb Sci* **125**, 123–142 (1997).

81. Hohenadel, A. *et al.* Electrochemical characterization of hydrocarbon bipolar membranes with varying junction morphology. *ACS Appl Energy Mater* **2**, 6817–6824 (2019).

82. Lin, M., Digdaya, I. A. & Xiang, C. Modeling the electrochemical behavior and interfacial junction profiles of bipolar membranes at solar flux relevant operating current densities. *Sustain Energy Fuels* **5**, 2149–2158 (2021).

83. Hohenadel, A., Gangrade, A. S. & Holdcroft, S. Spectroelectrochemical detection of water dissociation in bipolar membranes. *ACS Appl Mater Interfaces* **13**, 46125–46133 (2021).

84. Yan, Z. *et al.* The balance of electric field and interfacial catalysis in promoting water dissociation in bipolar membranes. *Energy Environ. Sci* **11**, 2235 (2018).

85. Konkena, B. & Vasudevan, S. Understanding aqueous dispersibility of graphene oxide and reduced graphene oxide through pKa measurements. *J. Phys. Chem. Lett* **3**, 872 (2012).

86. Orth, E. S. *et al.* pKa determination of graphene-like materials: validating chemical functionalization. *J Colloid Interface Sci* **467**, 239–244 (2016).

87. Publication Classification (54) Membrane for enhancing rates of water dissociation and water formation.

88. Wang, J. *et al.* Poly(aryl piperidinium) membranes and ionomers for hydroxide exchange membrane fuel cells. *Nat Energy* **4**, 392–398 (2019).

89. Chen, Y. *et al.* High-performance bipolar membrane development for improved water dissociation. *ACS Appl Polym Mater* (2020) doi:10.1021/acsapm.0c00653.

90. Luo, X., Rojas-Carbonell, S., Yan, Y. & Kusoglu, A. Structure-transport relationships of poly(aryl piperidinium) anion-exchange membranes: Eeffect of anions and hydration. *J Memb Sci* **598**, 117680 (2020).

91. Thuc, V. D., Cong Tinh, V. D. & Kim, D. Simultaneous improvement of proton conductivity and chemical stability of Nafion membranes via embedment of surface-modified ceria nanoparticles in membrane surface. *J Memb Sci* **642**, 119990 (2022).

92. Zhou, Y. *et al.* Rational use and reuse of Nafion 212 membrane in vanadium flow batteries. *RSC Adv* **7**, 19425–19433 (2017).

93. Blommaert, M. A., Vermaas, D. A., Izelaar, B., In'T Veen, B. & Smith, W. A. Electrochemical impedance spectroscopy as a performance indicator of water dissociation in bipolar membranes. *J Mater Chem A Mater* **7**, 19060–19069 (2019).

94. Craig, N. P. Electrochemical behavior of bipolar membranes. (2013).

95. Zenyuk, I. V, Das, P. K. & Weber, A. Z. Understanding impacts of catalyst-layer thickness on fuel-cell performance via mathematical modeling. *J Electrochem Soc* **163**, F691–F703 (2016).

96. Bui, J. C. *et al.* Continuum modeling of porous electrodes for electrochemical synthesis. *Chem Rev* **122**, 11022–11084 (2022).

97. Onsager, L. Deviations from ohm's law. *J. Chem. Phys.* **2**, 599–615 (1934).

98. Kaiser, V., Bramwell, S. T., Holdsworth, P. C. W. & Moessner, R. Onsager's wien effect on a lattice. *Nat. Mater.* **12**, 1033–1037 (2013).

99. Mafé, S., Manzanares, J. A. & Ramirez, P. Modeling of surface vs. bulk ionic conductivity in fixed charge membranes. *Physical Chemistry Chemical Physics* **5**, 376–383 (2003).

100. Schalenbach, M., Zeradjanin, A. R., Kasian, O., Cherevko, S. & Mayrhofer, K. J. J. A perspective on low-temperature water electrolysis - challenges in alkaline and acidic technology. *Int J Electrochem Sci* **13**, 1173–1226 (2018).

101. Sulistya Widodo, C., Sela, H. & Rahadi Santosa, D. The effect of NaCl concentration on the ionic NaCl solutions electrical impedance value using electrochemical impedance spectroscopy methods. *J Chem Phys* **2021**, (2018).

102. Konkena, B. & Vasudevan, S. Understanding aqueous dispersibility of graphene oxide and reduced graphene oxide through pKa measurements. *Journal of Physical Chemistry Letters* **3**, 867–872 (2012).

103. Torrisi, L., Cutroneo, M., Torrisi, A. & Silipigni, L. Measurements on five characterizing properties of graphene oxide and reduced graphene oxide foils. *Physica Status Solidi (A) Applications and Materials Science* **219**, 1–9 (2022).

104. Handbook of biological confocal microscopy (Springer US, 1995). doi:10.1007/978-1-4757-5348-6.

105. Welch, A. J. *et al.* Operando local pH measurement within gas diffusion electrodes performing electrochemical carbon dioxide reduction. *Journal of Physical Chemistry C* **125**, 20896–20904 (2021).

106. Boehme, A. *et al.* Direct observation of the local microenvironment in inhomogeneous CO_2 reduction gas diffusion electrodes via versatile pOH imaging. *Energy Environ Sci* (2023) doi:10.1039/d2ee02607d.

107. Sharifian, R., Wagterveld, R. M., Digdaya, I. A., Xiang, C. & Vermaas, D. A. Electrochemical carbon dioxide capture to close the carbon cycle. *Energy Environ Sci* (2021) doi:10.1039/d0ee03382k.

108. Electric power industry needs for grid-scale storage applications. (2010).

109. Fact Sheet | Energy Storage (2019) | White Papers | EESI. https://www.eesi.org/papers/view/energy-storage-2019.

110. Zhang, Z. *et al.* Cement clinker precursor production in an electrolyser. *Energy Environ Sci* **15**, 5129–5136 (2022).

111. Zhang, Z. *et al.* Porous metal electrodes enable efficient electrolysis of carbon capture solutions. *Energy Environ Sci* **15**, 705–713 (2022).

112. Zhang, Z. *et al.* pH matters when reducing CO_2 in an electrochemical flow cell. *ACS Energy Lett* **5**, 3101–3107 (2020).

113. Li, T., Lees, E. W., Zhang, Z. & Berlinguette, C. P. Conversion of bicarbonate to formate in an electrochemical flow reactor. *ACS Energy Lett* **5**, 2624–2630 (2020).

114. Zhang, Z. *et al.* Conversion of reactive carbon solutions into CO at low voltage and high carbon efficiency. *ACS Cent Sci* **8**, 749–755 (2022).

115. Culcasi, A., Gurreri, L., Micale, G. & Tamburini, A. Bipolar membrane reverse electrodialysis for the sustainable recovery of energy from pH gradients of industrial wastewater: Performance prediction by a validated process model. *J Environ Manage* **287**, (2021).

116. Xia, J., Eigenberger, G., Strathmann, H. & Nieken, U. Flow battery based on reverse electrodialysis with bipolar membranes: Single cell experiments. *J Memb Sci* **565**, 157–168 (2018).

117. Zaffora, A. *et al.* Energy harvesting by waste acid/base neutralization via bipolar membrane reverse electrodialysis. *Energies 2020, Vol. 13, Page 5510* **13**, 5510 (2020).

118. Kim, J. H. *et al.* Proof-of-concept experiments of an acid-base junction flow battery by reverse bipolar electrodialysis for an energy conversion system. *Electrochem commun* **C**, 157–161 (2016).

119. Zawodzinski, T. Redox flow batteries redox flow systems. *ACS Energy Letters* vol. 2 (2015).

120. Gurreri, L., Temburini, A. & Micale, G. Electromembrane processes experiments and modelling. (2021).

121. Lucas, É. *et al.* Asymmetric bipolar membrane for high current density electrodialysis operation with exceptional stability.

122. Vermaas, D. A., Sassenburg, M. & Smith, W. A. Photo-assisted water splitting with bipolar membrane induced pH gradients for practical solar fuel devices. *J Mater Chem A Mater* **3**, 19556–19562 (2015).

123. Yan, Q., Toghiani, H. & Wu, J. Investigation of water transport through membrane in a PEM fuel cell by water balance experiments. *J Power Sources* **158**, 316–325 (2006).

124. Keith, D. W., Holmes, G., St. Angelo, D. & Heidel, K. A process for capturing CO_2 from the atmosphere. *Joule* **2**, 1573–1594 (2018).

125. Van Straelen, J. & Geuzebroek, F. The thermodynamic minimum regeneration energy required for post-combustion CO_2 capture. *Energy Procedia* **4**, 1500–1507 (2011).

126. Gurkan, B. *et al.* Perspective and challenges in electrochemical approaches for reactive CO_2 separations. *iScience* **24**, 103422 (2021).

127. Seo, H. & Hatton, T. A. Electrochemical direct air capture of CO_2 using neutral red as reversible redox-active material. *Nat Commun* **14**, 1–11 (2023).

128. Li, X., Zhao, X., Liu, Y., Hatton, T. A. & Liu, Y. Redox-tunable Lewis bases for electrochemical carbon dioxide capture. *Nat Energy* **7**, 1065–1075 (2022).

129. Diederichsen, K. M., Liu, Y., Ozbek, N., Seo, H. & Hatton, T. A. Toward solvent-free continuous-flow electrochemically mediated carbon capture with high-concentration liquid quinone chemistry. *Joule* **6**, 221–239 (2022).

130. Clarke, L. E., Leonard, M. E., Hatton, T. A. & Brushett, F. R. Thermodynamic modeling of CO_2 separation systems with soluble, redox-active capture species. *Ind Eng Chem Res* **61**, 10531–10546 (2022).

131. Liu, Y., Ye, H. Z., Diederichsen, K. M., Van Voorhis, T. & Hatton, T. A. Electrochemically mediated carbon dioxide separation with quinone chemistry in salt-concentrated aqueous media. *Nat Commun* **11**, 1–11 (2020).

132. Rahimi, M., Khurram, A., Hatton, T. A. & Gallant, B. Electrochemical carbon capture processes for mitigation of CO_2 emissions. *Chem Soc Rev* **51**, 8676–8695 (2022).

133. Eisaman, M. D. *et al.* CO_2 separation using bipolar membrane electrodialysis. *Energy Environ Sci* **4**, 1319–1328 (2011).

134. Eisaman, M. D., Alvarado, L., Larner, D., Wang, P. & Littau, K. A. CO_2 desorption using high-pressure bipolar membrane electrodialysis. *Energy Environ Sci* **4**, 4031–4037 (2011).

135. Digdaya, I. A. *et al.* A direct coupled electrochemical system for capture and conversion of CO_2 from oceanwater. *Nat Commun* **11**, 1–10 (2020).

136. Sullivan, I. *et al.* Coupling electrochemical CO_2 conversion with CO_2 capture. *Nat Catal* **4**, 952–958 (2021).

137. Sharifian, R., Wagterveld, R. M., Digdaya, I. A., Xiang, C. & Vermaas, D. A. Electrochemical carbon dioxide capture to close the carbon cycle. *Energy Environ Sci* **14**, 781–814 (2021).

138. Liu, Y., Lucas, É., Sullivan, I., Li, X. & Xiang, C. Challenges and opportunities in continuous flow processes for electrochemically mediated carbon capture. *iScience* **25**, 105153 (2022).

139. Iizuka, A. *et al.* Carbon dioxide recovery from carbonate solutions using bipolar membrane electrodialysis. *Sep Purif Technol* **101**, 49–59 (2012).

140. Eisaman, M. D. *et al.* CO_2 separation using bipolar membrane electrodialysis. *Energy Environ Sci* **4**, 1319–1328 (2011).

141. Eisaman, M. D., Alvarado, L., Larner, D., Wang, P. & Littau, K. A. CO_2 desorption using high-pressure bipolar membrane electrodialysis. *Energy Environ Sci* **4**, 4031–4037 (2011).

142. Gurkan, B. *et al.* Perspective and challenges in electrochemical approaches for reactive CO_2 separations. *iScience* **24**, 103422 (2021).

143. Zabolotskii, V. I., Utin, S. V., Lebedev, K. A., Vasilenko, P. A. & Shel'Deshov, N. V. Study of pH correction process of chloride-bicarbonate dilute solutions by electrodialysis with bipolar membranes. *Russian Journal of Electrochemistry* **48**, 767–772 (2012).

144. Bui, J. C., Digdaya, I., Xiang, C., Bell, A. T. & Weber, A. Z. Understanding multi-ion transport mechanisms in bipolar membranes. *ACS Appl Mater Interfaces* acsami.0c12686 (2020) doi:10.1021/acsami.0c12686.

145. Bui, J. C., Digdaya, I., Xiang, C., Bell, A. T. & Weber, A. Z. Understanding multi-ion transport mechanisms in bipolar membranes. *ACS Appl Mater Interfaces* acsami.0c12686 (2020) doi:10.1021/acsami.0c12686.

146. Craig, N. P. Electrochemical behavior of bipolar membranes. (2013).

147. Lin, M., Digdaya, I. A. & Xiang, C. Modeling the electrochemical behavior and interfacial junction profiles of bipolar membranes at solar flux relevant operating current densities. *Sustain Energy Fuels* (2021) doi:10.1039/d1se00201e.

148. Dinh, H. Q., Toh, W. L., Chu, A. T. & Surendranath, Y. Neutralization short-circuiting with weak electrolytes erodes the efficiency of bipolar membranes. *ACS Appl Mater Interfaces* (2022) doi:10.1021/acsami.2c18685.

149. Lees, E. W. *et al.* Electrodes designed for converting bicarbonate into CO. *ACS Energy Lett* **5**, 2165–2173 (2020).

150. Li, T. *et al.* Electrolytic conversion of bicarbonate into CO in a flow cell. *Joule* **3**, 1487–1497 (2019).

151. Hodges, A. *et al.* A high-performance capillary-fed electrolysis cell promises more cost-competitive renewable hydrogen. *Nat Commun* **13**, 1304 (2022).

152. Nouri-Khorasani, A., Tabu Ojong, E., Smolinka, T. & Wilkinson, D. P. Model of oxygen bubbles and performance impact in the porous transport layer of PEM water electrolysis cells. *Int J Hydrogen Energy* **42**, 28665–28680 (2017).

153. Liu, J. *et al.* Elucidating the role of hydroxide electrolyte on anion-exchange-membrane water electrolyser performance. *J Electrochem Soc* **168**, 054522 (2021).

154. Lees, E. W., Mowbray, B. A. W., Parlane, F. G. & Berlinguette, C. P. Gas diffusion electrodes and membranes for CO_2 reduction electrolysers. *Nature Review Materials* 55–64 (2021) doi:10.1038/s41578-021-00356-2.

155. Wei, Z. D. *et al.* Water electrolysis on carbon electrodes enhanced by surfactant. *Electrochim Acta* **52**, 3323–3329 (2007).

156. Zeng, K. & Zhang, D. Recent progress in alkaline water electrolysis for hydrogen production and applications. *Prog Energy Combust Sci* **36**, 307–326 (2010).

157. Bird, R. B., Stewart, W. E. & Lightfoot, E. N. *Transport phenomena*. (Wiley, 2002).

158. Sforza, P. *Drag Estimation*. *Commercial Airplane Design Principles* (2014). doi:10.1016/b978-0-12-419953-8.00009-7.

159. Wang, X.-K., Zhao, G.-X., Huang, X. & Wang, X. Progress in the catalyst exploration for heterogeneous CO_2 reduction and utilization: a critical review. *J. Mater. Chem. A* **5**, 21625–21649 (2017).

160. Liu, Y. & Guo, L. On factors limiting the performance of photoelectrochemical CO2 reduction. *Journal of Chemical Physics* **152**, (2020).

161. Diederichsen, K. M. *et al.* Electrochemical methods for carbon dioxide separations. *Nature Reviews Methods Primers 2022 2:1* **2**, 1–20 (2022).

162. White, J. L. *et al.* Light-driven heterogeneous reduction of carbon dioxide: photocatalysts and photoelectrodes. *Chem Rev* **115**, 12888–12935 (2015).

163. Xu, J. *et al.* Review on electrochemical carbon dioxide capture and transformation with bipolar membranes. *Chinese Chemical Letters* 108075 (2022) doi:10.1016/J.CCLET.2022.108075.

164. Chang, H. M. & Zenyuk, I. V. Membrane electrode assembly design to prevent CO_2 crossover in CO_2 reduction reaction electrolysis. *Communications Chemistry 2023 6:1* **6**, 1–3 (2023).

165. Kim, B., Hillman, F., Ariyoshi, M., Fujikawa, S. & Kenis, P. J. A. Effects of composition of the micro porous layer and the substrate on performance in the electrochemical reduction of CO_2 to CO. *J Power Sources* **312**, 192–198 (2016).

166. Sreekanth, N. & Phani, K. L. Selective reduction of CO_2 to formate through bicarbonate reduction on metal electrodes: new insights gained from SG/TC mode of SECM. *Chemical Communications* **50**, 11143–11146 (2014).

167. Lu, Q. *et al.* A selective and efficient electrocatalyst for carbon dioxide reduction. *Nat Commun* **5**, 1–6 (2014).

168. Welch, A. J. *et al.* Nanoporous gold as a highly selective and active carbon dioxide reduction catalyst. (2018) doi:10.1021/acsaem.8b01570.

169. Jang, Y. J. *et al.* Selective CO production by Au coupled ZnTe/ZnO in the photoelectrochemical CO_2 reduction system. *Energy Environ Sci* **8**, 3597–3604 (2015).

170. Ozden, A. *et al.* Carbon-efficient carbon dioxide electrolysers. *Nature Sustainability 2022 5:7* **5**, 563–573 (2022).

171. Hoang, T. T. H. *et al.* Nano porous copper-silver alloys by additive-controlled electro-deposition for the selective electroreduction of CO_2 to ethylene and ethanol. *J Am Chem Soc* jacs.8b01868 (2018) doi:10.1021/jacs.8b01868.

172. Hoang, T. T. H., Ma, S., Gold, J. I., Kenis, P. J. A. & Gewirth, A. A. Nanoporous copper films by additive-controlled electrodeposition: CO_2 reduction catalysis. *ACS Catal* **7**, 3313–3321 (2017).

173. Li, C. W., Ciston, J. & Kanan, M. W. Electroreduction of carbon monoxide to liquid fuel on oxide-derived nanocrystalline copper. *Nature* **508**, 504–507 (2014).

174. Dinh, C. *et al.* CO_2 electroreduction to ethylene via hydroxide-mediated copper catalysis at an abrupt interface. **787**, 783–787 (2018).

175. Lee, S. Y. *et al.* Mixed copper states in anodized Cu electrocatalyst for stable and selective ethylene production from CO_2 reduction mixed copper states in anodized Cu electrocatalyst for stable and selective ethylene production from CO_2 reduction. (2018) doi:10.1021/jacs.8b02173.

176. Environ, E. Environmental Science New insights into the electrochemical reduction of carbon dioxide on metallic copper surfaces. 7050–7059 (2012) doi:10.1039/c2ee21234j.

177. Pham, Q. N., Shao, B., Kim, Y. & Won, Y. Hierarchical and well-ordered porous copper for liquid transport properties control. *ACS Appl Mater Interfaces* **10**, 16015–16023 (2018).

178. Lührs, L. & Weissmüller, J. Scripta. Nanoporous copper-nickel – macroscopic bodies of a strong and deformable nanoporous base metal by dealloying. *Scr Mater* **155**, 119–123 (2018).

179. Egle, T. *et al.* Multiscale morphology of nanoporous copper made from intermetallic phases. *ACS Appl Mater Interfaces* **9**, 25615–25622 (2017).

180. Zugic, B. *et al.* Dynamic restructuring drives catalytic activity on nanoporous gold-silver alloy catalysts. *Nat Mater* **16**, 558–564 (2017).

181. Diao, F. *et al.* Two-step fabrication of nanoporous copper films with tunable morphology for SERS application. *Appl Surf Sci* **427**, 1271–1279 (2018).

182. Qi, Z. *et al.* Formation and characterization of monolithic nanoporous copper by chemical dealloying of Al− Cu alloys. *The Journal of Physical Chemistry C* **113**, 6694–6698 (2009).

183. Cave, E. R. *et al.* Improved CO_2 reduction activity towards C^{2+} alcohols on a tandem Au on Cu electrocatalyst. *Nat Catal* **1**, (2018).

184. Weng, L. C., Bell, A. T. & Weber, A. Z. Modeling gas-diffusion electrodes for CO_2 reduction. *Physical Chemistry Chemical Physics* **20**, 16973–16984 (2018).

185. Marepally, B. C. *et al.* Enhanced formation of >C1 products in electroreduction of CO_2 by adding a CO_2 adsorption component to a gas-diffusion layer-type catalytic electrode. *ChemSusChem* **10**, 4442–4446 (2017).

186. Verma, S., Lu, X., Ma, S., Masel, R. I. & Kenis, P. J. A. The effect of electrolyte composition on the electroreduction of CO_2 to CO on Ag based gas diffusion electrodes. *Phys. Chem. Chem. Phys.* **18**, 7075–7084 (2016).